The Development of an Ice-Ocean Coupled Model for the Northern Hemisphere

ABE CHENG

Sverdrup Technologies Incorporated
Stennis Space Center, MS

RUTH H. PRELLER

Ocean Dynamics and Prediction Branch
Oceanography Division

December 30, 1996

REPORT DOCUMENTATION PAGE

Public reporting burden for this collection of information is estimated to average 1 hour per response, including the time for reviewing instructions, searching existing data sources, gathering and maintaining the data needed, and completing and reviewing the collection of information. Send comments regarding this burden or any other aspect of this collection of information, including suggestions for reducing this burden, to Washington Headquarters Services, Directorate for information Operations and Reports, 1215 Jefferson Davis Highway, Suite 1204, Arlington, VA 22202-4302, and to the Office of Management and Budget, Paperwork Reduction Project (0704-0188), Washington, DC 20503.

1. AGENCY USE ONLY (Leave blank)	2. REPORT DATE December 30, 1996	3. REPORT TYPE AND DATES COVERED Final

4. TITLE AND SUBTITLE

The Development of an Ice-Ocean Coupled Model for the Northern Hemisphere

6. AUTHOR(S)

Abe Cheng* and Ruth H. Preller

5. FUNDING NUMBERS

Job Order No.	573509305
Program Element No.	0603207N
Project No.	X0513
Task No.	100
Accession No.	DN894428

7. PERFORMING ORGANIZATION NAME(S) AND ADDRESS(ES)

Naval Research Laboratory
Oceanography Division
Stennis Space Center, MS 39529-5004

8. PERFORMING ORGANIZATION REPORT NUMBER

NRL/FR/7322--95-9627

9. SPONSORING/MONITORING AGENCY NAME(S) AND ADDRESS(ES)

Space and Naval Warfare Systems Command
PWM-165-D
Washington, DC 22202

10. SPONSORING/MONITORING AGENCY REPORT NUMBER

11. SUPPLEMENTARY NOTES

*Sverdrup Technologies Incorporated, Stennis Space Center, MS 39529-5004

12a. DISTRIBUTION/AVAILABILITY STATEMENT

Approved for public release; distribution unlimited.

12b. DISTRIBUTION CODE

13. ABSTRACT (Maximum 200 words)

The Polar Ice Prediction System (PIPS), based on the Hibler ice model, has been reformulated into spherical coordinates for the Northern Hemisphere. These spherical coordinates help to avoid a numerical singularity at the North Pole and numerical instabilities in high latitudes. Further, a coordinate transformation was chosen so that a new equator coincides with the 170° W–10° E great circle, and a new north pole is located at the intersection of the 100° E meridian and the true Equator. The spherical coordinate version of PIPS has been tested against the Cartesian coordinate version. It is found that all the physics in the two versions remain the same. There are no differences in the estimated ice conditions between these two versions.

The spherical coordinate PIPS model has been extended southward in a version of the model called PIPS2.0. In another development, the Cox ocean model has been transformed into the same spherical coordinate system as PIPS and then coupled with the sea ice model. The coupling technique of the ice and ocean models is conceptually similar to that described in Hibler and Bryan, but the heat and momentum exchanges have been modified. The two models are coupled by exchanging daily information of ice and ocean. The coupled model has been tested using the 1986 monthly forcing of the Navy Operational Global Atmospheric Prediction System (NOGAPS), as well as other inputs describing river runoff, bottom topography, and climatological water temperature and salinity. Preliminary results have been published.

This report describes the coordinate transformation referred to above, the physics of the heat and momentum exchanges, model parameters, variable ice-water drag coefficients, and a test case using the 1986 monthly NOGAPS forcing fields. For the discussions in this report, the model domain was divided into seven subregions: the Sea of Okhotsk, the Bering Sea, the central Arctic, the Barents Sea, Hudson Bay, the Labrador Sea/Baffin Bay, and the Norwegian/East Greenland Seas.

14. SUBJECT TERMS

sea ice forecasting, sea ice model, sea ice analysis

15. NUMBER OF PAGES 67

16. PRICE CODE

17. SECURITY CLASSIFICATION OF REPORT	18. SECURITY CLASSIFICATION OF THIS PAGE	19. SECURITY CLASSIFICATION OF ABSTRACT	20. LIMITATION OF ABSTRACT
Unclassified	Unclassified	Unclassified	Same as report

NSN 7540-01-280-5500

CONTENTS

THE DEVELOPMENT OF AN ICE-OCEAN COUPLED MODEL
FOR THE NORTHERN HEMISPHERE

1.0 INTRODUCTION

The Polar Ice Prediction System (PIPS), based on the Hibler ice model [Hibler 1979; 1980], is an operational numerical model used by the Fleet Numerical Meteorology and Oceanography Center (FNMOC) for daily prediction of ice-drift velocity, thickness, and concentration in the Arctic Ocean. PIPS uses daily information on ocean currents, oceanic heat flux, incoming solar radiation, sensible heat flux, total heat flux, surface air temperatures, geostrophic wind stresses, and new data on ice concentrations to make these estimates. The oceanic variables that it needs, ocean currents and heat fluxes, are monthly mean values derived from the Cox ocean model [Hibler and Bryan 1987].

The PIPS domain mainly covers the central Arctic, the Barents Sea, the East Greenland Sea, and the Norwegian Sea (Fig. 1.1). The PIPS grid, a subsection of the FNMOC polar stereographic projection grid for the Northern Hemisphere, has a dimension of 47 × 25 grid squares, each approximately 127 km on a side. Since the difference between the spherical grid and the stereographic projected grid is minimal in the Arctic, less than 0.8% throughout the model domain, the PIPS model Cartesian grid can be used to estimate sea ice conditions without losing much accuracy.

South of the Arctic, however, in areas such as the Labrador Sea and the Sea of Okhotsk, the differences between the spherical grid and stereographic projected grids are significant enough that the PIPS model cannot be simply extended to accurately compute seasonal conditions there. The PIPS model must be transformed into spherical coordinates, and the most appropriate transformation is discussed in this report.

Owens et al. [1990] transformed the Hibler ice model to the spherical coordinates of the Earth latitudes and longitudes for Antarctic sea ice. Since the land area of the Antarctic continent covers most areas from 80° S to the South Pole, the Owens et al. ice model had no numerical singularity at the Pole, and very little numerical instability in high latitudes. Thus, there was no need to solve the flow equations in the actual polar areas in the Owens et al. model.

However, this set of spherical coordinates would not work for the Northern Hemisphere because of the circulation calculations required for the North Pole. Flato and Hibler [1993] and Holland [1994] have tried to use the standard Earth latitudes and longitudes in models of the Arctic. They introduced an "island" at the North Pole to avoid making calculations there, but the results show sea ice obviously drifting around the island rather than through it. Holland then transformed the North Pole to Siberia for calculations, and sea ice drift across the Pole occurred. Since they used the same atmospheric forcing for both sets of calculations, the difference must have been caused by the coordinate systems that were used.

In addition to the problem of sea ice not drifting across the Pole, sea ice was thinner in the island models than in the transformed pole model calculations. The sea ice was up to 0.5 m thicker
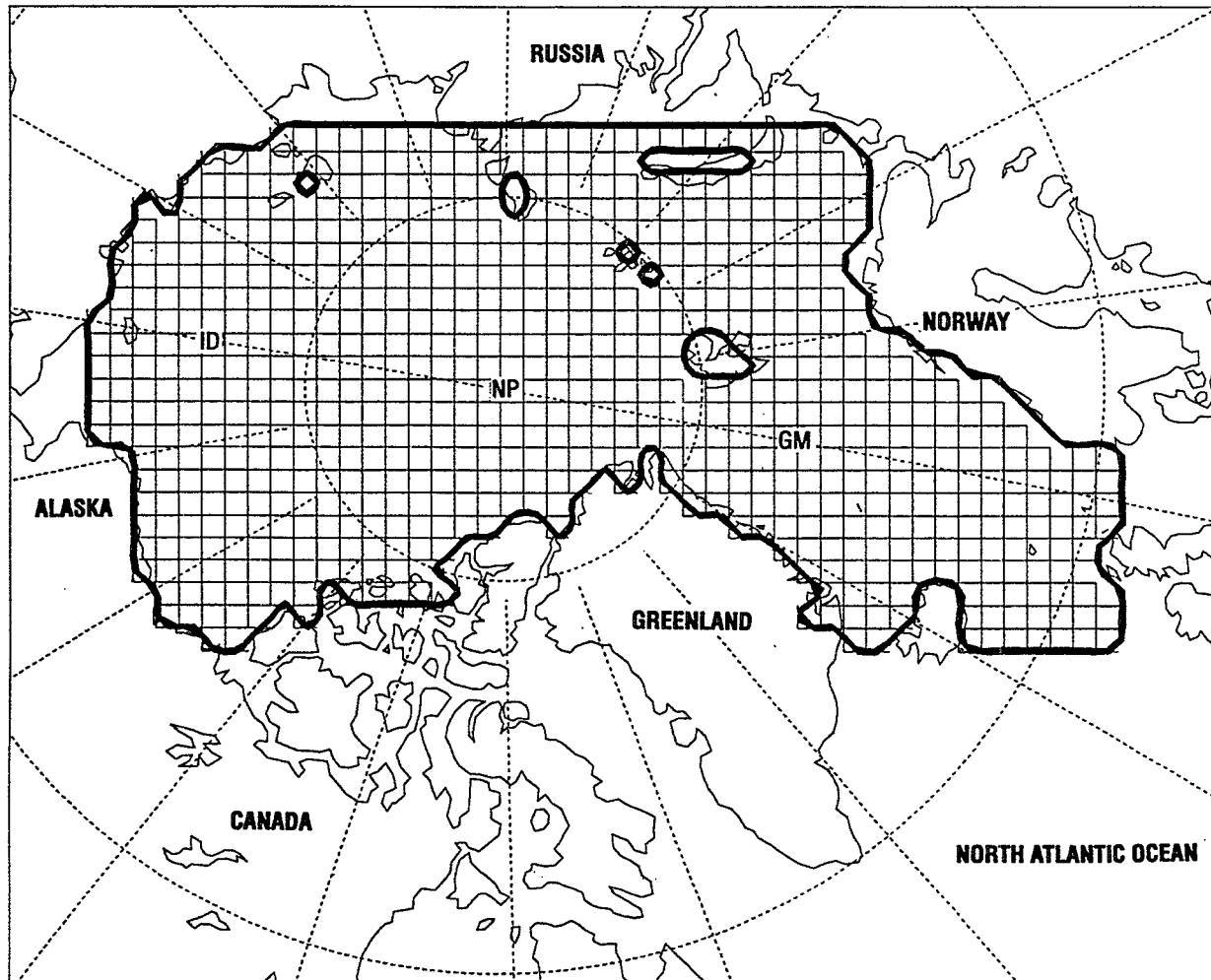
Fig. 1.1 — PIPS domain overlaid with 127-km resolution grid

in the transformed pole model calculations than in the island model calculations. The distribution of ice thickness was similar in the transformed Pole model calculations to other work [Cheng and Preller 1992; 1994]: ice was thick north of Greenland and the Canadian Archipelago, less thick across the North Pole, and thin near the Russian coast. Consequently, for the PIPS model to describe the evolution of conditions throughout the Northern Hemisphere it, too, needs the transformed pole of the spherical coordinate system rotated away from the geographic North Pole.

This report describes the transformation of the PIPS model from rectangular coordinates to the new spherical coordinates, and the PIPS model modifications required to accommodate that transformation. The transformed model grid matches the original PIPS grid closely where they overlap, and it can estimate the evolution of ice conditions south of the original PIPS grid without the numerical difficulties. In the following discussions, we first show the transformation that was made, and then test cases that compared the results of the new model against the rectangular PIPS. It is noted how the transformed model maintains the same physics as the rectangular PIPS, and the programming changes necessary to maintain the physics are described. Test results are divided into the model domain's seven subregions: the Sea of Okhotsk, the Bering Sea, the central Arctic, the Barents Sea, Hudson Bay, the Labrador Sea/Baffin Bay, and the Norwegian/East Greenland Seas.

The transformed PIPS model was extended southward (to 20° N–30° N, depending on location) to cover most sea ice formation and drift in the Northern Hemisphere with fine grid resolution. The coupling of the ice model to the Cox ocean circulation model for calculation purposes is described, as well as how the atmospheric forcing fields, bathymetry data, ocean temperature, and salinity fields were interpolated to support studies with the transformed and extended PIPS model at lower latitudes. The autonomy of the PIPS model and the ocean circulation model (the Cox model [1984] for this work) was maintained during this development as much as possible so that the Cox ocean model could be replaced in future developments by upgraded code (be it an upgraded Cox model, or the Mellor ocean model [1992]).

At present, there are three operational PIPS model versions: a coarse spatial grid version (127 km), which covers the entire Arctic area of interest, and two finer grid resolution versions (20-km grid squares): one for the Barents Sea (the Regional Polar Ice Prediction System–Barents Sea [RPIPS-B]) and one for the East Greenland Sea (the Regional Polar Ice Prediction System–Greenland Sea [EPIPS-G]). The finer grid models are not coupled with ocean models; they are driven by constant ocean currents and oceanic heat fluxes, and will be replaced in the future by a finer grid ice-ocean coupled model.

The ice-ocean coupled model has been applied to studies other than operational uses, such as modeling the changes in the Arctic Ocean due to variable river outflows [Allard et al. 1995]. In addition, the "ocean-only" part of the model has been used to study the dispersion of radioactive waste material in the Kara and Barents Seas in the Arctic and in the North Atlantic [Preller et al. 1993; Preller and Cheng 1995]. It is anticipated that further applications of the model will evolve with time.

2.0 NEW SPHERICAL COORDINATES

Figures 2.1 and 2.2 show a coordinate transformation from the Earth latitudes and longitudes to a new spherical coordinate system that removes computational instabilities from the PIPS model. This particular coordinate transformation has the following advantages. There is neither numerical instability in high latitudes nor numerical singularity at the North Pole of this coordinate system because the new north pole has been transformed to near the equator. In addition, putting the new north pole in a land mass means computations near or across a pole will never be an issue. For the PIPS domain, the spherical grid to which the computational algorithms were transformed and the Cartesian grid of the original formulation are almost identical. Therefore, when the extra terms are added to account for the coordinate transformation, the physics remain the same, and one grid can be verified against the other. The same spherical geometry was introduced into the Cox ocean model [1984], then both the PIPS ice model and the Cox ocean model were coupled in spherical coordinates.

The new set of spherical coordinates for the PIPS model was constructed in the following manner. First, longitudes were rotated so that the prime meridian was located at 190° E (Fig. 2.1). Then, the North Pole was rotated 90° down the 100° E meridian until it resided on the true equator (Fig. 2.2). Therefore, the transformed coordinates coincide with the 170° W–10° E great circle, which passes through the North Pole as the new equator. The new equator passes right through the old PIPS grid, where each grid square in the new spherical coordinates is about 1.143° on a side. The Cartesian PIPS grid and the spherical coordinates PIPS grid are almost identical. The X- and Y-axes are stereographic projections of the 170° W–10° E and the 80° W–100° E great circles, respectively.
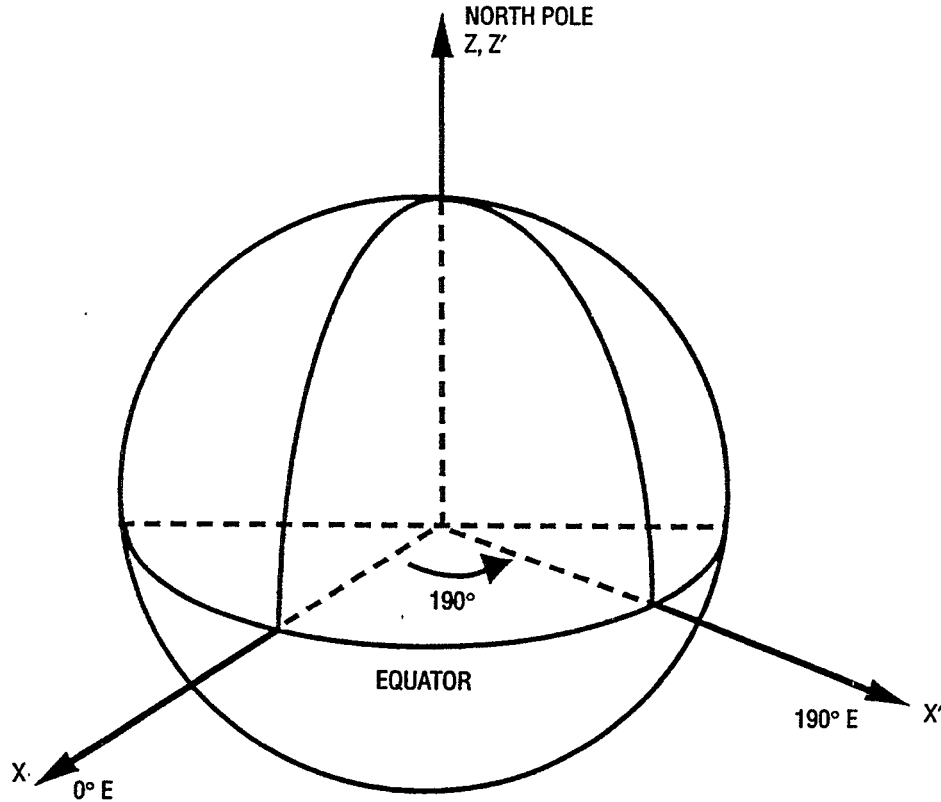
Fig. 2.1 — Coordinate transformation from the Earth-oriented longitudes and latitudes,
step one: rotate Greenwich meridian 190° eastward

To convert the model from Cartesian coordinates to the new spherical coordinates, replace δx and δy by $\delta\phi$ and $\delta\theta$ as follows:

$$\delta x = r \ \cos\theta\delta\phi \ ,$$

$$\delta y = r \ \delta\theta \ ,$$

where δx and δy represent spatial intervals in Cartesian coordinates, r is the Earth's radius, θ is the latitude in the spherical coordinates, ϕ is the longitude, and $\delta\phi$ and $\delta\theta$ are increments in the spherical coordinates. The physics of the ice and ocean models were recast into these variables.

The edges of the PIPS grid are about 11 grid squares from the new equator of the transformed coordinates, or about 12.57°. The difference between the Cartesian grid (a projected grid) and the spherical grid is less than 0.8% at the boundaries (i.e., the difference between the 12.57° arc distance and the sin 12.57°). Section 5.0 of this report provides a more thorough comparison between the Cartesian model and the model with the transformed spherical coordinates. The results of ice-drift velocity, concentration, and thickness cannot be distinguished in vector or contour plots.

3.0 ICE MOMENTUM BALANCE EQUATION

As in Hibler [1979], Preller and Posey [1985], Hibler and Bryan [1987], and Cheng and Preller [1992; 1994], the momentum balance equation for sea ice is as follows:
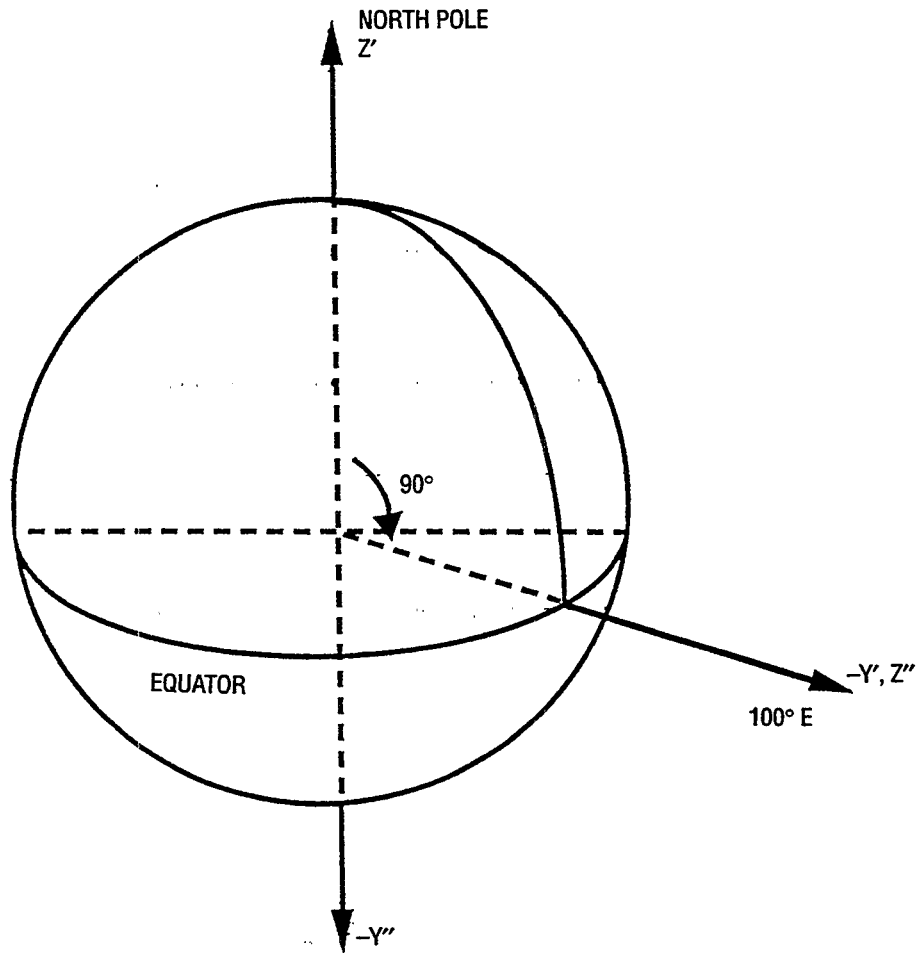
Fig. 2.2 — Coordinate transformation from the Earth-oriented longitudes and latitudes, step two: rotate North Pole 90° southward along the 100° E meridian

$$m\frac{\partial \mathbf{u}}{\partial t} + m\mathbf{u} \cdot \nabla \mathbf{u} + mf\mathbf{k} \times \mathbf{u} = \tau_a + \tau_w - mg\nabla H + \mathbf{F},$$ (1)

where m represents ice mass per unit area,

   $\mathbf{u}$ is ice-drift velocity expressed in spherical coordinates as $(\hat{\phi}u_\phi, \hat{\theta}u_\theta)$,

   $\hat{\phi}$ and $\hat{\theta}$ are the unit vectors in the angular coordinates of the spherical coordinate system into which the equation of motion must be transformed,

   f is the Coriolis parameter,

   $\mathbf{k}$ is the unit vector that points radially,

   τ_a is the wind stress at the ice surface,

   τ_w is the ocean current drag stress on the bottom of the sea ice,

   g is the gravitational acceleration,

H is the dynamic height of ocean currents, and

F is a force produced by ice internal stress.

This equation must be transformed into spherical coordinates to ensure that the physics of the ice-ocean model is correct.

As long as **u** is expressed in spherical coordinates, the temporal derivative $m \dfrac{\partial \mathbf{u}}{\partial t}$ term needs no modification for inclusion in the PIPS model.

The gradient term ∇ is modified in the following way. Since the sea ice drifts horizontally at the sea surface, the vertical derivative is zero in the gradient term. The other components are written as $\left(\hat{\phi} \dfrac{1}{r\cos\theta} \dfrac{\partial}{\partial \phi}, \hat{\theta} \dfrac{1}{r} \dfrac{\partial}{\partial \theta} \right)$. The total advection term is equivalent to $m\nabla\left(\dfrac{1}{2}|\mathbf{u}|^2 \right) - \mathbf{u} \times (\nabla \times \mathbf{u})$ in spherical coordinates where the $\times$ is the cross-product. Expanding this term gives, for the advection

term, $m\left(u_\phi \dfrac{1}{r\cos\theta}\dfrac{\partial \mathbf{u}}{\partial \phi} + u_\theta \dfrac{1}{r}\dfrac{\partial \mathbf{u}}{\partial \theta} - \hat{\phi}\dfrac{u_\theta u_\phi \tan\theta}{r} + \hat{\theta}\dfrac{u_\phi u_\phi \tan\theta}{r} \right)$. The Coriolis term $mf\,\mathbf{k}\times\mathbf{u}$ is written

as $mf\,(\mathbf{k}\times\hat{\theta}u_\phi + \mathbf{k}\times\hat{\phi}u_\theta)$. Note that the Coriolis parameter should be evaluated for each grid cell because of the variations in its value with latitude.

The terms for wind and ocean current stresses are expressed as follows:

$$\tau_a = \rho_{air} C_a \left| \mathbf{U}_g \right| \left\{ \mathbf{U}_g \cos\alpha_a + \mathbf{k}\times\mathbf{U}_g \sin\alpha_a \right\} \text{ and}$$

$$\tau_w = \rho_w C_w \left| \mathbf{U}_w - \mathbf{u} \right| \left\{ \left(\mathbf{U}_w - \mathbf{u} \right)\cos\alpha_w + \mathbf{k}\times\left(\mathbf{U}_w - \mathbf{u} \right)\sin\alpha_w \right\},$$

where $\mathbf{U}_g$ represents the geostrophic winds,

$\mathbf{U}_w$ is the ocean current of the mixed layer,

ρ_{air} and ρ_w are the densities of air and seawater,

C_a and C_w are drag coefficients of wind and ocean currents, and

α_a and α_w are the turning angles between air and ice and between ice and water, respectively.

The law of the wall was applied to compute the variable coefficient C_w as a function of sea ice thickness. Further discussions and comparisons are presented in Secs. 12.0 and 14.0. In those discussions, the symbol $C_{d,ice\text{-}water}$ is used for the drag between sea ice and water.

The force **F** due to the ice internal stress σ_{ij} can be written as follows:

$$F_j = \dfrac{1}{r\cos\theta}\dfrac{\partial}{\partial\theta}(\cos\theta\;\sigma_{\theta j}) + \dfrac{1}{r\cos\theta}\dfrac{\partial\sigma_{\phi j}}{\partial\phi}, \text{ or}$$

$$\mathbf{F} = \nabla \bullet \sigma_{ij} = (\frac{-\tan\theta}{r}\sigma_{\theta\phi} + \frac{1}{r}\frac{\partial\sigma_{\theta\phi}}{\partial\theta} + \frac{1}{r\cos\theta}\frac{\partial\sigma_{\phi\phi}}{\partial\phi})\hat{\phi} + (\frac{-\tan\theta}{r}\sigma_{\theta\theta} + \frac{1}{r}\frac{\partial\sigma_{\theta\theta}}{\partial\theta} + \frac{1}{r\cos\theta}\frac{\partial\sigma_{\phi\theta}}{\partial\phi})\hat{\theta}, \quad (2)$$

where i and j represent the indices of the variables θ and ϕ. Note that the divergence operator introduces the extra terms $\frac{-\tan\theta}{r}\sigma_{\theta\theta}$ and $\frac{-\tan\theta}{r}\sigma_{\theta\phi}$ when it operates due to the coordinate transformation. The ice internal stress ϕ_{ij} and the corresponding strain ε_{ij} (or a strain rate to be precise) are shown below:

$$\sigma_{ij} = 2\eta\varepsilon_{ij} + \delta_{ij}((\zeta - \eta)\ \varepsilon_{kk} - P/2),$$

where $\zeta = P/2\Delta$ and $\eta = \zeta/e^2$ (computed from u_ϕ and u_θ in the previous time step),

$$\Delta = \left\{\varepsilon_{kk}^2\left(1 + \frac{1}{e^2}\right) + \frac{4\varepsilon_{\phi\theta}^2}{e^2} + 2\varepsilon_{\phi\phi}\varepsilon_{\theta\theta}\left(1 - \frac{1}{e^2}\right)\right\}^{1/2},$$

$$P = 2.75 \bullet 10^4 he^{-20(1-A)},$$

A and h are ice concentration and thickness, respectively,

δ_{ij} is the Kronecker delta function: 1 as $i = j$ and 0 otherwise,

$e = 2,$

$$\varepsilon_{kk}^2 = \varepsilon_{\phi\phi}^2 + \varepsilon_{\theta\theta}^2,$$

$$\varepsilon_{\phi\phi} = \frac{1}{r\cos\theta}\frac{\partial u_\phi}{\partial\phi} + \frac{u_\theta\tan\theta}{r},$$

$$\varepsilon_{\phi\theta} = \varepsilon_{\theta\phi} = \frac{1}{2}\left(\frac{1}{r\cos\theta}\frac{\partial u_\theta}{\partial\phi} + \frac{u_\phi\tan\theta}{r} + \frac{1}{r}\frac{\partial u_\phi}{\partial\theta}\right), \text{ and}$$

$$\varepsilon_{\theta\theta}^2 = \frac{1}{r}\frac{\partial u_\theta}{\partial\theta}.$$

Therefore, the force $\frac{\partial\sigma_{i\phi}}{\partial x_i}$ due to the ice internal stress can be expressed as follows (δx_i and δx_j represent either $r\cos\theta\delta\phi$ or $r\delta\theta$):

$$\frac{\partial\sigma_{i\phi}}{\partial x_i} = \frac{\partial}{\partial x_i}(2\eta\varepsilon_{i\phi} + \delta_{i\phi}((\zeta-\eta)\varepsilon_{kk} - P/2))$$

$$= \frac{\partial}{r\cos\theta\,\partial\phi}\left(2\eta\left(\frac{1}{r\cos\theta}\frac{\partial u_\phi}{\partial\phi}+\frac{u_\theta\tan\theta}{r}\right)\right)$$

$$+\frac{\partial}{r\partial\theta}\left(2\eta\frac{1}{2}\left(\frac{1}{r\cos\theta}\frac{\partial u_\theta}{\partial\phi}+\frac{u_\phi\tan\theta}{r}+\frac{1}{r}\frac{\partial u_\phi}{\partial\theta}\right)\right)$$

$$+\frac{\partial}{r\cos\theta\,\partial\phi}\left((\zeta-\eta)\left(\frac{1}{r\cos\theta}\frac{\partial u_\phi}{\partial\phi}+\frac{u_\theta\tan\theta}{r}+\frac{1}{r}\frac{\partial u_\theta}{\partial\theta}\right)-P/2\right)$$

$$=\frac{\partial}{r\cos\theta\,\partial\phi}\left((\zeta+\eta)\frac{1}{r\cos\theta}\frac{\partial u_\phi}{\partial\phi}\right)+\frac{\partial}{r\partial\theta}\left(\eta\frac{1}{r\cos\theta}\frac{\partial u_\theta}{\partial\phi}\right)$$

$$+\frac{\partial}{r\partial\theta}\left(\eta\frac{1}{r}\frac{\partial u_\phi}{\partial\theta}\right)+\frac{\partial}{r\cos\theta\,\partial\phi}\left((\zeta-\eta)\frac{1}{r}\frac{\partial u_\theta}{\partial\theta}\right)$$

$$-\frac{\partial}{r\cos\theta\,\partial\phi}(P/2)+\frac{\tan\theta}{r}\frac{\partial}{r\cos\theta\,\partial\phi}(2\eta u_\theta)$$

$$+\frac{\tan\theta}{r}\frac{\partial(\eta u_\phi)}{r\partial\theta}+\frac{\sec^2\theta}{r}\frac{\eta u_\phi}{r}+\frac{\tan\theta}{r}\frac{\partial}{r\cos\theta\,\partial\phi}((\zeta-\eta)u_\theta).$$

Following Hibler [1979], apply the finite difference method to a discretized form of $\dfrac{\partial\sigma_{i\phi}}{\partial x_i}$ and the equation above becomes:

$$\frac{\partial\sigma_{i\phi}}{\partial x_i}\approx\frac{1}{2}\left(\frac{1}{r\cos\theta\Delta\phi}\right)^2\left\{\begin{array}{l}u_{\phi m-1n}(\eta_{mn+1}+\eta_{mn}+\zeta_{mn+1}+\zeta_{mn})\\-u_{\phi mn}(\eta_{mn+1}+\eta_{mn}+\eta_{m+1n+1}+\eta_{m+1n}\\+\zeta_{mn+1}+\zeta_{mn}+\zeta_{m+1n+1}+\zeta_{m+1n})\\+u_{\phi m+1n}(\eta_{m+1n+1}+\eta_{m+1n}+\zeta_{m+1n+1}+\zeta_{m+1n})\end{array}\right\}$$

$$+\frac{1}{4}\frac{1}{r^2\cos\theta\Delta\phi\Delta\theta}\left\{\begin{array}{l}\eta_{m+1n+1}(u_{\theta m+1n+1}+u_{\theta m+1n}-u_{\theta mn+1}-u_{\theta mn})\\+\eta_{mn+1}(u_{\theta mn+1}+u_{\theta mn}-u_{\theta m-1n+1}-u_{\theta m-1n})\\+\eta_{m+1n}(u_{\theta mn}+u_{\theta mn-1}-u_{\theta m+1n}-u_{\theta m+1n-1})\\+\eta_{mn}(u_{\theta m-1n}+u_{\theta m-n-1}-u_{\theta mn}-u_{\theta mn-1})\end{array}\right\}$$

$$+\frac{1}{2}\left(\frac{1}{r\Delta\theta}\right)^2\left\{\begin{array}{l}u_{\phi mn-1}(\eta_{mn}+\eta_{m+1n})\\-u_{\phi mn}(\eta_{mn}+\eta_{m+1n}+\eta_{mn+1}+\eta_{m+1n+1})\\+u_{\phi mn+1}(\eta_{mn+1}+\eta_{m+1n+1})\end{array}\right\}$$

$$+\frac{1}{4}\frac{1}{r^2\cos\theta\Delta\phi\Delta\theta}\left\{\begin{array}{l}(\zeta_{m+1\,n+1}-\eta_{m+1\,n+1})(u_{\theta m+1\,n+1}+u_{\theta mn+1}-u_{\theta m+1\,n}-u_{\theta mn})\\[4pt]+(\zeta_{m+1\,n}-\eta_{m+1\,n})(u_{\theta m+1\,n}+u_{\theta m\,n}-u_{\theta m+1\,n-1}-u_{\theta mn-1})\\[4pt]+(\zeta_{m\,n+1}-\eta_{m\,n+1})(u_{\theta mn}+u_{\theta m-1\,n}-u_{\theta m\,n+1}-u_{\theta m-1\,n+1})\\[4pt]+(\zeta_{mn}-\eta_{mn})(u_{\theta mn-1}+u_{\theta m-1\,n-1}-u_{\theta mn}-u_{\theta m-1\,n})\end{array}\right\}$$

$$-\frac{1}{r\cos\theta\Delta\phi}(P/2)+\frac{\tan\theta}{r}\frac{1}{r\cos\theta\Delta\phi}\frac{1}{2}\left\{u_{\theta m+1\,n}(\eta_{m\,n+1}+\eta_{m\,n})-u_{\theta m-1n}(\eta_{mn}+\eta_{mn-1})\right\}$$

$$+\frac{\tan\theta}{r}\frac{1}{r\Delta\theta}\frac{1}{4}\left\{u_{\phi mn+1}(\eta_{m+1\,n}+\eta_{m\,n})-u_{\phi mn-1}(\eta_{mn}+\eta_{m-1\,n})\right\}$$

$$+\frac{\sec^2\theta}{r}\frac{1}{4r}u_{\phi mn}(\eta_{mn}+\eta_{mn+1}+\eta_{m+1\,n}+\eta_{m+1\,n+1})$$

$$+\frac{\tan\theta}{r}\frac{1}{r\cos\theta\Delta\phi}\frac{1}{4}\left\{\begin{array}{l}u_{\theta m+1\,n}(\zeta_{mn+1}+\zeta_{mn}-\eta_{mn+1}-\eta_{mn})\\[4pt]-u_{\theta m-1\,n}(\zeta_{mn}+\zeta_{m\,n-1}-\eta_{mn}-\eta_{mn-1})\end{array}\right\}.$$

Similarly, the force $\dfrac{\partial\sigma_{i\phi}}{\partial x_i}$ due to the ice internal stress can be written as follows:

$$\frac{\partial\sigma_{i\theta}}{\partial x_i}=\frac{\partial}{\partial x_i}(2\eta\varepsilon_{i\theta}+\delta_{i\theta}((\zeta-\eta)\varepsilon_{kk}-P/2))$$

$$=\frac{\partial}{r\cos\theta\partial\phi}(2\eta\frac{1}{2}(\frac{1}{r\cos\theta}\frac{\partial u_\theta}{\partial\phi}+\frac{u_\phi\tan\theta}{r}+\frac{1}{r}\frac{\partial u_\phi}{\partial\theta}))$$

$$+\frac{\partial}{r\partial\theta}(2\eta\frac{1}{r}\frac{\partial u_\theta}{\partial\theta})+\frac{\partial}{r\partial\theta}((\zeta-\eta)(\frac{1}{r\cos\theta}\frac{\partial u_\phi}{\partial\phi}+\frac{u_\theta\tan\theta}{r}+\frac{1}{r}\frac{\partial u_\theta}{\partial\theta})-P/2)$$

$$=\frac{\partial}{r\partial\theta}((\zeta+\eta)\frac{1}{r}\frac{\partial u_\theta}{\partial\theta})+\frac{\partial}{r\cos\theta\partial\phi}(\eta\frac{1}{r\cos\theta}\frac{\partial u_\theta}{\partial\phi})$$

$$+\frac{\partial}{r\cos\theta\partial\phi}(\eta\frac{1}{r}\frac{\partial u_\phi}{\partial\theta})+\frac{\partial}{r\partial\theta}((\zeta-\eta)\frac{1}{r\cos\theta}\frac{\partial u_\phi}{\partial\phi})-\frac{\partial}{r\partial\theta}(P/2)$$

$$+\frac{\tan\theta}{r}\frac{\partial}{r\cos\theta\partial\phi}(\eta u_\phi)+\frac{\tan\theta}{r}\frac{\partial}{r\partial\theta}((\zeta-\eta)u_\theta)+\frac{\sec^2\theta}{r}\frac{(\zeta-\eta)u_\theta}{r}.$$

The discretized form of $\dfrac{\partial \sigma_{i\phi}}{\partial x_i}$ above becomes:

$$\frac{\partial \sigma_{i\theta}}{\partial x_i} \approx \frac{1}{2}\left(\frac{1}{r\Delta\theta}\right)^2$$

$$\left\{ \begin{array}{l} u_{\theta mn-1}(\eta_{m+1\,n}+\eta_{mn}+\zeta_{m+1\,n}+\zeta_{mn}) \\[4pt] -u_{\theta mn}(\eta_{m+1\,n}+\eta_{mn}+\eta_{m+1\,n+1}+\eta_{mn+1}+\zeta_{m+1\,n}+\zeta_{m\,n}+\zeta_{m+1\,n+1}+\zeta_{m\,n+1}) \\[4pt] +u_{\theta mn+1}(\eta_{m+1\,n+1}+\eta_{m\,n+1}+\zeta_{m+1\,n+1}+\zeta_{mn+1}) \end{array} \right\}$$

$$+\frac{1}{2}\left(\frac{1}{r\cos\theta\Delta\phi}\right)^2 \left\{ \begin{array}{l} u_{\phi m-1\,n}(\eta_{mn}+\eta_{mn+1})-u_{\phi m\,n}(\eta_{mn}+\eta_{m+1\,n}+\eta_{mn+1}+\eta_{m+1\,n+1}) \\[4pt] +u_{\phi m+1\,n}(\eta_{m+1\,n}+\eta_{m+1\,n+1}) \end{array} \right\}$$

$$+\frac{1}{4}\frac{1}{r^2\cos\theta\Delta\phi\Delta\theta} \left\{ \begin{array}{l} \eta_{m+1\,n+1}(u_{\theta m+1\,n+1}+u_{\theta m\,n+1}-u_{\theta m+1\,n}-u_{\theta mn}) \\[4pt] +\eta_{m+1\,n}(u_{\theta m+1\,n}+u_{\theta mn}-u_{\theta m+1\,n-1}-u_{\theta m\,n-1}) \\[4pt] +\eta_{m\,1+n}(u_{\theta m\,n}+u_{\theta m-1\,n}-u_{\theta m\,n+1}-u_{\theta m-1\,n+1}) \\[4pt] +\eta_{m\,n}(u_{\theta m\,n-1}+u_{\theta m-1\,n-1}-u_{\theta m\,n}-u_{\theta m-1\,n}) \end{array} \right\}$$

$$+\frac{1}{4}\frac{1}{r^2\cos\theta\Delta\phi\Delta\theta} \left\{ \begin{array}{l} (\zeta_{m+1\,n+1}-\eta_{m+1\,n+1})(u_{\phi m\,+1\,n+1}+u_{\phi m\,+1\,n}-u_{\phi mn-1}-u_{\phi mn}) \\[4pt] +(\zeta_{mn+1}-\eta_{mn+1})(u_{\phi mn+1}+u_{\phi mn}-u_{\phi m-1\,n+1}-u_{\phi m-1\,n}) \\[4pt] +(\zeta_{m+1\,n}-\eta_{m+1\,n})(u_{\phi m\,n}+u_{\phi m\,n-1}-u_{\phi m+1\,n}-u_{\phi m+1\,n-1}) \\[4pt] +(\zeta_{m\,n}-\eta_{m\,n})(u_{\phi m-1\,n}+u_{\phi m\,-1\,n-1}-u_{\phi mn}-u_{\phi mn-1}) \end{array} \right\}$$

$$-\frac{1}{r\Delta\theta}(P/2)+\frac{\tan\theta}{r}\frac{1}{r\cos\theta\Delta\phi}\frac{1}{4}\left\{ u_{\phi m+1\,n}(\eta_{m\,n+1}+\eta_{mn})-u_{\phi m-1\,n}(\eta_{mn}+\eta_{m\,n-1}) \right\}$$

$$+\frac{\tan\theta}{r}\frac{1}{r\Delta\theta}\frac{1}{4}\left\{ \begin{array}{l} u_{\theta mn+1}(\zeta_{m+1\,n}+\zeta_{mn}-\eta_{m+1\,n}-\eta_{mn}) \\[4pt] -u_{\theta mn-1}(\zeta_{mn}+\zeta_{m-1\,n}-\eta_{mn}-\eta_{m-1\,n}) \end{array} \right\}$$

$$+\frac{\sec^2\theta}{r}\frac{1}{4r}u_{\theta mn}(\zeta_{mn}+\zeta_{mn+1}+\zeta_{m+1\,n}+\zeta_{m+1\,n+1}$$

$$-\eta_{mn}-\eta_{mn+1}-\eta_{m+1\,n}-\eta_{m+1n+1}).$$

4.0 THE CONTINUITY EQUATION FOR ICE CONCENTRATION AND THICKNESS

The continuity equation for ice concentration is written as follows [Hibler 1979]:

$$\frac{\partial A}{\partial t} + \nabla \cdot \left(\mathbf{u} A \right) = S_A + \text{(diffusion)},\tag{3}$$

where A represents the ice concentration,

$\nabla \cdot (\mathbf{u}A)$ is the advection term for ice concentration,

S_A is the ice growth rate (i.e., a thermodynamic term due to atmospheric and oceanic forcing), and the diffusion term, usually small, is mainly used to stabilize the numerical algorithm.

Again, as with Eq. (1), the temporal term $\frac{\partial A}{\partial t}$ would not be affected by transforming the coordinates from Cartesian to spherical. Its form remains the same in the spherical version of the continuity equation.

The advection term $\nabla \cdot (\mathbf{u}A)$ in spherical coordinates is transformed as follows:

$$\nabla \cdot (\mathbf{u}\, A) = \frac{-\tan\theta}{r}\, u_\theta A + \frac{1}{r}\frac{\partial(u_\theta A)}{\partial\theta} + \frac{1}{r\cos\theta}\frac{\partial(u_\phi A)}{\partial\phi}\ .$$

The extra term $\dfrac{-\tan\theta}{r}\, u_\theta A$ is a result of the coordinate transformation.

The diffusion term is a sum of two terms $\nabla^2 A$ and $\nabla^2\nabla^2 A$, which transform as follows:

$$\nabla^2 A = \frac{-\tan\theta}{r^2}\frac{\partial A}{\partial\theta} + \frac{1}{r^2}\frac{\partial^2 A}{\partial\theta^2} + \frac{1}{r^2\cos^2\theta}\frac{\partial^2 A}{\partial\phi^2}\ \text{and}$$

$$\nabla^2\,(\nabla^2 A) = \frac{-\tan\theta}{r^2}\frac{\partial\nabla^2 A}{\partial\theta} + \frac{1}{r^2}\frac{\partial^2\nabla^2 A}{\partial\theta^2} + \frac{1}{r^2\cos^2\theta}\frac{\partial^2\nabla^2 A}{\partial\phi^2}\ .$$

The thermodynamic term S_A is expressed as follows:

$$S_A = \frac{f(0)}{h_0}(1-A)H(f(0)) + \frac{A}{2h}S_h H(f(h/A)),$$

where $f(0)$ is the growth rate of ice thickness in open water,

$H(x)$ is the Heaviside step function, and equals 1 for $x > 0$ and 0 otherwise,

h represents the ice thickness, and h_0 is set to be 0.5 m,

S_h is the net ice growth or melt, and equals $f(h/A)A + f(0)(1-A)$, and

$f(h/A)$ is the growth rate of ice thickness h/A.

The function $f(0)$ becomes the growth rate due to the atmospheric cooling after all the mixed-layer heat above the freezing temperature is used [Cheng and Preller 1992; 1994]. The mixed-layer temperature used here comes from the Cox ocean model that is the basis of the ice-ocean coupled model.

Note that the Hibler ice model [Hibler 1979; 1980] calculates the atmospheric heating of the mixed layer as a negative ice growth rate. In PIPS2.0, that heating comes to the mixed layer from the ocean model. Further discussions about the negative ice growth rate, the mixed-layer temperature, and the oceanic heat flux can be found in Sec. 12.0 of this report.

All changes discussed above for the continuity equation for ice concentration apply as well to the continuity equation for ice thickness. The derivation of the thickness equation, which has been omitted here, is completely analogous, except that the S_A term is replaced by S_h for the thickness equation.

5.0 MODEL COMPARISON IN THE PIPS DOMAIN

The spherical coordinate version of PIPS was compared here with the Cartesian version of PIPS to ensure that no discernible inaccuracies were introduced during the coordinate transformation. During the test, 1986 NOGAPS winds were used for atmospheric forcing and the monthly oceanic forcing was provided by Hibler and Bryan [1987]. Both the Cartesian and the spherical coordinate ice models were spun up for 3 yr with the following initial conditions: 3-m ice thickness, 100% ice concentration, and zero ice velocity. Figures 5.1a, 5.2a, and 5.3a show ice velocity, thickness, and concentration, respectively, for 17 Jan 1986, computed from the spherical coordinate PIPS model. Figures 5.1b, 5.2b, and 5.3b show the same quantities for the Cartesian model. There are no visible differences between Figs. 5.1a and 5.1b, 5.2a and 5.2b, and 5.3a and 5.3b, although numerical differences of a few percent exist. The model comparison demonstrates that (1) both models give almost identical results, and (2) the transformed PIPS model can be applied to cover most sea ice regions in the Northern Hemisphere without numerical difficulties [Cheng and Preller 1992; Holland et al. 1994].

6.0 PIPS DOMAIN IN THE NORTHERN HEMISPHERE

Recasting the ice-ocean model in spherical coordinates provides a different polar grid on which to calculate ice and ocean conditions from the one that was used for the Cartesian model calculations (see Fig. 1.1). Figure 6.1 shows the PIPS2.0 model domain on a stereographic projection of the Northern Hemisphere (the hatched area). The domain includes the Gulf of St. Lawrence, the Labrador Sea, Baffin Bay, Hudson Bay, the Baltic Sea, the Yellow Sea, the Sea of Okhotsk, the Bering Sea, and many other seas of the Arctic and sub-Arctic (Fig. 6.2). This domain allows no sea ice inflow or outflow as boundary conditions because no sea ice exists as far south as 20°–30° N. (Note that since sea ice is the main interest, the following seas and lakes are ignored: the five Great Lakes of North America, the Mediterranean Sea, and the Caspian Sea.)

Figure 6.1 was drawn for every fourth grid line and has 360 × 360 grid cells, each with an arc length of approximately 0.28575° for both sides of the grid square. Note that at the North Pole, the equal angular measures for the grid square sides translate into equal linear dimensions of approximately 32 km. However, the grid cell at the top boundary of Fig. 6.1 shows the most linear inequality for the grid dimensions (i.e., approximately 17 × 32 km). In the new model domain, the equator that
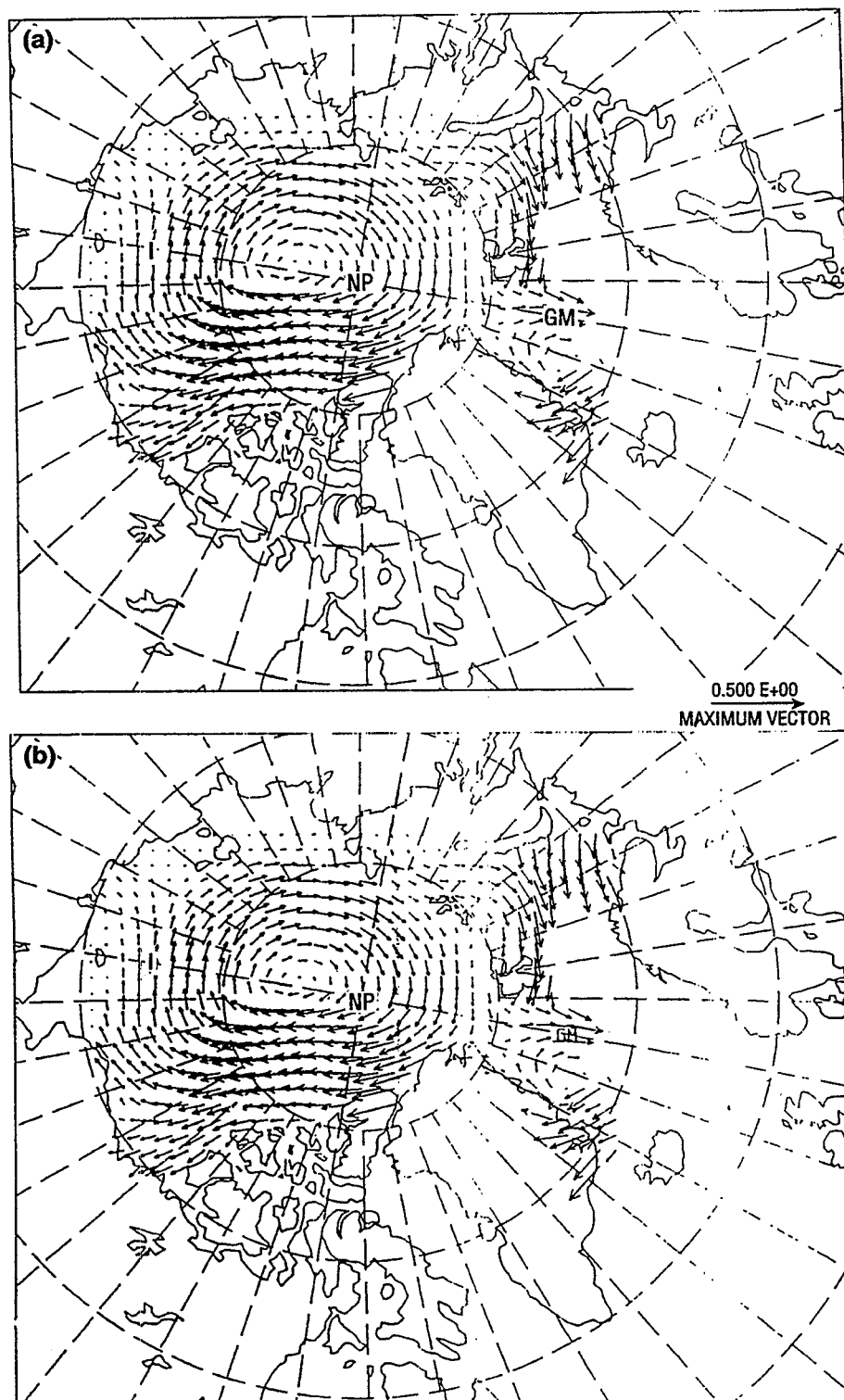
Fig. 5.1 — Modeled ice-drift velocity from PIPS model coordinates: (a) spherical and (b) Cartesian. Scale of maximum vector is 0.5 m/s.
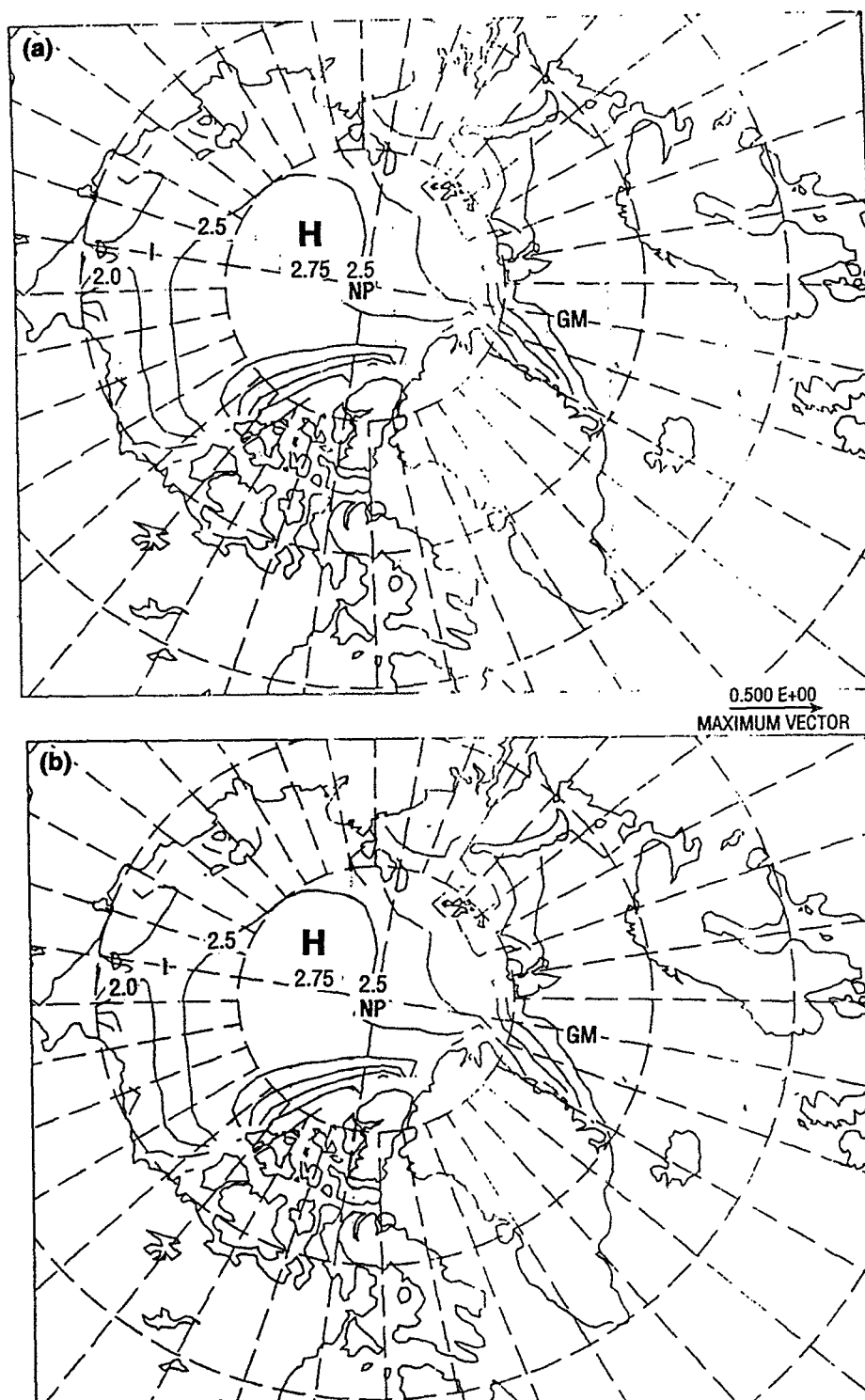
Fig. 5.2 — Modeled ice thickness from PIPS model coordinates: (a) spherical and (b) Cartesian. Thickness in meters, interval 0.5 m.
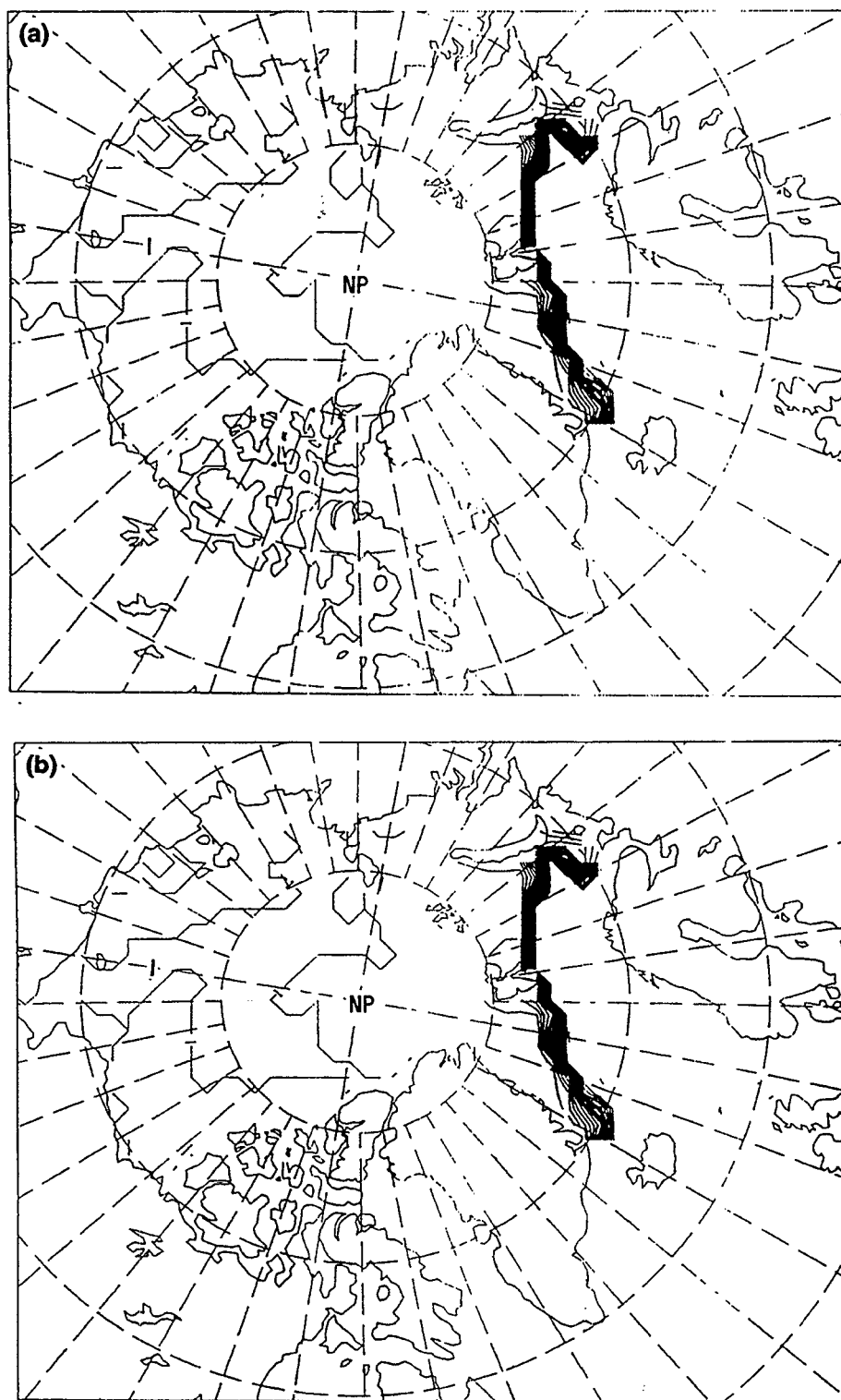
Fig. 5.3 — Modeled ice concentration from PIPS model coordinates: (a) spherical
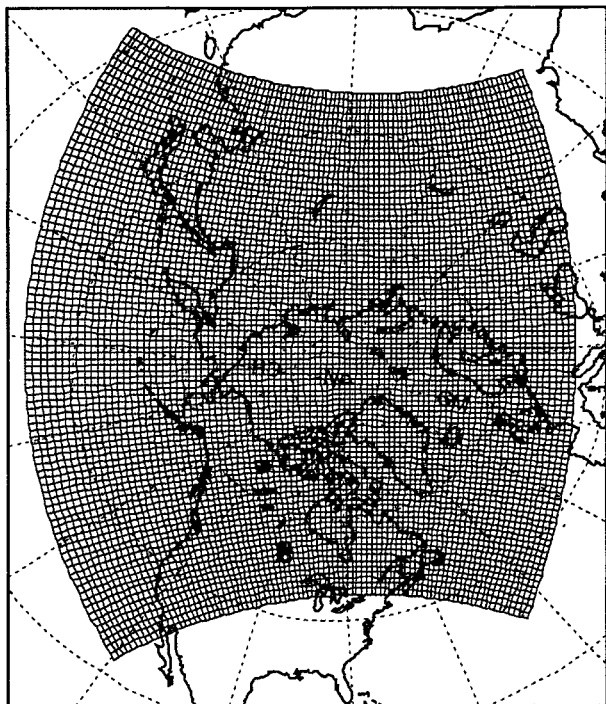and (b) Cartesian. Concentration ranges are from 0 to 1.

Fig. 6.1 — PIPS2.0 domain with the variable resolution grid overlaid. The hatched lines are drawn at every fourth grid point including land points.
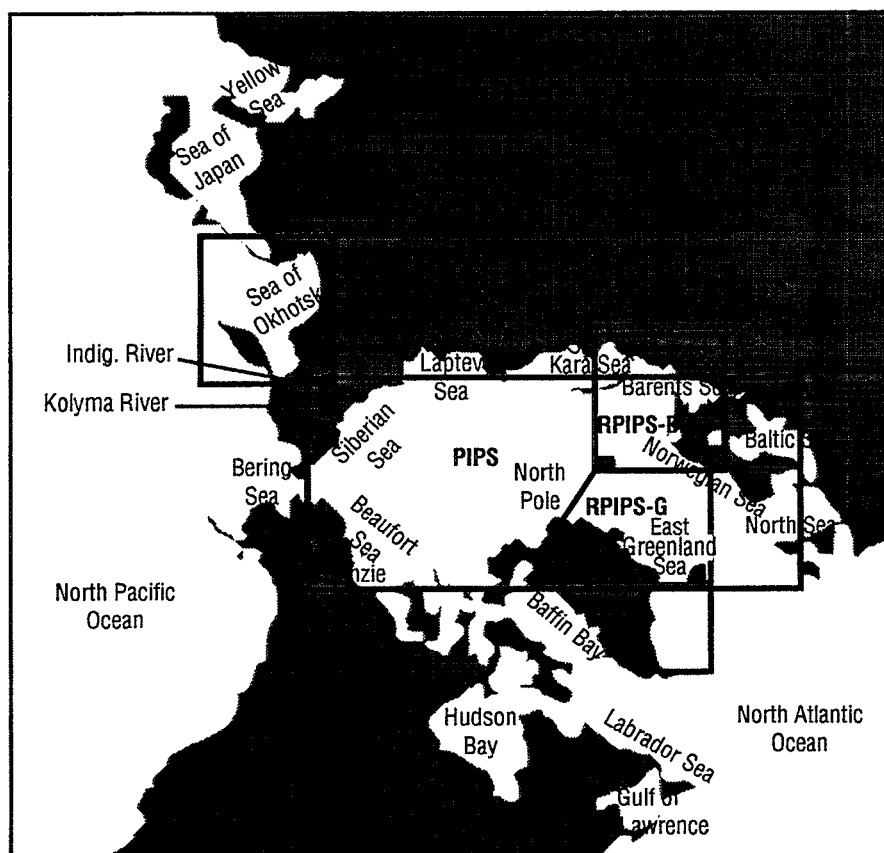

Fig. 6.2 — The PIPS2.0 model domain, is equivalent to the hatched area in Fig. 6.1, is plotted with the same arc distance, 0.28575°, for both vertical and horizontal axes.

is defined by the polar rotation lies on the 170° W–10° E great circle that passes through the North Pole.

7.0 ATMOSPHERIC FORCING

The atmospheric forcing includes incoming solar radiation, sensible heat flux, total heat flux, surface air temperature, atmospheric pressure, and vapor pressure. Oceanic and atmospheric heat fluxes contribute to a heat balance equation that allows the calculation of ice growth/decay. Ocean currents in the top mixed layer and the geostrophic wind stress are used to calculate ice motion.

The 1986 daily NOGAPS atmospheric forcing was used to compute monthly averages that were interpolated into the PIPS2.0 domain using two-dimensional cubic splines to provide the necessary forcing fields. As examples of the kinds of data produced by this procedure, Figs. 7.1 and 7.2 show the monthly NOGAPS geostrophic winds and surface air temperature averages, respectively. The winds were computed from the pressure fields using the geostrophic approximation. The wind velocities were plotted at every fourth point of the PIPS2.0 grid.

Because of such weather features as cyclones, wind magnitudes and directions vary throughout the year in the Arctic. Sea ice motion changes follow accordingly. Westerly winds prevail for most of the year in the North Pacific and North Atlantic Oceans, but the winds become somewhat more random during the summer.

Long-wavelength radiation was calculated based on the total heat flux, the sensible heat flux, and the incoming solar radiation from the NOGAPS data fields. Boltzmann radiation is included in the computed long-wavelength radiation. The incoming solar radiation is defined as positive in all calculations (i.e., heat flow into the sea ice and water is positive). Small negative values that occur during the balance calculations with the other heat sources are probably caused by errors in the interpolation from the NOGAPS model grid to the ice/ocean model grid. Therefore, these small errors are set to zero in the calculations.

General comments describing the Arctic input data will be useful in understanding the results of running the sea ice model that follows. Incoming solar radiation decreases with latitude. In the Arctic, vapor pressures are small from late fall to early spring, but reach up to 10 mbar during the rest of the year. In general, vapor pressures decrease with latitude. Sensible heat fluxes seem to be randomly distributed in the Arctic throughout the year, but they generally increase south of the Arctic.

The NOGAPS forcing fields in the 63 × 63 FNMOC grid of the Northern Hemisphere have a horizontal resolution for each grid cell of approximately 380 km. That spatial resolution is too coarse to resolve some regions (such as the Baltic Sea, the Yellow Sea, the Sea of Okhotsk, the Gulf of St. Lawrence, the Labrador Sea, and Baffin Bay). The NOGAPS data must be interpolated, which can introduce error into the fields for grid squares close to land. Estimates of ice drift velocity, thickness, and concentration produced by the research version of PIPS2.0, which includes the interpolation, could be biased. In operation, when implemented at FNMOC, the coupled model (PIPS2.0) will use the NOGAPS fine spatial resolution data fields (i.e., 1° × 1° in longitudes and latitudes) for calculations. The error in interpolated forcing fields should be reduced considerably.

Another source of error in the PIPS2.0 model has to do with how the wind stress is implemented. Instead of surface winds and their stresses, monthly geostrophic winds and a corresponding drag
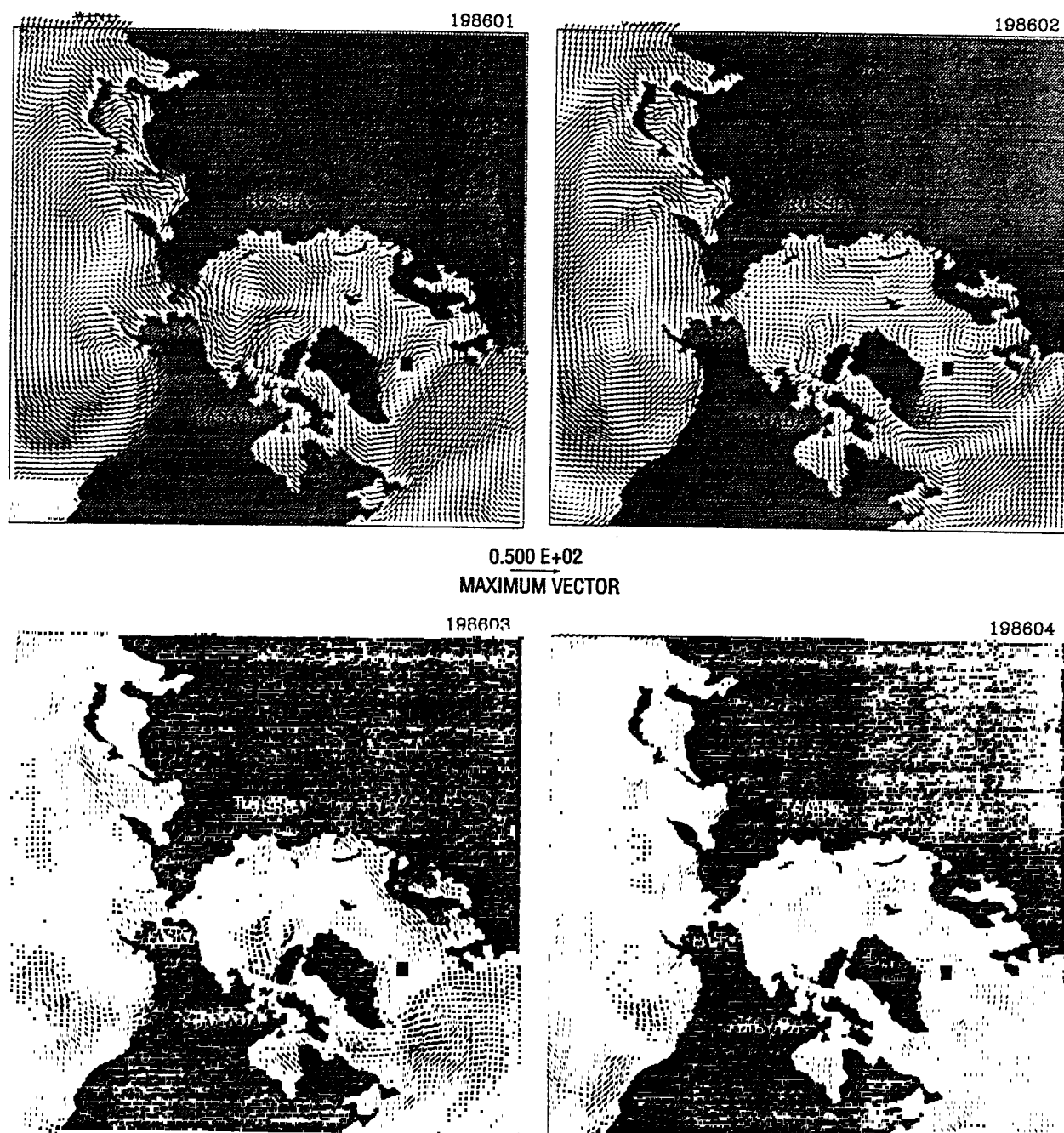
0.500 E+02
MAXIMUM VECTOR

Fig. 7.1 — Monthly NOGAPS geostrophic winds (m/s), Jan–Dec 1986

198605

198606

0.500 E+02
MAXIMUM VECTOR

198607

198608

Fig. 7.1 — cont.

198609

198610

0.500 E+02
MAXIMUM VECTOR

198611

198612
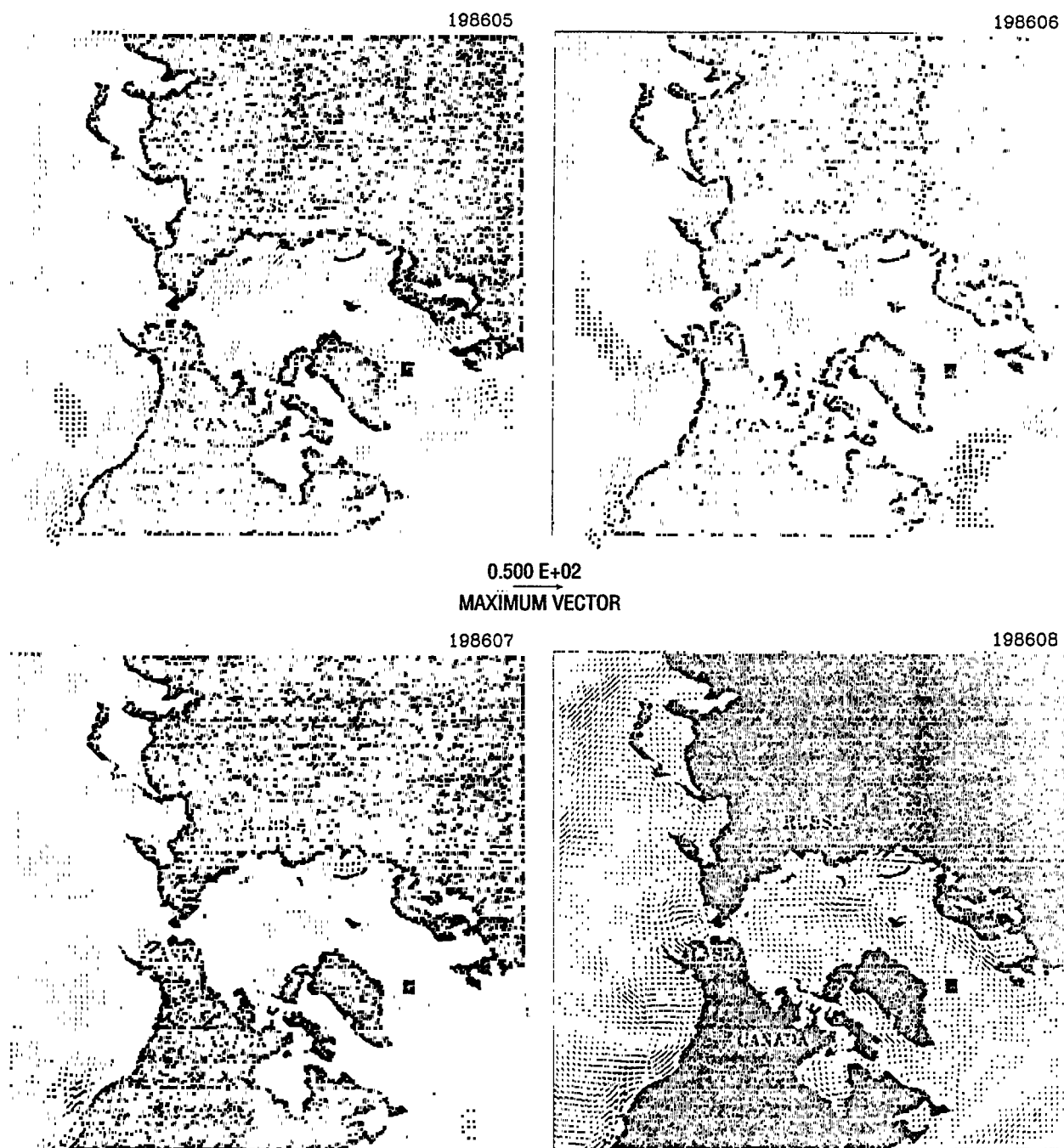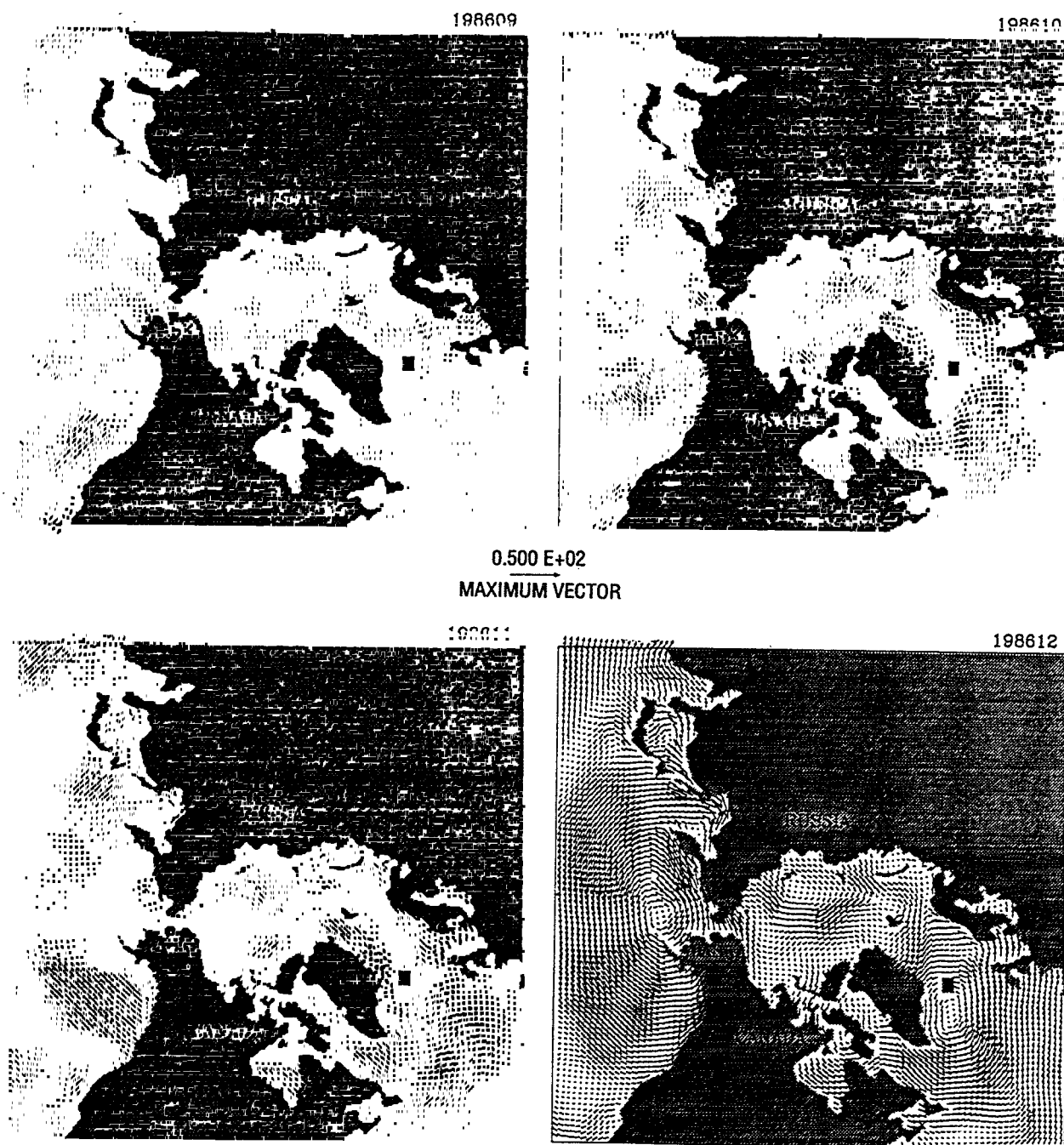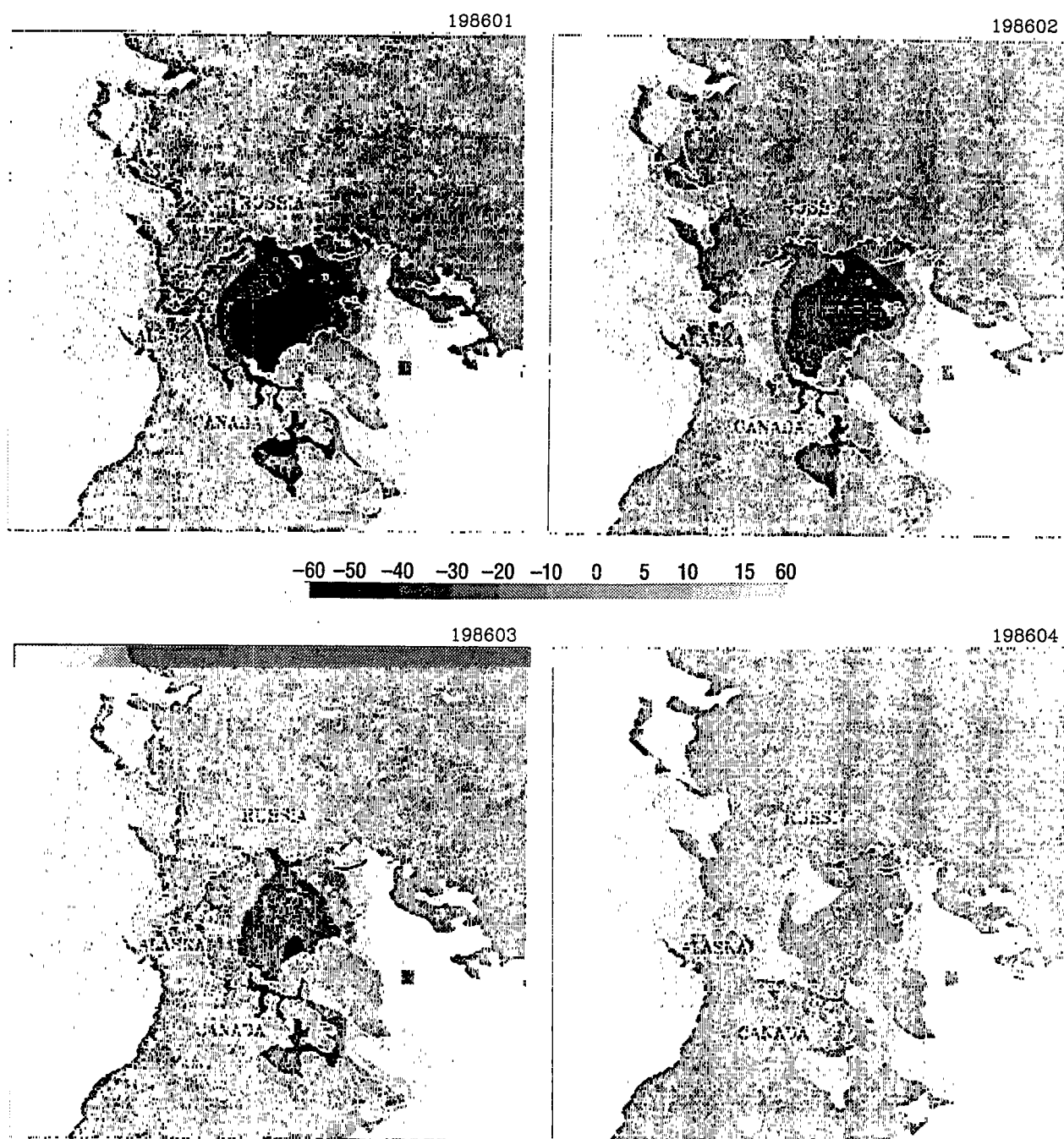
Fig. 7.1 — cont.

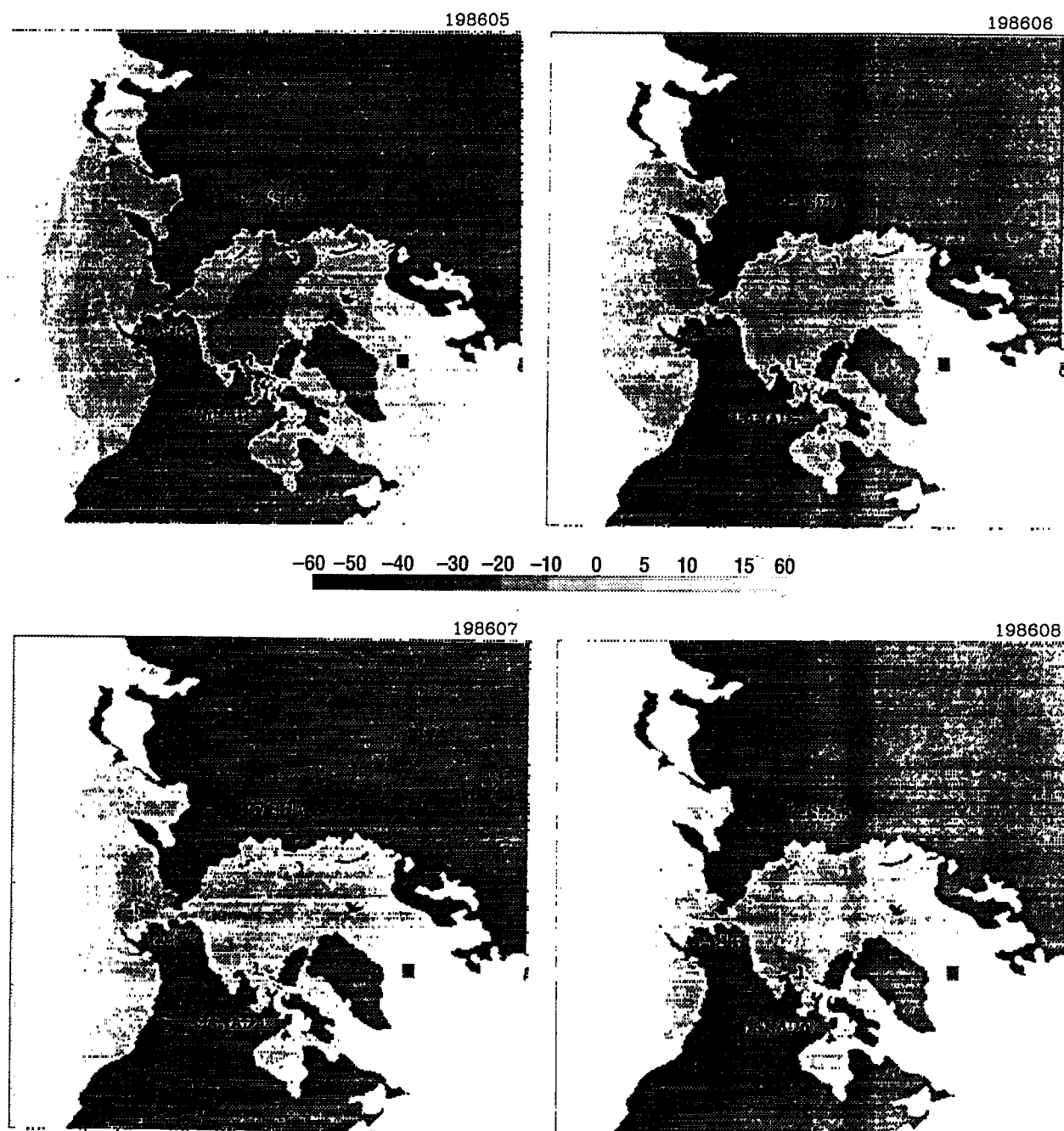Fig. 7.2 — Monthly NOGAPS surface air temperature, Jan–Dec 1986 (°C)
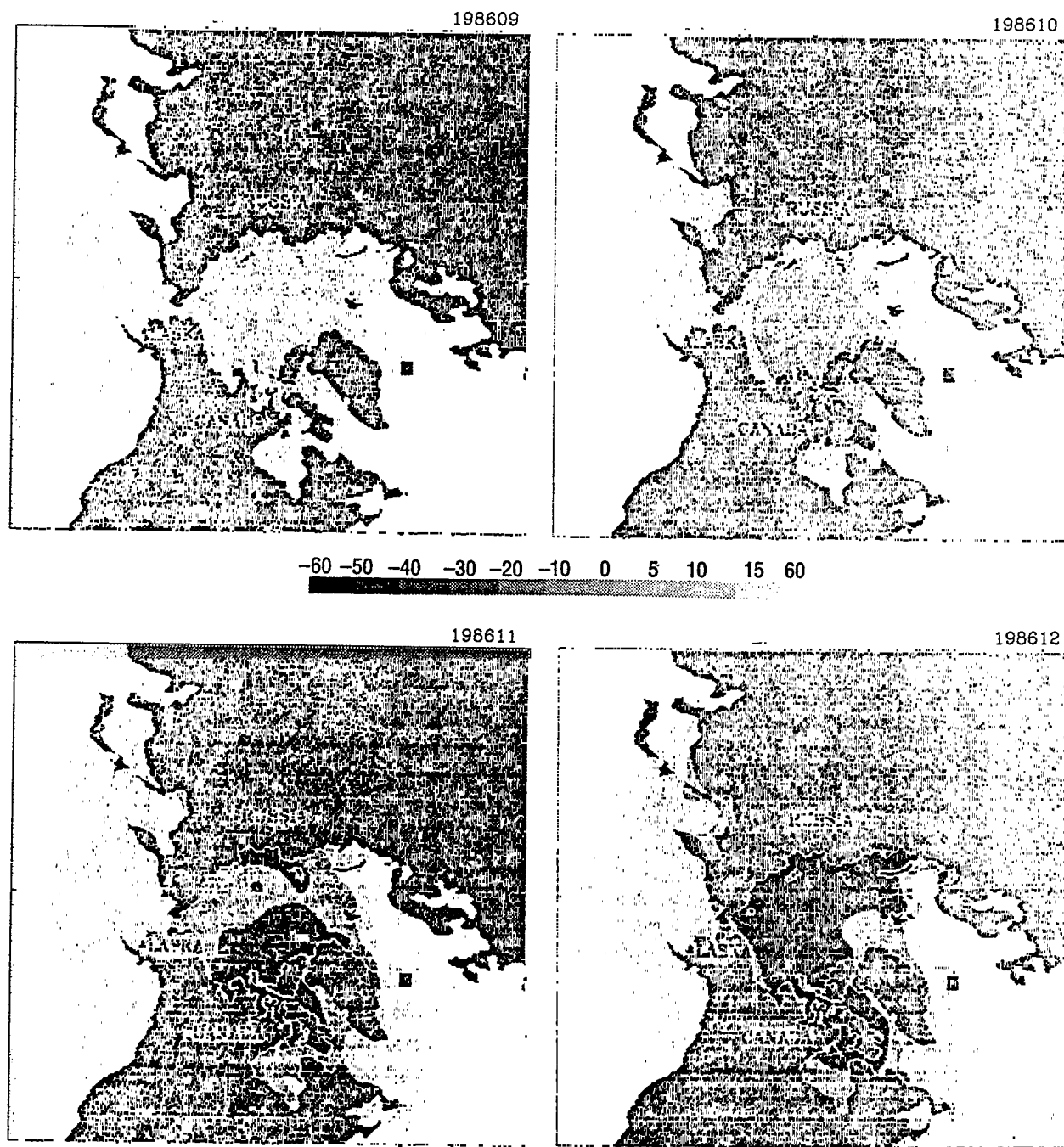
Fig. 7.2 — cont.

Fig. 7.2 — cont.

coefficient 0.001 were used to drive the coupled model as an expedient way of speeding up the model execution and as a useful and accurate approximation for some ocean areas. In the Arctic, the North Pacific, and the North Atlantic Oceans, this geostrophic approximation works reasonably well because of the expanses of open water. However, the accuracy of the results is suspect near coasts, such as the southeast Bering Sea between Alaska and the Aleutian Islands, because the wind estimates are affected by the water/land interfaces. When implementation of the PIPS2.0 model is complete at FNMOC, the geostrophic wind and pressure fields will be replaced by NOGAPS surface wind stress, which will address this problem for operations.

8.0 THE COX OCEAN MODEL

In his original work on Arctic ice modeling [1987], Hibler used the Cox ocean model [1984] to provide the oceanic forcing for the water components of the momentum and heat flow calculations. The PIPS ice growth model retained this dependence on the Cox ocean model although mainly for the sake of convenience, as the PIPS investigators were occupied with including other features in the model. The Cox ocean model provides oceanic forcing for the ice models: namely, the ocean currents, the mixed-layer temperature and salinity, and the oceanic heat fluxes. This section describes the version of the Cox ocean model that was used for PIPS2.0, as well as the procedures that were used to execute it.

The Cox ocean model is a three-dimensional, primitive equation numerical model for large-scale baroclinic ocean circulation. The model was spun up from a motionless initial ocean state for 5 yr of model time to develop steady-state oceanic characteristics. These characteristics were used as initial values for the ice-ocean coupled model. Sarmiento and Bryan's robust method [1982] was used during the spin-up to constrain temperature and salinity in the top mixed layer with 30 day, and then to constrain temperature and salinity in the rest of the levels with 3 yr.

The parameters and data for the spin-up initialization are as follows. The coefficients of horizontal eddy diffusion, vertical eddy diffusion, horizontal eddy viscosity, and horizontal eddy viscosity are $10^7 \text{cm}^2\text{s}^{-1}$, $1 \text{ cm}^2\text{s}^{-1}$, $10^9 \text{ cm}^2\text{s}^{-1}$, and $1 \text{ cm}^2\text{s}^{-1}$, respectively. The timestep is 1 hr for temperature and salinity, and 0.1 hr for ocean currents and stream functions (i.e., the distorted physics method of Bryan [1984]). The 1986 annual NOGAPS geostrophic winds and the Levitus annual climatological data [1982] were used in this 5-yr spin-up process.

Assumptions made in the implementation of the Cox model manifest themselves with signatures in the data that the PIPS model produces during runs. Those assumptions, as well as the signatures that they produce, are discussed in Secs. 13.0 and 14.0.

9.0 OCEAN-BOTTOM TOPOGRAPHY

To support studies using the Cox ocean model, the NOAA-NGDC Earth Topography System, Version 5 (ETOPO5) bathymetric data were interpolated into the PIPS2.0 domain and grid using the cubic splines. Figure 9.1 shows the ocean-bottom topography of this model domain. The topography was smoothed to avoid numerical difficulties in the Cox ocean model by integrating the cubic spline function and then averaging it over every 3 × 3 grid squares to represent the center square's topography.
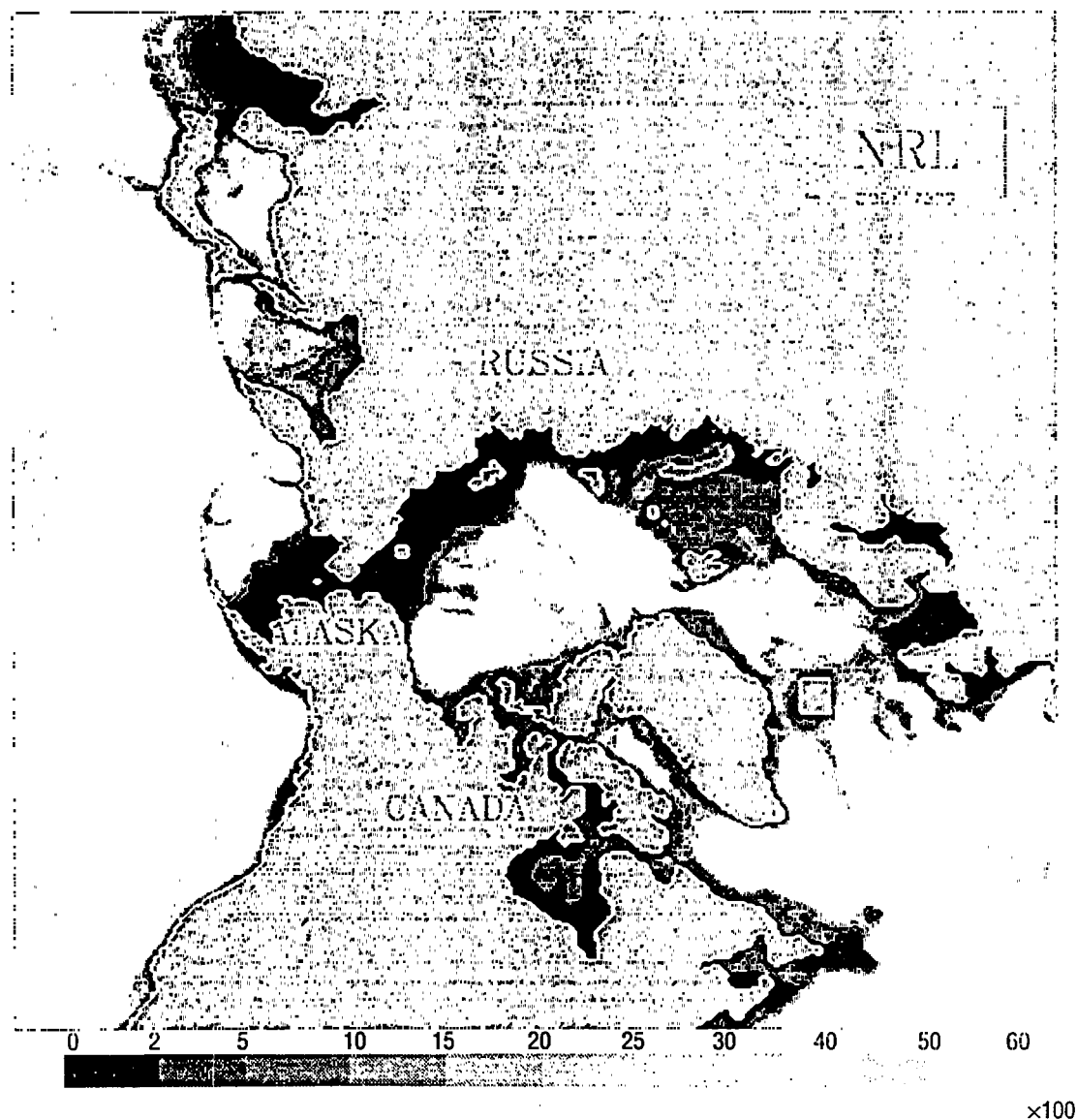
Fig. 9.1 — Bottom topography in PIPS2.0 domain according to ETOPO5. Scale range from 0–6000 m.

The topography was divided into 15 levels, according to the requirements of the Cox ocean model [1984]. Several channels and straits were too narrow to appear as waterways after this averaging technique was used. Examples are the English Channel and the channel between the fresh-water Baltic Sea and the salt-water North Sea. In addition, some small islands were averaged with adjacent deep trenches and became sea gridpoints. Where it is important to have land topography, island points such as some of the Kuril Islands and the Aleutian Islands, have been manually edited back. Table 9.1 lists the level depths and the thickness of each ocean layer for bottom topography used by the Cox ocean model. Any bottom topography from the data set deeper than the Level 15 definition (5700 m) was set to that depth for this study. Similar adjustments were made on the Levitus climatological data of temperature and salinity (see Sec. 10.0) when applied to studies involving the PIPS2.0 domain. Model ocean currents at depth could be biased by such adjustments near and in deep trenches.

Table 9.1 — Level Depths and Thicknesses of Bottom Topography for the Cox Ocean Model

Level	Thickness (m)	Center Depth (m)	Depth (m)
1	30.0	15.0	30.0
2	46.3	53.1	76.3
3	67.4	110.0	143.7
4	94.5	191.0	238.2
5	128.5	302.4	366.7
6	170.6	451.9	537.2
7	221.9	648.2	759.1
8	283.5	900.0	1042.7
9	356.2	1220.8	1398.9
10	440.6	1619.1	1839.4
11	536.8	2107.8	2376.2
12	644.5	2698.5	3020.8
13	763.0	3402.3	3783.8
14	890.7	4229.1	4674.5
15	1025.5	5187.2	5700.0

Level 1, a 30-m-thick layer that interacts with sea ice and atmosphere, was chosen to represent an average depth for the mixed layer in the Arctic. In the summer, the mixed layer is much deeper than Level 1, probably reaching down to Level 4 or 5.

10.0 LEVITUS CLIMATOLOGICAL DATA

Three-dimensional salinity and temperature fields for initialization of the PIPS2.0 model were prepared from the Levitus climatological data set. Seasonal and annual data were used to make monthly temperature and salinity estimates, which were interpolated into the model domain according to the 15 levels of bottom topography. Figures 10.1 and 10.2 show the top mixed-layer temperature throughout the year and the salinity of the mixed layer, respectively, for the PIPS2.0 domain.

The interpolation procedure is as follows. The monthly data are extrapolated from the sea grid to nearby land gridpoints. The extrapolated data are then used to compute three-dimensional cubic spline functions in longitude, latitude, and depth. The cubic splines are then used to interpolate the data set onto the PIPS2.0 grid. The horizontal spatial resolution of the Levitus data is 1° × 1° in the oceans. Therefore, when those data are extrapolated on to the PIPS2.0 grid (0.28575° × 0.28575°) near coasts, narrow straits, channels, or semi-enclosed seas, the accuracy becomes questionable.

A review of the data and general trends from the Levitus data set may help in understanding the study results to be presented in Sec. 13.0. Water temperatures in the Arctic generally decrease with increasing latitude. The water temperature is usually 2°–6° warmer in summer than in winter throughout the domain, except where permanent sea ice is present (the Central Arctic). The temperature there remains at the freezing point for most of the year. The salinity is 3–6 ppt lower in the western Arctic than in the eastern Arctic. The western Arctic obtains fresh water from the Siberian and Alaskan rivers, while the eastern Arctic is mixed with salty North Atlantic water. The salinity in the North Pacific is lower than in the North Atlantic Ocean, the Norwegian Sea, and the East Greenland Seas.

11.0 RIVER RUNOFF

The ice-ocean coupled model includes runoff from eight major rivers (Table 11.1), as suggested by Aagaard and Carmack [1989]. The Severnaya Dvina River is not used in the modeling because the White Sea to which it flows is closed from other Arctic seas. Based on Shiklomanov and
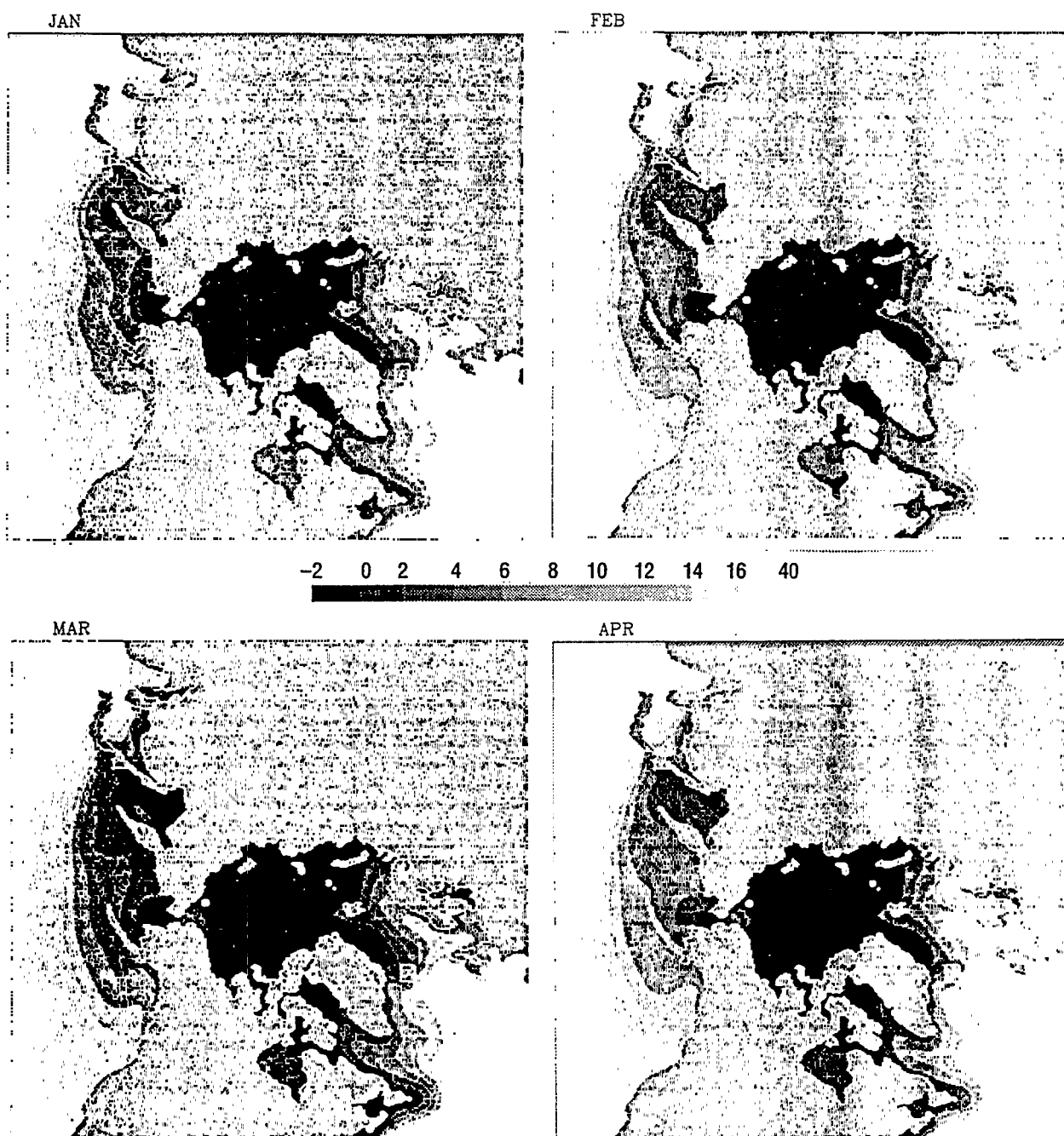
Fig. 10.1 — Monthly Levitus climatological data of temperature (°C) at 15 m
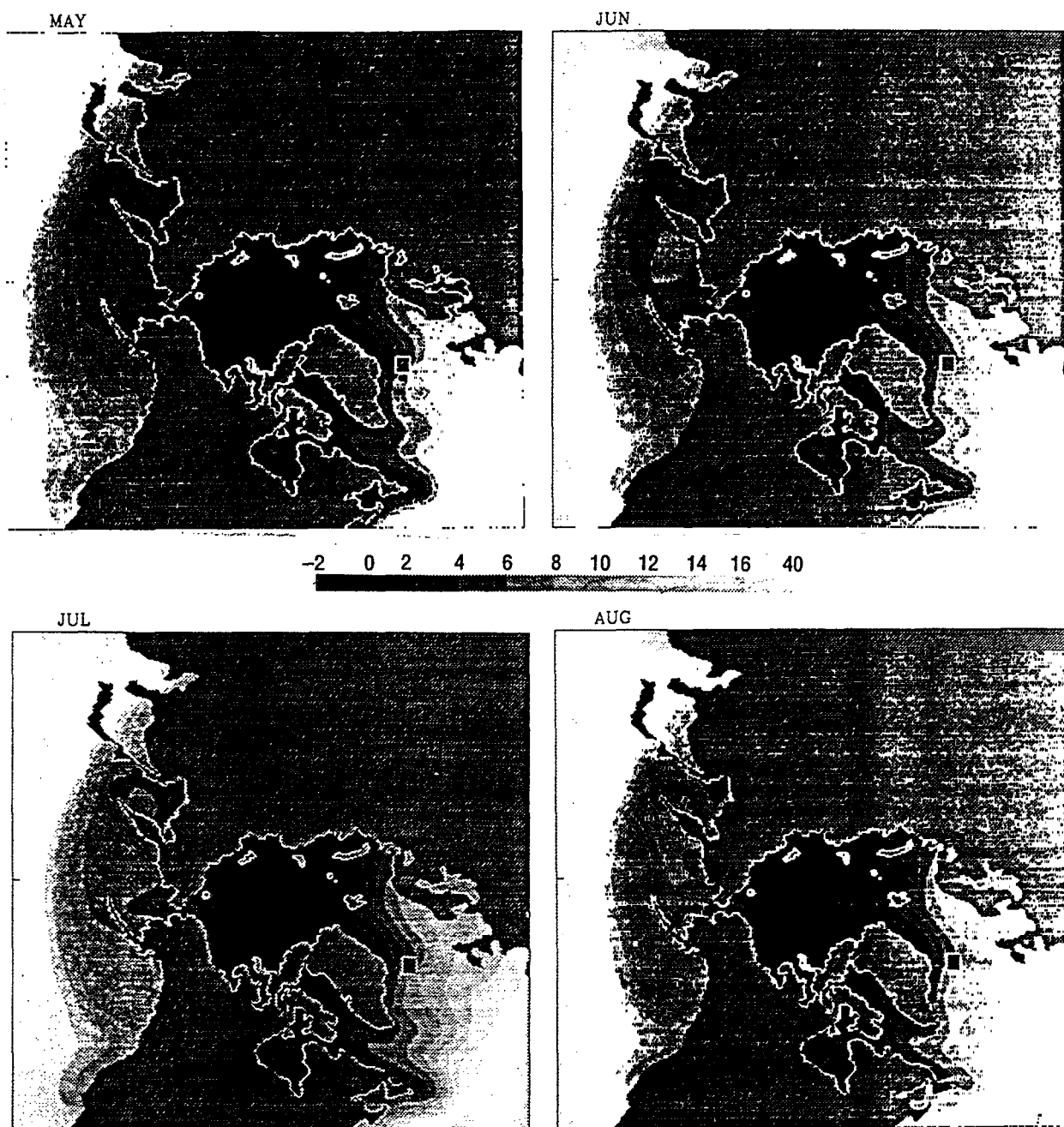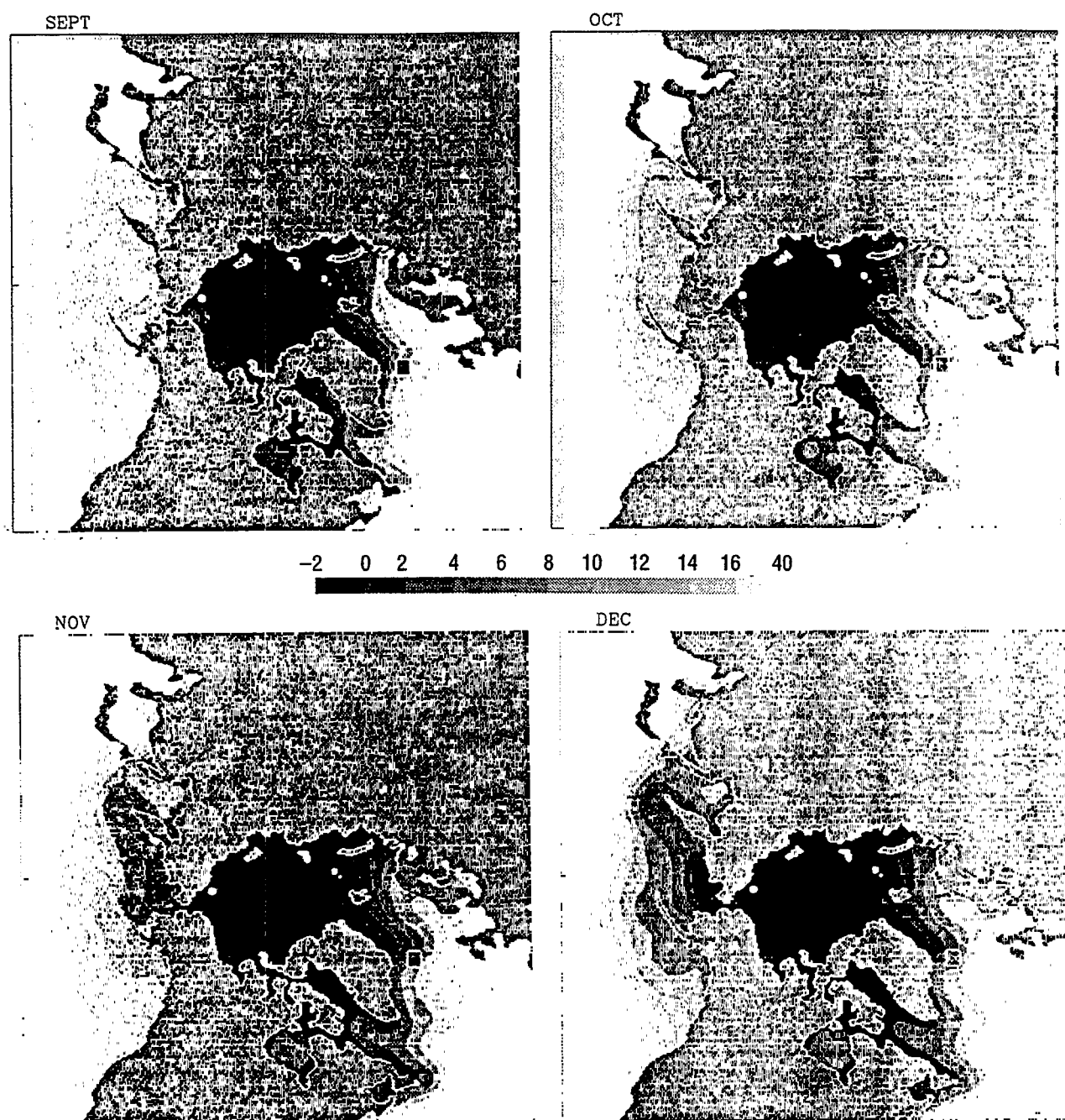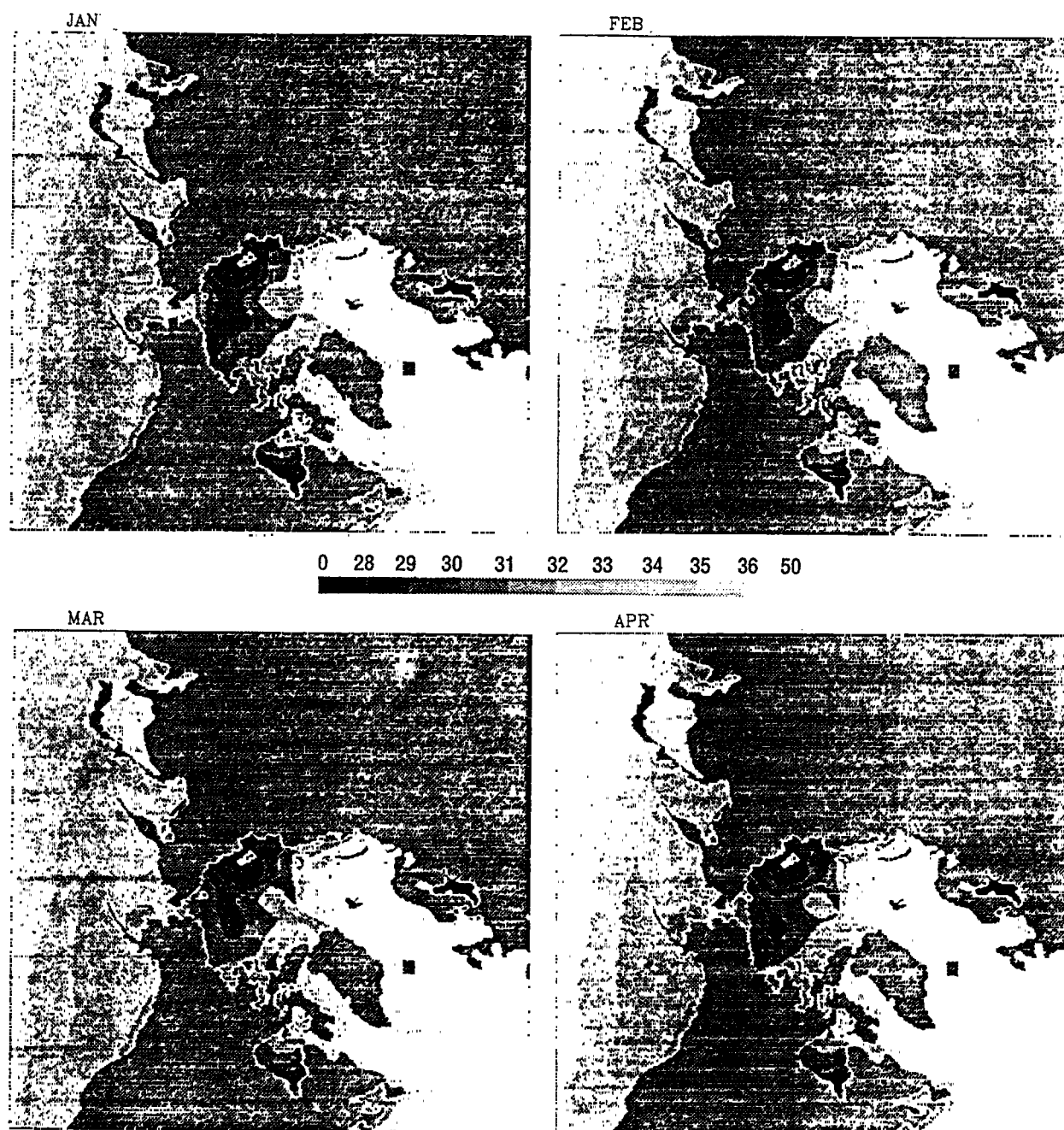
Fig. 10.1 — cont.

Fig. 10.1 — cont.

Fig. 10.2 — Monthly Levitus climatological data of salinity (ppt) at 15 m

Fig. 10.2 — cont.

SEP

OCT

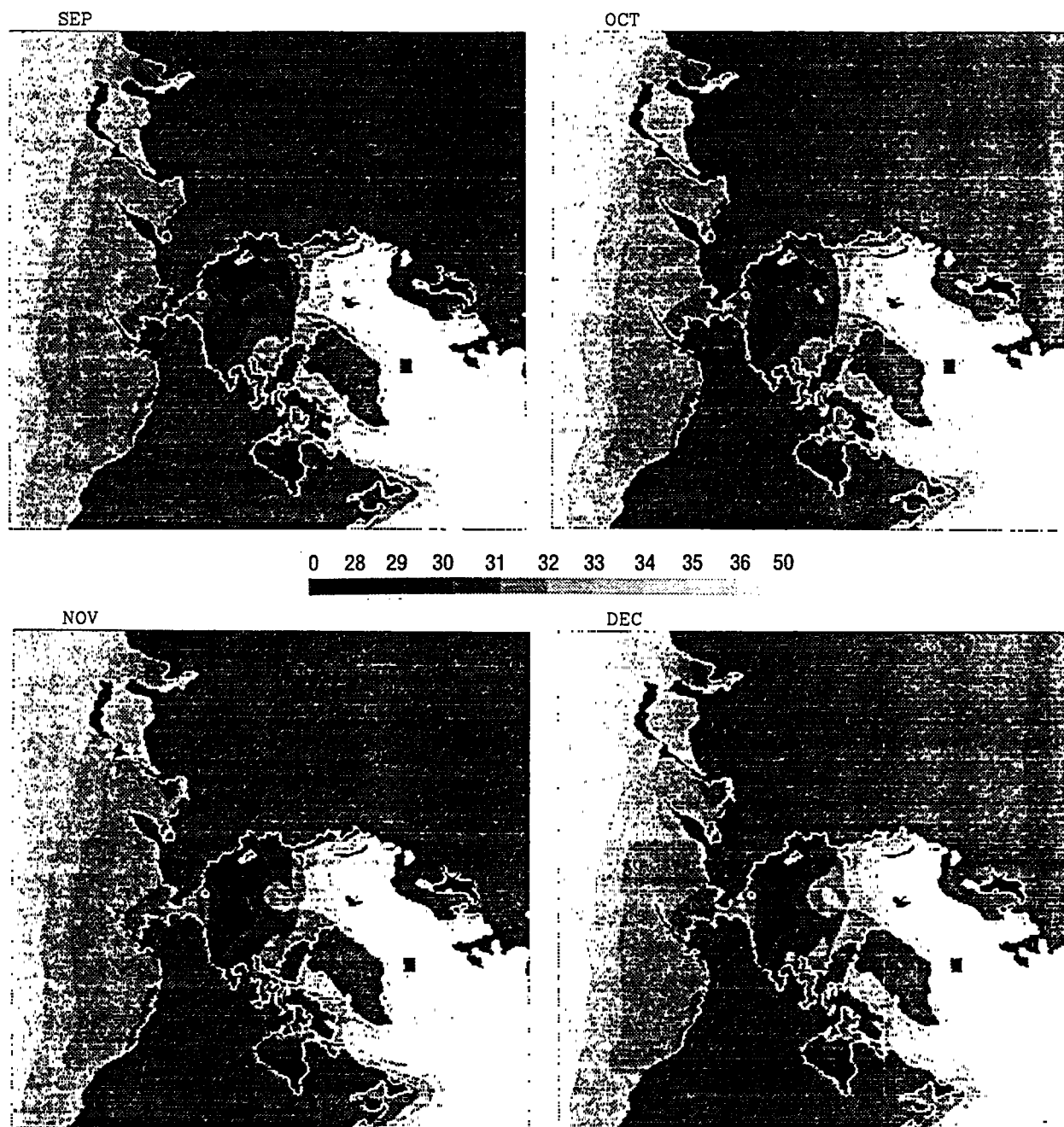0   28   29   30   31   32   33   34   35   36   50

NOV

DEC
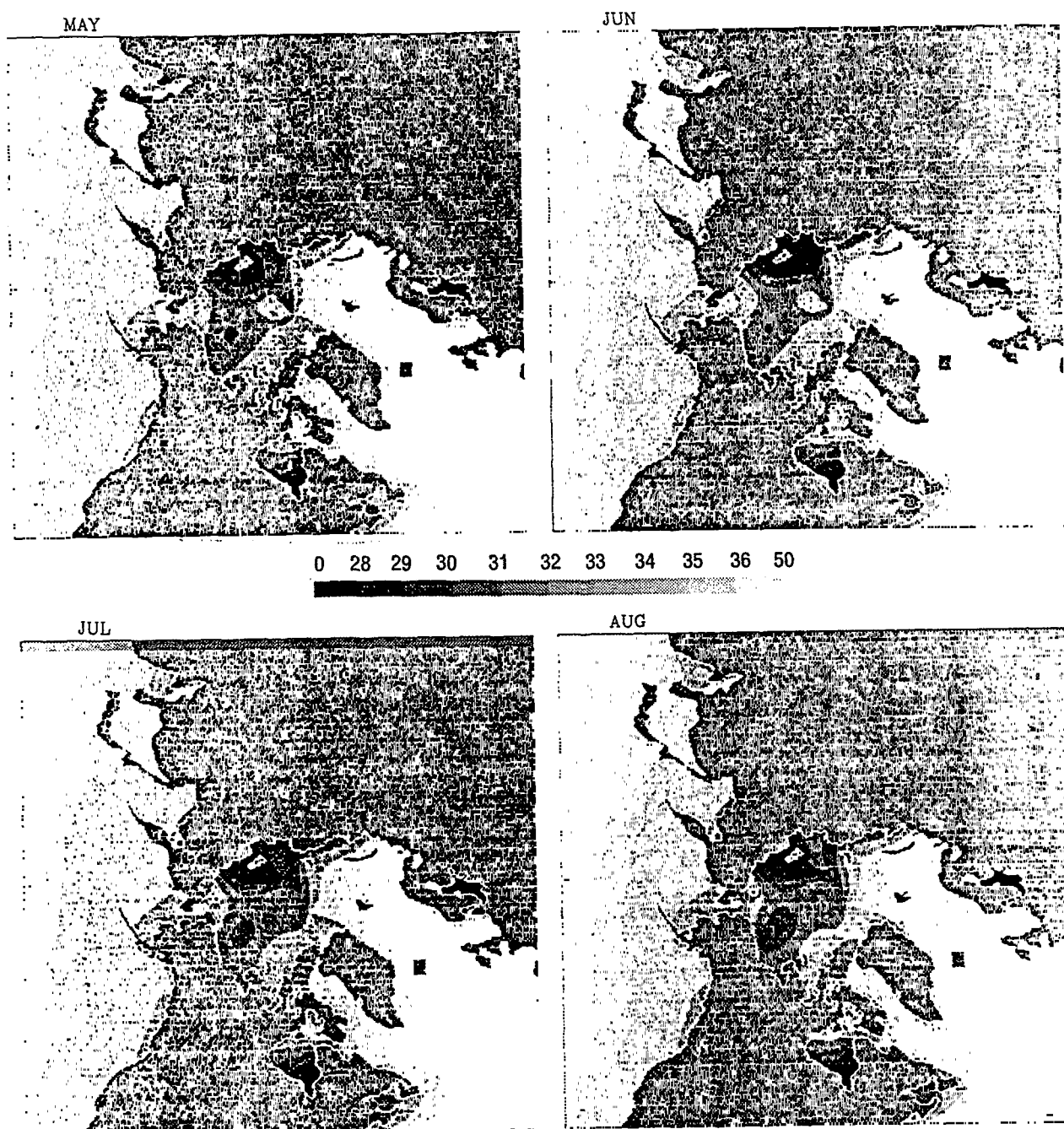
Fig. 10.2 — cont.

River	Runoff (km³yr⁻¹)
MacKenzie	340
Kolyma	102
Indigirka	57
Lena	520
Kotuy	105
Yenisei	603
Ob	530
Pechora	130

Table 11.1 — Major River Runoff in the Arctic [Aagaard and Carmack 1989]

Skakalsky [1993], the annual runoff from each river was interpolated into monthly data to be consistent with the other data fields (the NOGAPS winds and the Levitus climatology) that were used for studies. Flood or drought seasons would change the monthly river flow, which in turn would change both ice and ocean conditions near river mouths.

12.0 COUPLING THE ICE AND OCEAN MODELS

The discussion to this point has left the interface between the Cox ocean model and the ice growth model undefined. In the earlier versions of the PIPS model [Preller 1985], the ice model essentially ran independently of the ocean model. The oceanic forcing necessary for the former model was provided by Hibler and Bryan [1987]. Changes in salinity, the daily exchanges of heat between ice and ocean, and the drag that the ice exerts on the currents directly under it were totally unaccounted for in earlier work. The ice-ocean coupled model described here has sought to improve that situation by using an algorithm that simultaneously integrates both the ocean model and the ice model, while exchanging information along the way. That algorithm is described in this section.

The intent of the algorithm is to preserve the autonomy of both the ice model and the Cox ocean model, and couple the models by exchanging necessary information. The top mixed-layer temperatures, the variable freezing temperatures, the oceanic heat fluxes, and the ocean currents are provided from the ocean model to the ice model. In return, a variable drag coefficient, salinity transfers, and daily ice growth rates are provided to the ocean model. These interchanges are made on each day of model time. The details of these transfers follow.

The two important equations in the ocean model into which the daily information from the ice model is updated are the equations for water temperature and salinity. Following Cheng and Preller [1992; 1994], Hibler and Bryan [1987], Cox [1984], and Sarmiento and Bryan [1982], the heat equation for computing water temperature is written as follows:

$$\frac{\partial T}{\partial t} + \nabla \cdot (\mathbf{u}T) = K_H \nabla_H^2 T + K_z \frac{\partial^2 T}{\partial z^2} - \frac{f_A \delta(z) R_0 \theta (T - T_f)}{Z_{mix}} - R_t (T - T_0) , \tag{4}$$

where T is the water temperature,

   $\mathbf{u}$ is the ocean current,

   K_H is the coefficient of the horizontal eddy diffusion,

∇^2_H is the horizontal Laplacian operator,

K_z is the coefficient of the vertical eddy diffusion,

f_A is the ice growth/melting rate in open water due to atmospheric forcing only,

A is the ice concentration,

$\delta(z)$ is the delta function (i.e., one in the mixed-layer and zero otherwise),

R_0 is a ratio of the latent heat of fusion of sea ice to the heat capacity of seawater,

$\theta(T - T_f)$ is 1 when the mixed-layer temperature T is greater than the freezing point T_f, and zero otherwise,

R_t^{-1} is the robust constraint for water temperature and salinity, and is 250 days for all levels in the ice-ocean coupled model,

T_0 is the Levitus monthly climatological temperature, and

Z_{mix} is the mixed-layer thickness.

The robust constraint, R_t^{-1}, was used in the integration of the equation, not only to keep ocean temperature and salinity from dissipating due to eddy diffusion and lack of precipitation, but also to allow atmospheric heating/cooling to penetrate into the mixed layer in open water areas. This constraint differs from those used in the Cox ocean model (Sec. 8.0), which were imposed to accelerate the model spin-up from a motionless ocean, as well as to relax the temperature and salinity towards the Levitus climatological data. The sign convention used here is that positive ice growth rate due to atmospheric forcing f_A means that the water is cooling off; negative f_A implies the water is warming.

The salinity equation in the ocean model is:

$$\frac{\partial S}{\partial t} + \nabla \cdot (\mathbf{u}S) = K_H \nabla^2_H S + K_z \frac{\partial^2 S}{\partial z^2} + \frac{0.035 S_f \, \delta(z)}{Z_{mix}} - R_t(S - S_0), \tag{5}$$

where S is the salinity,

S_f is the total ice growth rate in open water, and

S_0 is the Levitus monthly climatology salinity.

A robust constraint is also used here for the same purpose as with the temperature equation. Salinity in the mixed layer could vary seasonally according to ice growth or melt because sea ice rejects salt as it forms. An average salinity value of 35 ppt is used for fresh water when melting occurs and for brine when ice is growing.

For numerical stability of the ocean model when it is coupled with the ice model, a 0.5-hr timestep is used for integrating the temperature and salinity equations, and a 0.05-hr timestep is used for the stream function and ocean current. For the ice model, a 2-hr timestep was chosen.

The freezing temperature (°C) depends on the mixed-layer salinity, as follows:

$T_f = -54.4 \ S$, where S is the salinity.

The mixed-layer oceanic heat fluxes are defined as the heat advected and diffused into each grid cell and have the following forms: $-\nabla \cdot (\mathbf{u}T), K_H \nabla_H^2 T, \text{and } K_z \dfrac{\partial^2 T}{\partial z^2}$, each multiplied by the water mass and its heat capacity. Vertical mixing and vertical heat convection in the Cox ocean model takes place whenever density differences occur that must be smoothed out. In this coupled ice-ocean model, mixed-layer currents that are driven by geostrophic winds are used instead of the second-layer ocean currents [Hibler and Bryan 1987; Semtner 1987].

In this study, a variable drag coefficient between sea ice and water was applied according to the boundary layer theory of McPhee [1990]:

$$C_{d,ice\text{-}water} = \left(\frac{1}{k} ln \left(\frac{h}{z_0} \right) \right)^{-2},$$

where $C_{d,ice\text{-}water}$ is the coefficient,

k is the von Karmon constant, 0.41,

z_0 is the ice roughness and is set to be 0.01 m, and

h is the ice thickness and is set to be greater than z_0 at all times.

When h is equal to 2.5 m, the drag coefficient is equal to the constant value (0.0055) used by the initial versions of PIPS. Note that the drag coefficient decreases as the ice thickness increases; i.e., there is very little drag stress on thick ice from water. However, the drag stress becomes the dominant factor over wind stress when h is small and is very close to z_0.

Hibler and Bryan [1987] used the ice internal stress and the surface wind stress in the momentum balance equation of the ocean model. In coupling the PIPS2.0 ice and ocean models, the sea ice is treated as a boundary layer that blocks direct heat and momentum exchanges between the atmosphere and the ocean. Surface wind stress passes momentum to the sea ice; some momentum moves the sea ice, and some transfers into the internal ice. Sea-ice motion that drags the top mixed layer at the surface is modeled in PIPS2.0.

In the coupled model, the mixed-layer temperature depends on the open-water condition. If the open water starts to grow sea ice, then the mixed-layer temperature is set at the freezing point. The open water does not grow sea ice if the atmospheric and oceanic forcings are not cold enough. They simply reduce the mixed-layer temperature. In the melting seasons, the forcings warm the mixed layer or melt the existing sea ice.

Since the Hibler and PIPS ice models do not couple with ocean models, the mixed-layer temperature depends on accumulated heat during melting seasons, called YNEG in the model Fortran code. In modeling, the heat is stored and accumulated. It has to be balanced completely in fall and winter before growing any sea ice. In the coupled model, the oceanic heat fluxes were computed based on the heat advection and diffusion (Eq. 4). In the ocean model, the mixed-layer

temperature is heated or cooled according to the atmospheric forcing, i.e., $\dfrac{f_A \delta(z) R_0 \theta\,(T - T_f)}{Z_{mix}}$. Therefore, it is reasonable to eliminate the YNEG term in the coupled model.

Figures 12.1–12.6 show the ice-ocean coupled model in action. The monthly Levitus data and the monthly NOGAPS wind forcing data were used to drive the ice-ocean coupled model for 5 yr. The model continued to run for another 2 yr with the monthly river runoff included. Figures 12.1 and 12.2 show the model distributions of ice thickness and concentration for each month of a year. The model ice-drift velocities for the same year are plotted in Fig. 12.3. Figures 12.4 and 12.5 are the model distributions of ocean temperature and salinity, and Fig. 12.6 is the ocean current at a 15-m depth.

For comparison, the dark thick line in the March ice concentration of Fig. 12.2 indicates ice-edge locations near mid-month that were derived as the weekly ice concentration analysis by the Navy-NOAA (National Oceanic and Atmospheric Administration) Joint Ice Center (JIC). The JIC weekly analysis is derived from satellite passive microwave measurements, visible and infrared imagery, aerial reconnaissance and conventional field observations. The visual agreement between the data and the model results is good.

13.0 RESULTS OF AN ICE-OCEAN COUPLED MODEL

Section 13.1 shows the ocean model results of the PIPS2.0 ice-coupled model and discusses how the parameters of viscosity and diffusivity, the lateral wall boundaries, and the forcing fields influence ocean circulation. After that, for further regional discussion, the PIPS2.0 model domain was divided into seven regions in the area of interest as follows: the Central Arctic (Sec. 13.2), the Barents Sea (Sec. 13.3), the Norwegian/East Greenland Seas (Sec. 13.4), Baffin Bay/Labrador Sea (Sec. 13.5), Hudson Bay (Sec. 13.6), the Bering Sea (Sec. 13.7), and the Sea of Okhotsk (Sec. 13.8). Since each of these regions has the potential of becoming a separate topic of interest in future international affairs, each is discussed separately, and the best available model description is given.

13.1 The Ocean Model Results

In the Arctic and sub-Arctic regions, all the major circulations appear in the output of the ice-ocean coupled model: the Alaska Gyre, the Oyashio Current, the Beaufort Gyre, the Transpolar Drift, the East Greenland Current, the Norwegian Current and its branches to the Barents Sea and south and west of Spitsbergen, the North Atlantic Drift and its return current, and the Labrador Current. In general, the stream function follows the f/H contours throughout the domain, as Semtner [1987] suggested, where f is the Coriolis parameter and H is the ocean-bottom topography (see Figs. 13.1.1 and 9.1). Figure 13.1.1 shows the stream functions in March, June, September, and December. The features in the stream functions remain almost constant through the year, as expected, because the values represent the major ocean circulation. The seasonal variations represent the minor differences between the features.

The original values of the horizontal coefficients of eddy viscosity and diffusivity, which were used in the Cox ocean model, were appropriate when the model was run at 2°–3° spatial resolution. These coefficients were quite large, however, for the fine resolution (0.28575°) of the coupled model. Sensitivity studies to determine better coefficients for both ice and ocean models will be conducted and results presented in the future.
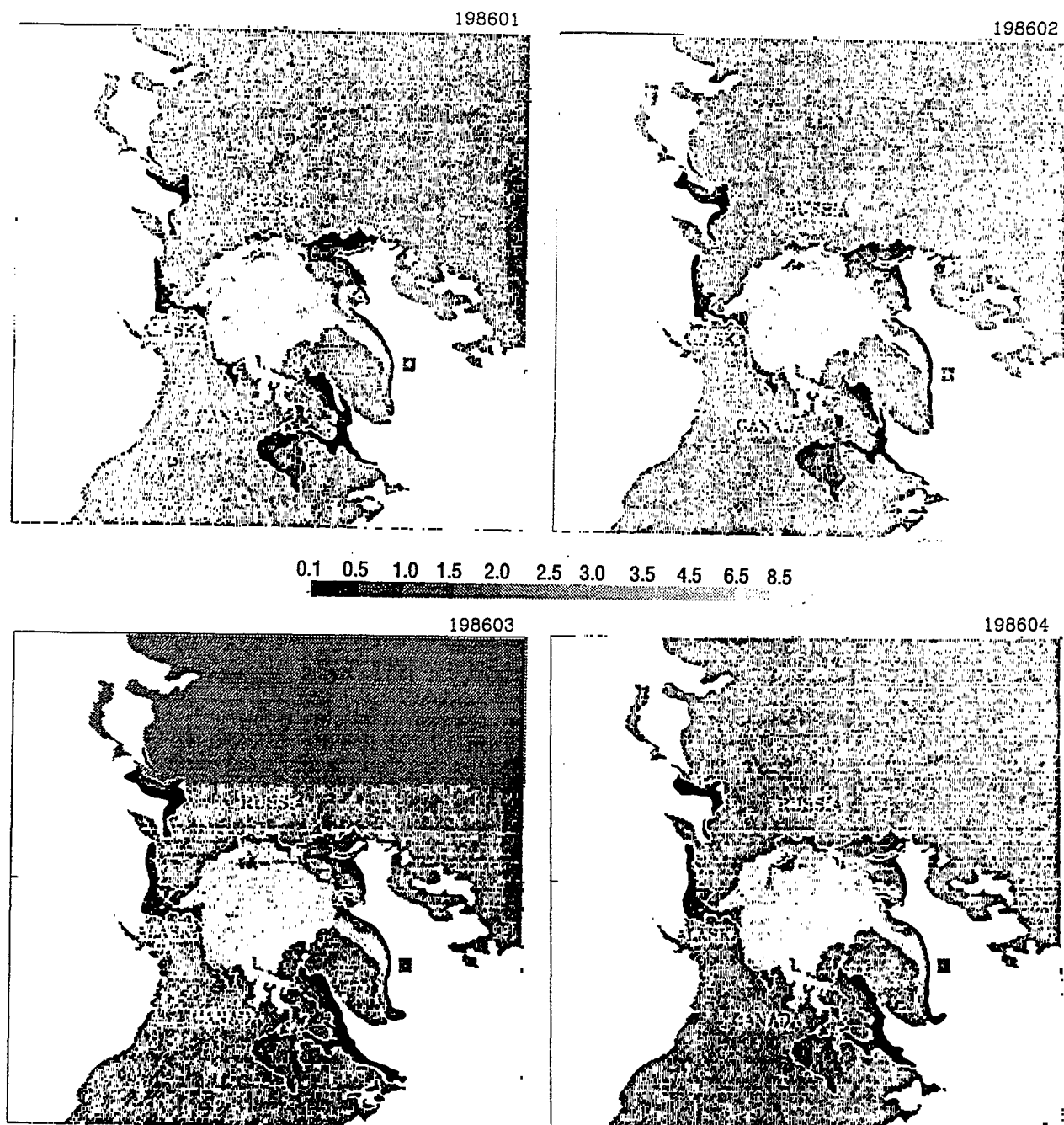
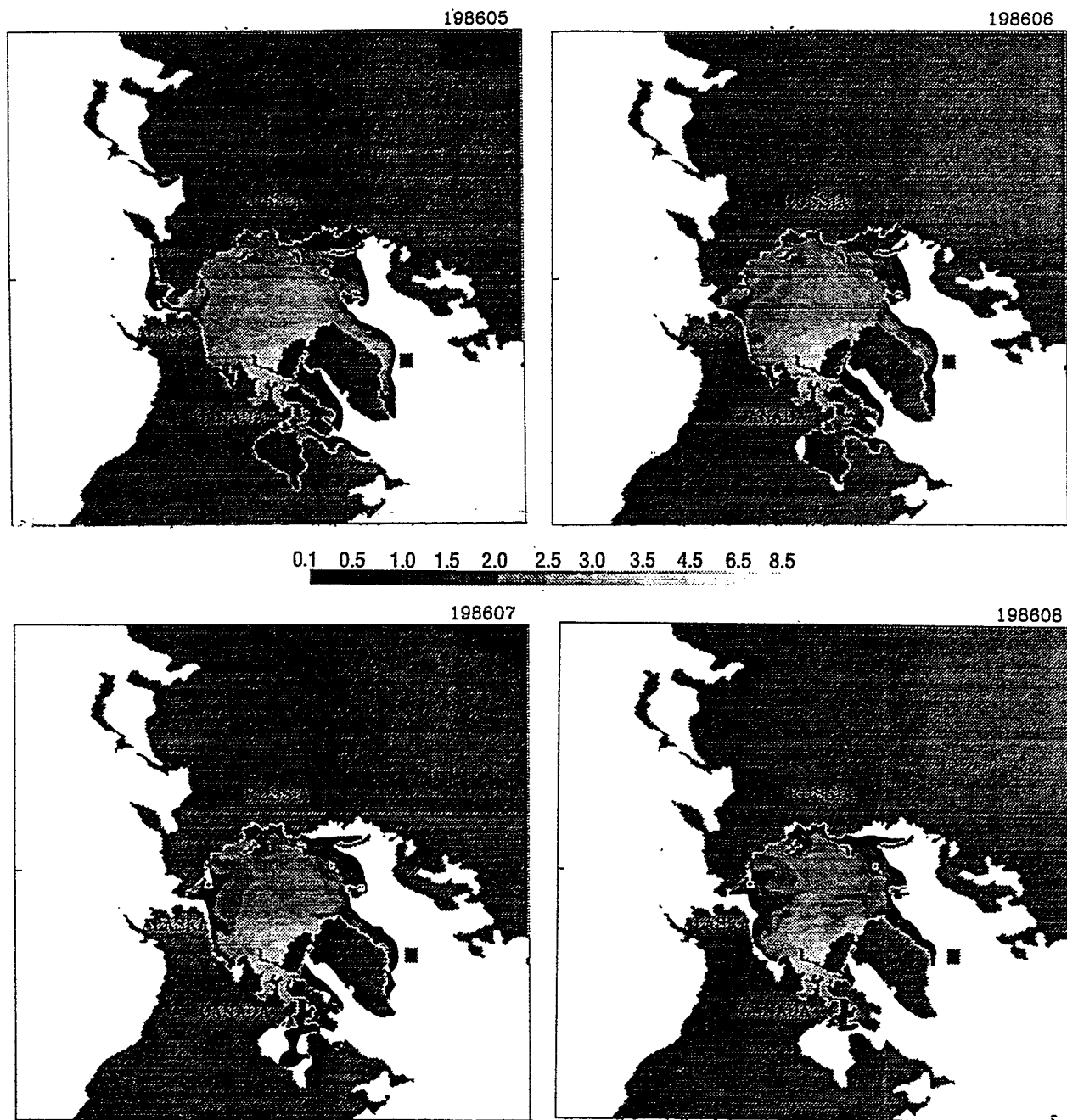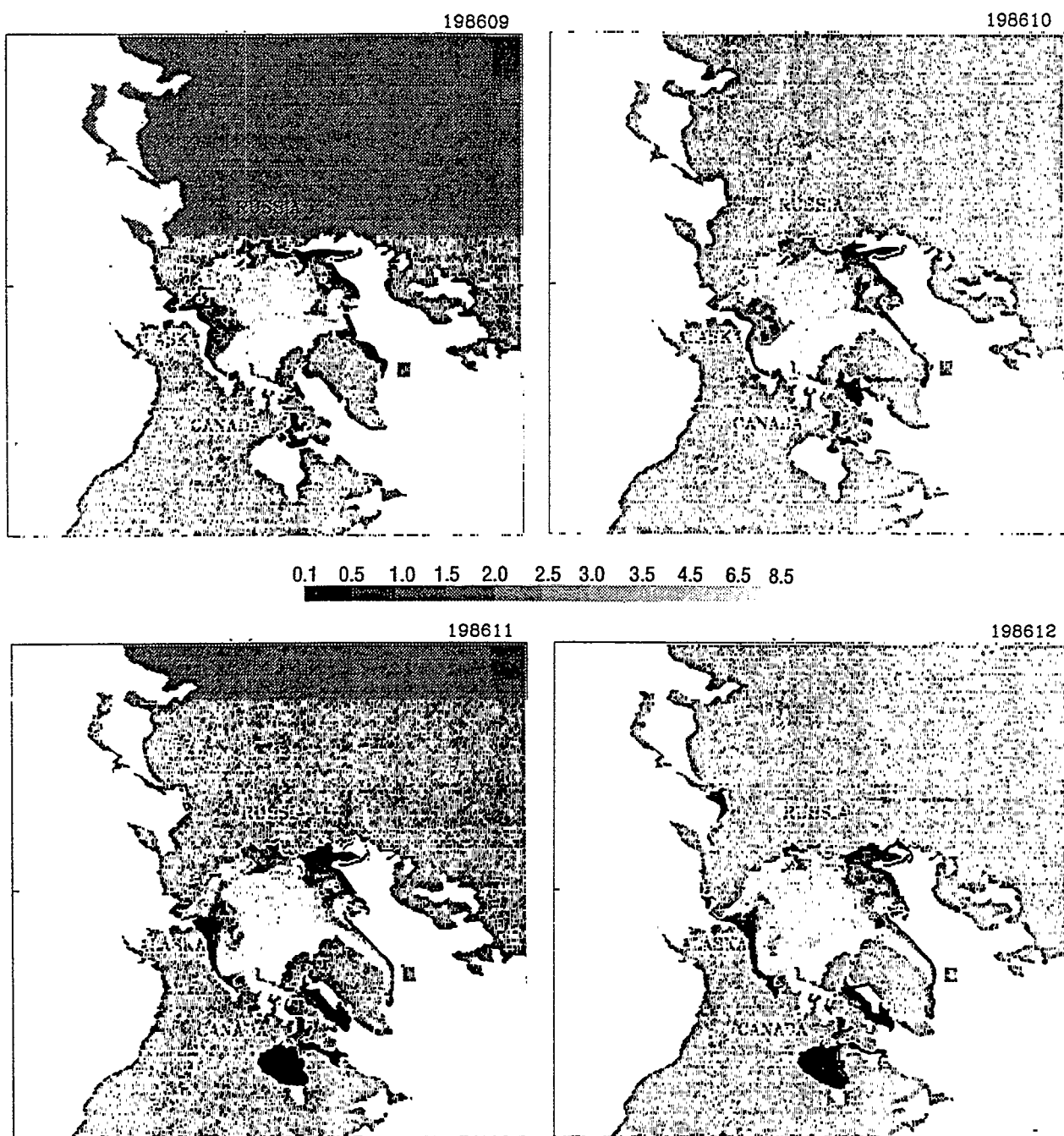Fig. 12.1 — Model ice thickness (m) distribution, Jan–Dec 1986

198605

198606

0.1   0.5   1.0   1.5   2.0   2.5   3.0   3.5   4.5   6.5   8.5

198607

198608

Fig. 12.1 — cont.

Fig. 12.1 — cont.
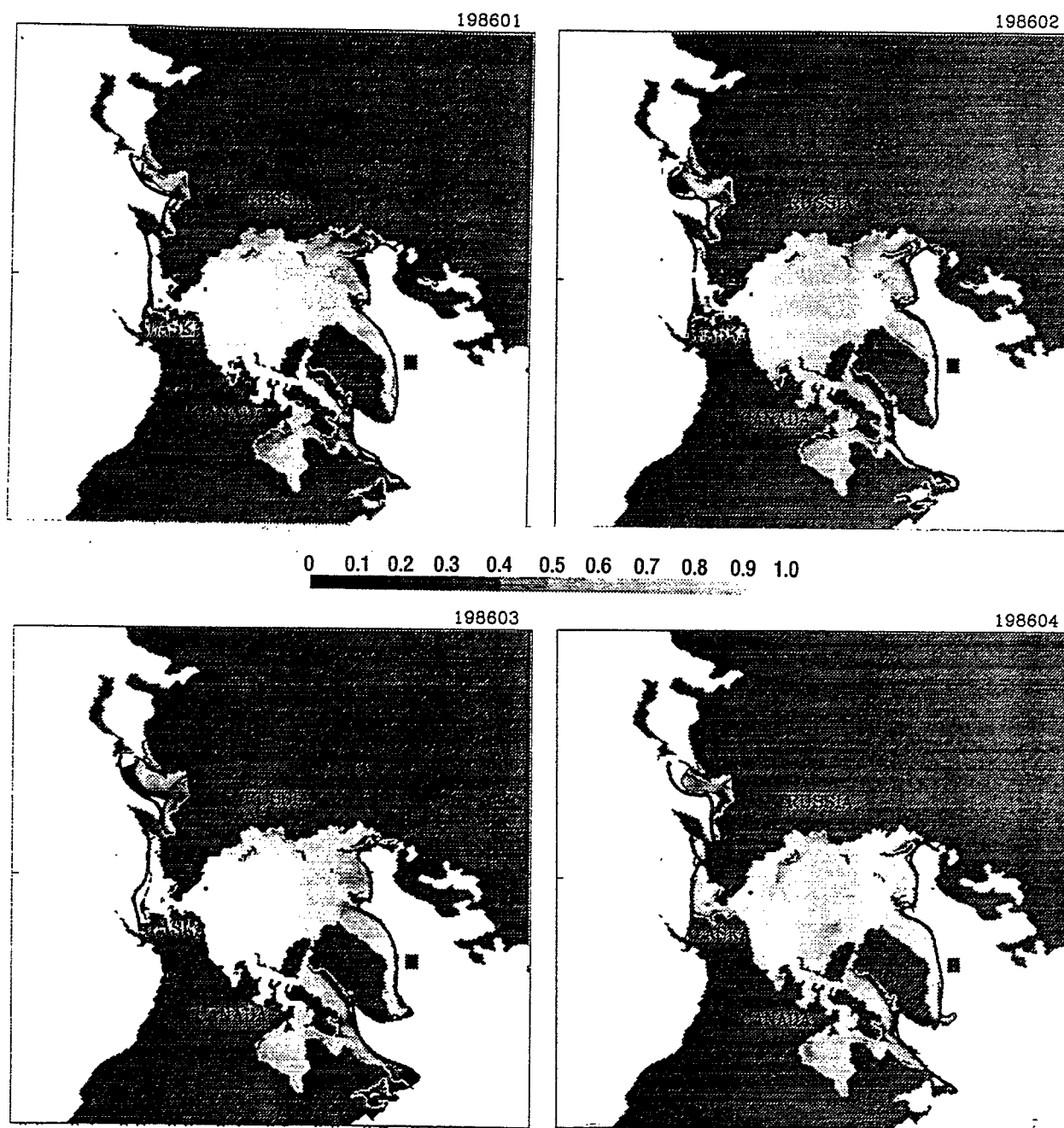
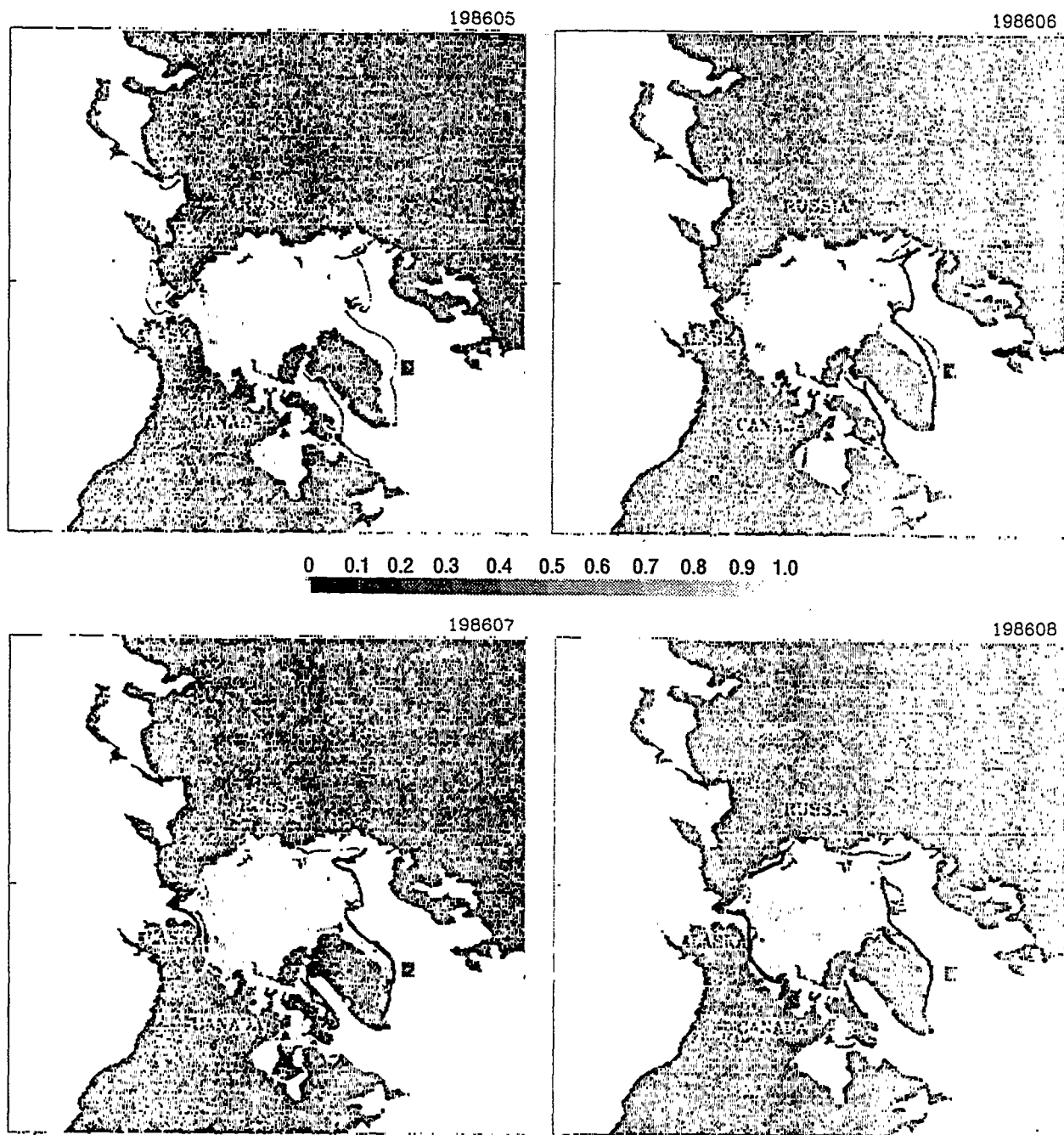Fig. 12.2 — Model ice concentration distribution, Jan–Dec 1986

198605

198606

0   0.1   0.2   0.3   0.4   0.5   0.6   0.7   0.8   0.9   1.0

198607

198608

Fig. 12.2 — cont.

198609

198610

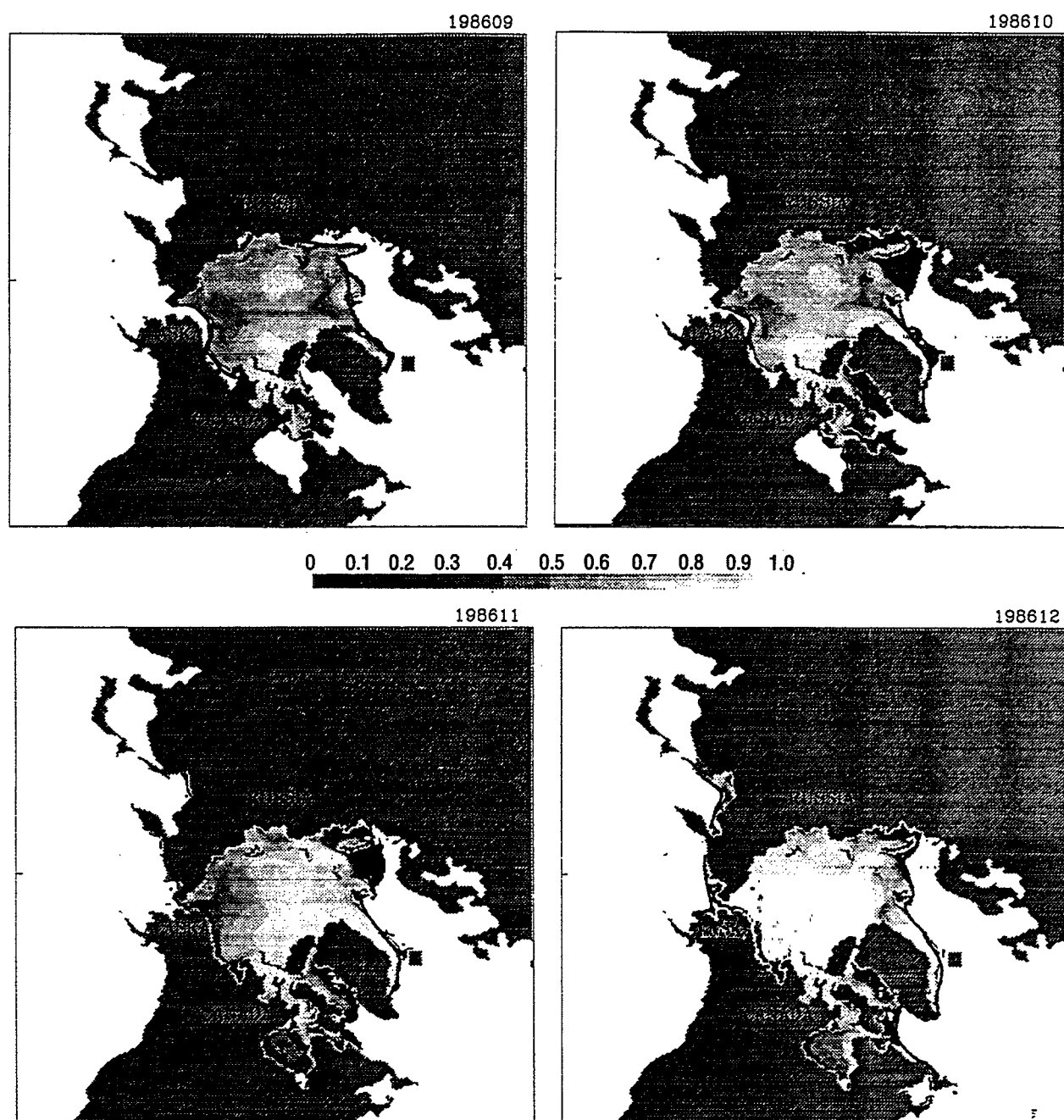0   0.1   0.2   0.3   0.4   0.5   0.6   0.7   0.8   0.9   1.0

198611

198612

Fig. 12.2 — cont.
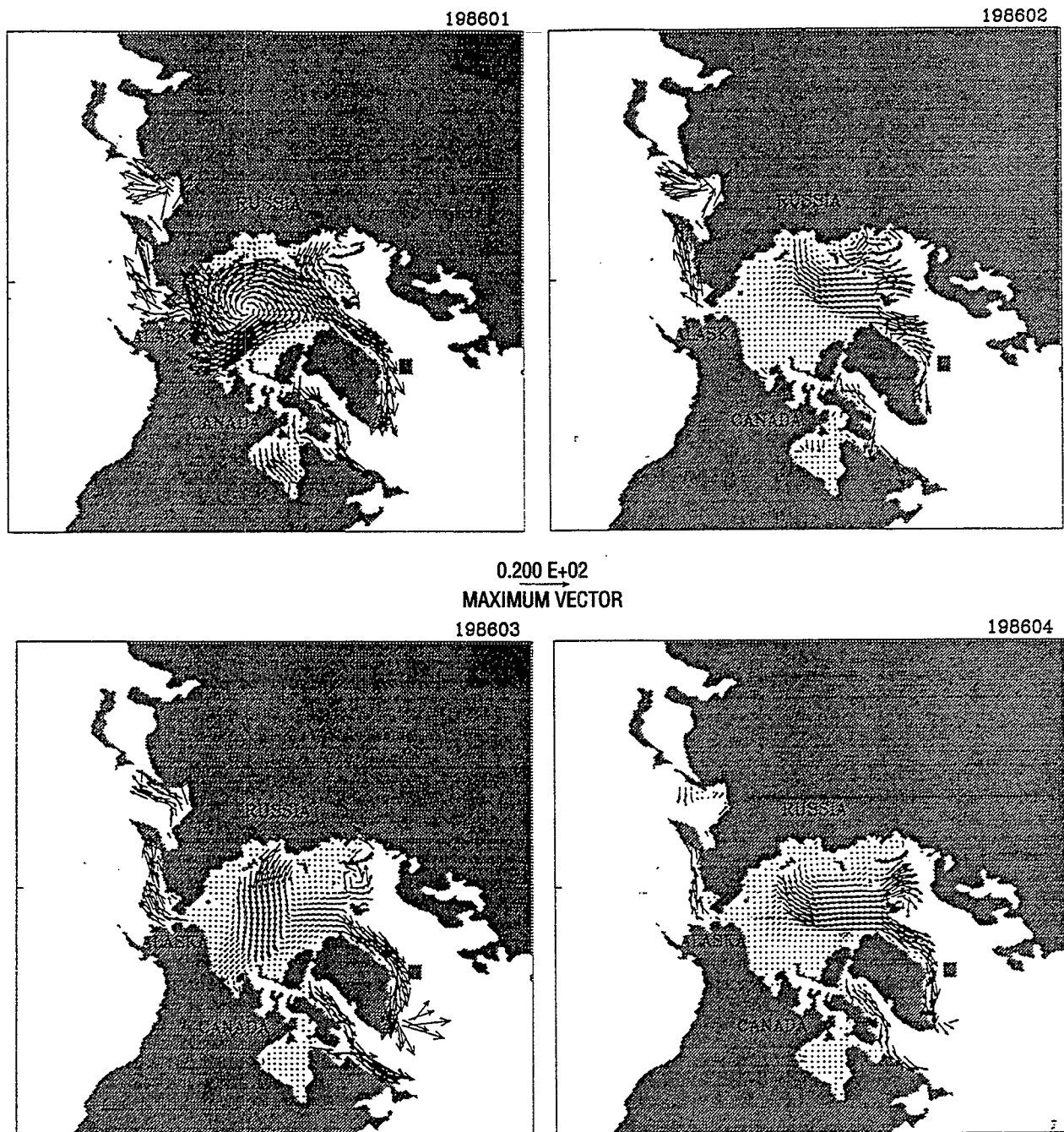
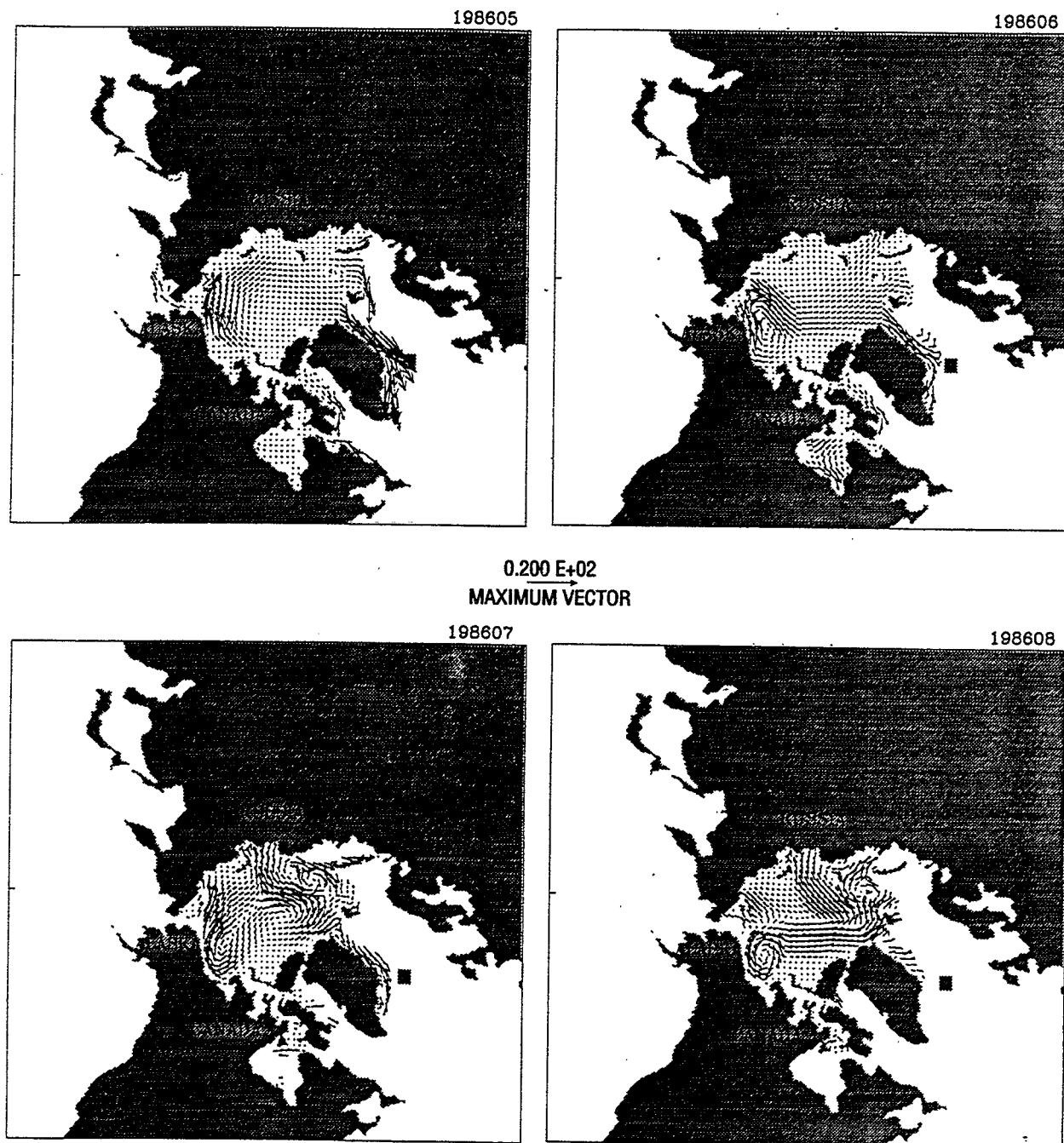Fig. 12.3 — Model ice drift velocity (cm/s), Jan–Dec 1986

198605

198606

0.200 E+02
MAXIMUM VECTOR

198607

198608

Fig. 12.3 — cont.
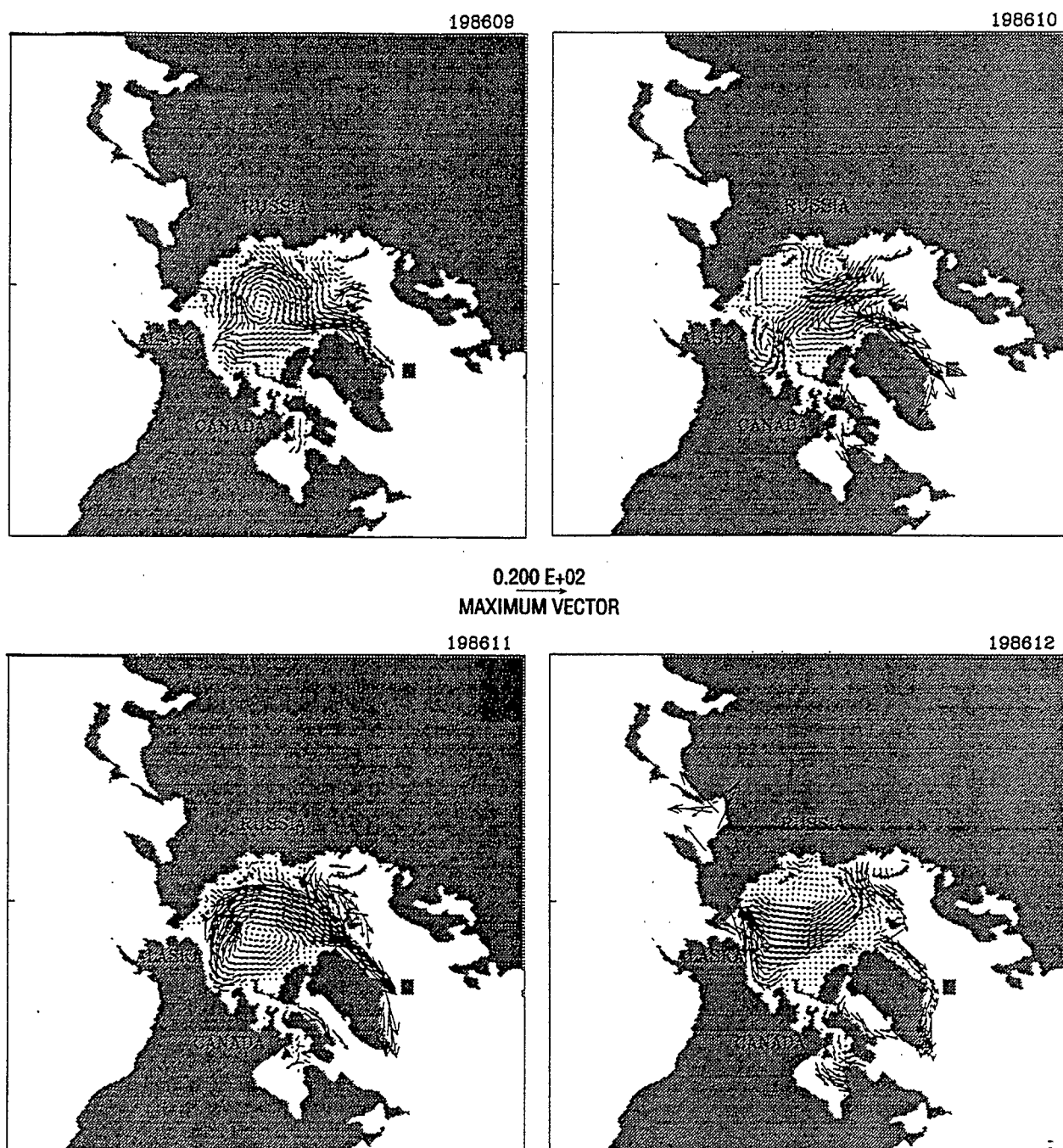
198609

198610

0.200 E+02
→
MAXIMUM VECTOR

198611

198612

Fig. 12.3 — cont.
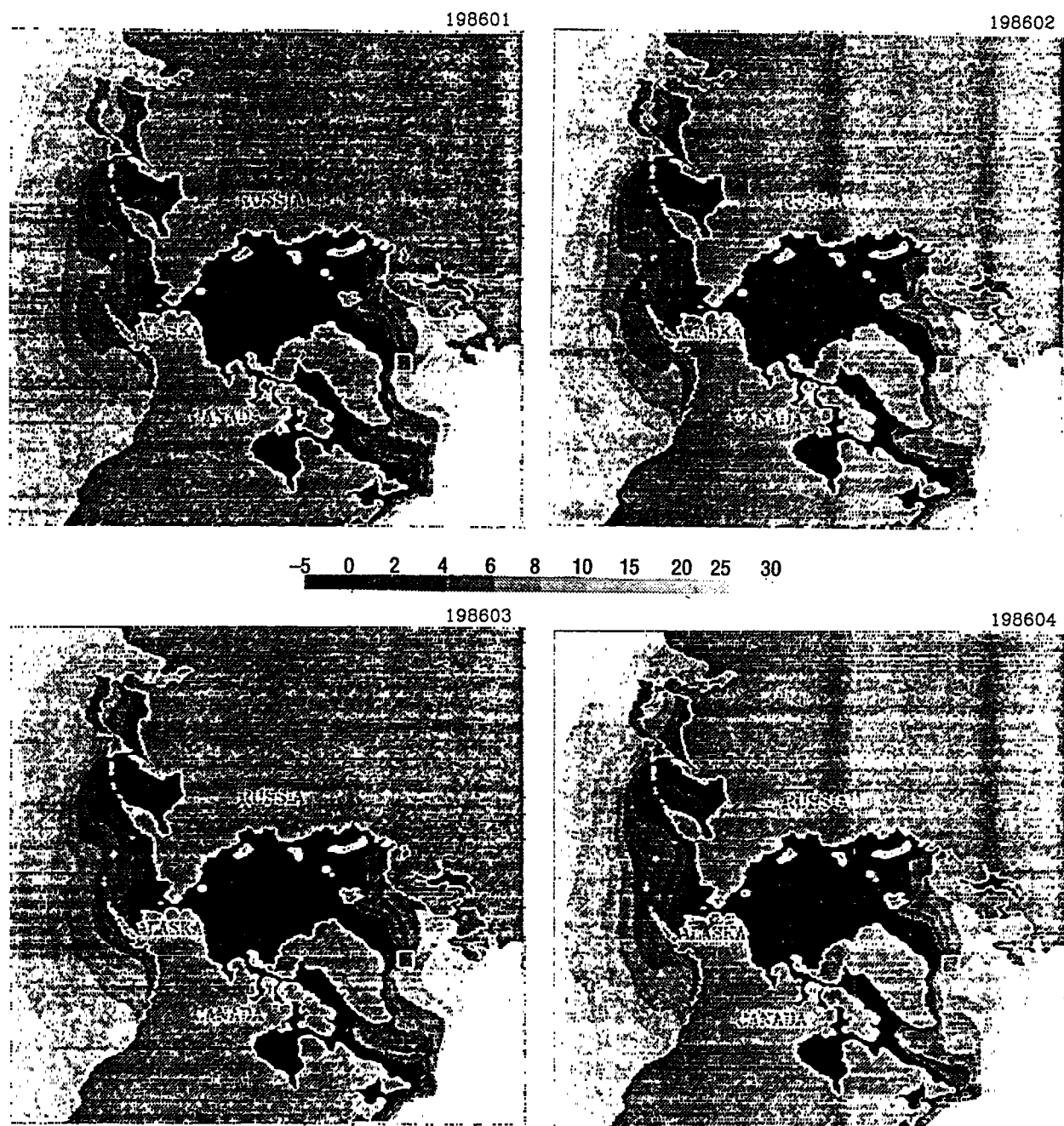
Fig. 12.4 — Model ocean temperature (°C) at 15 m, Jan–Dec 1986

Fig. 12.4 — cont.

198609

198610

-5   0   2   4   6   8   10   15   20   25   30

198611

198612
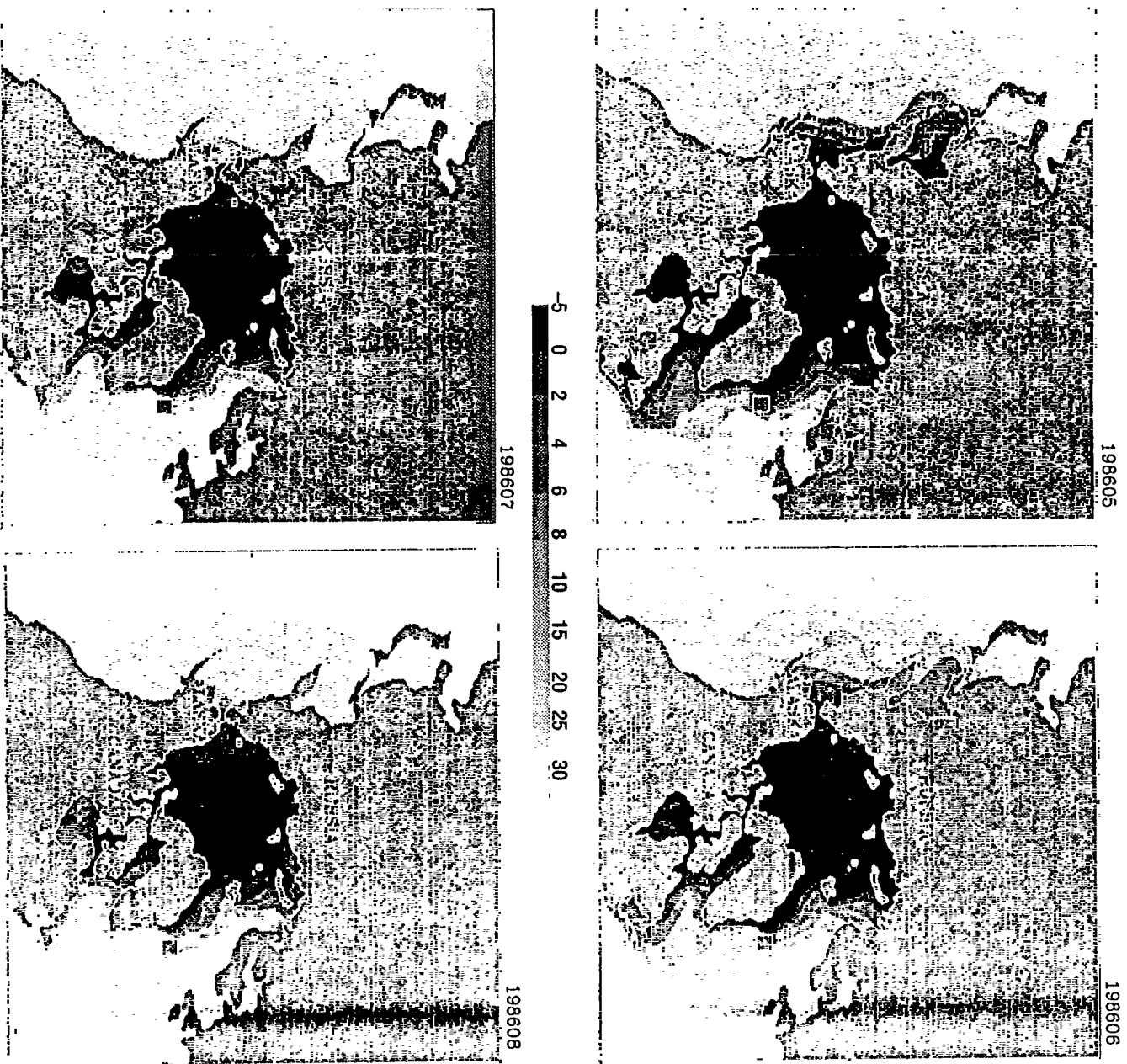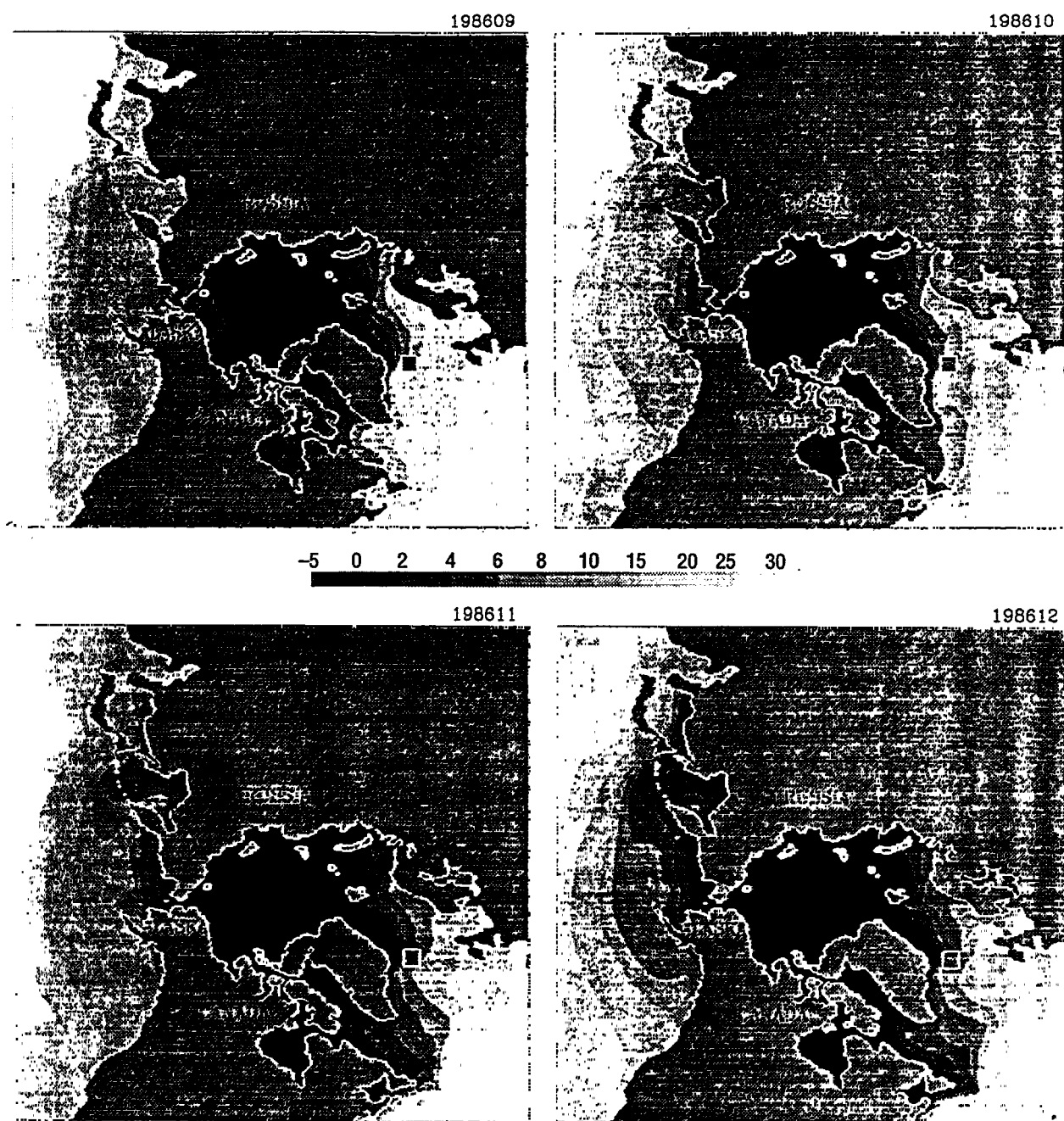
Fig. 12.4 — cont.
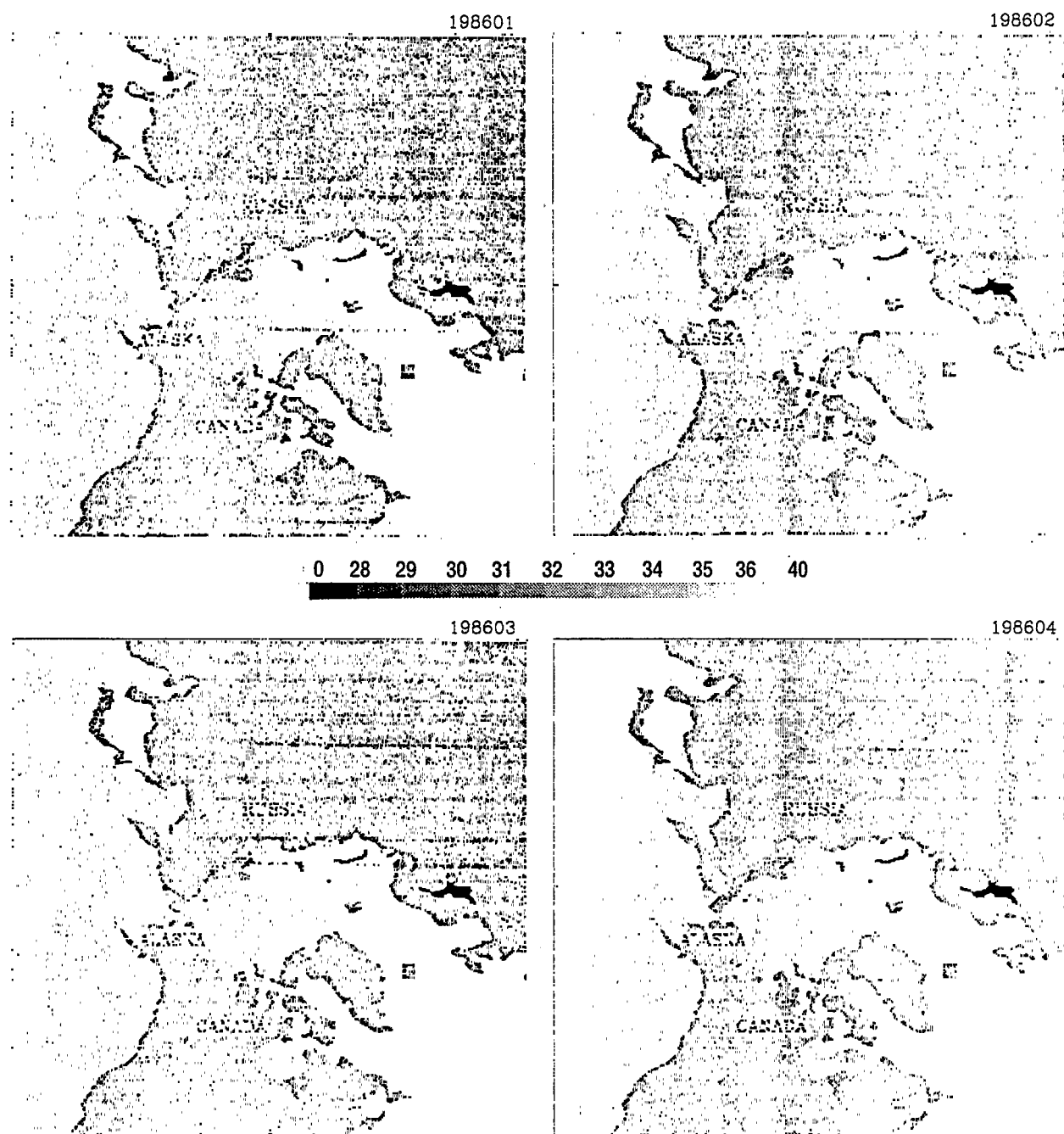
Fig. 12.5 — Model ocean salinity (ppt) at 15 m, Jan–Dec 1986

198605

198606

0 28 29 30 31 32 33 34 35 36 40

198607

198608
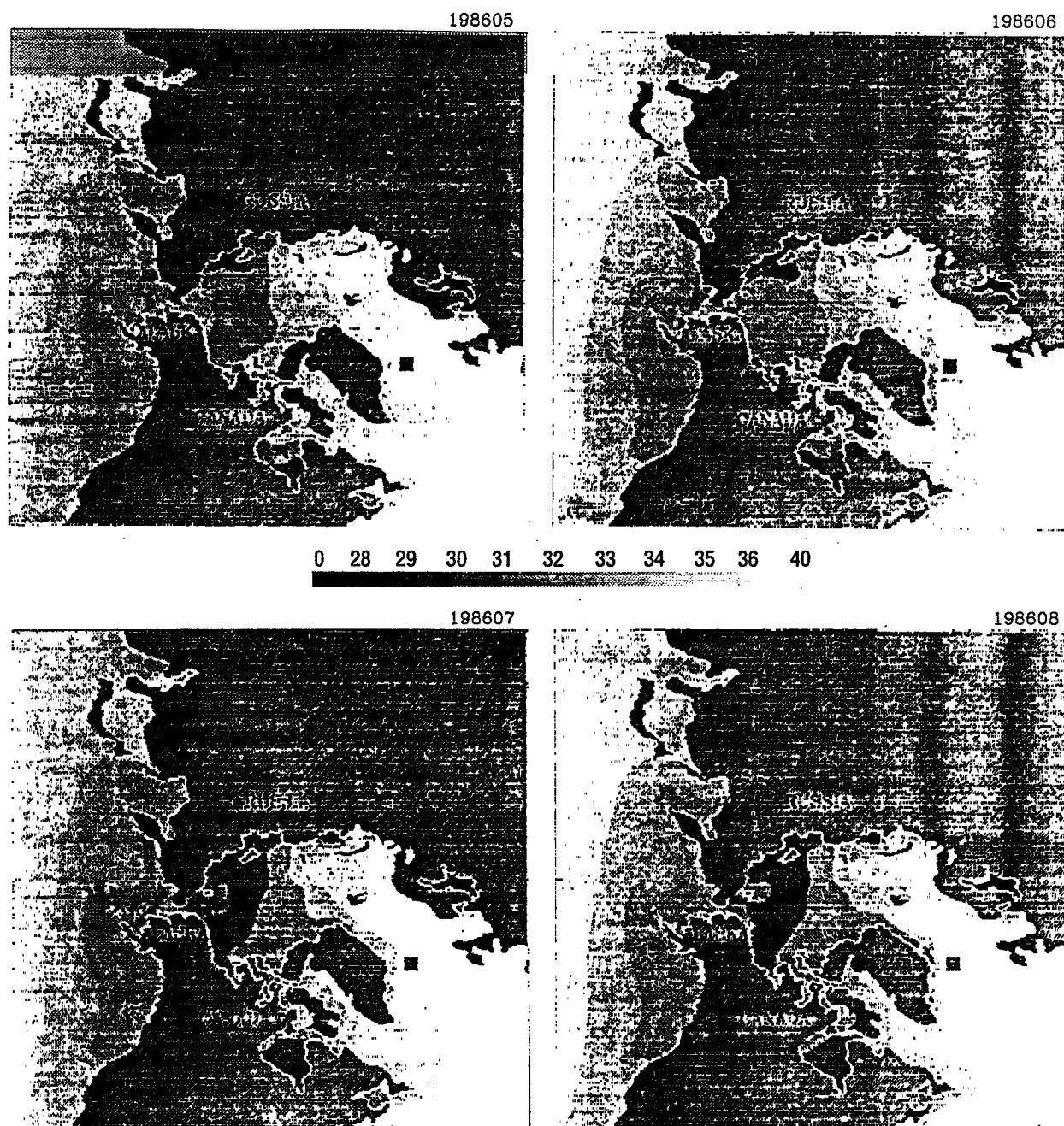
Fig. 12.5 — cont.

Fig. 12.5 — cont.

0.200 E+02
MAXIMUM VECTOR
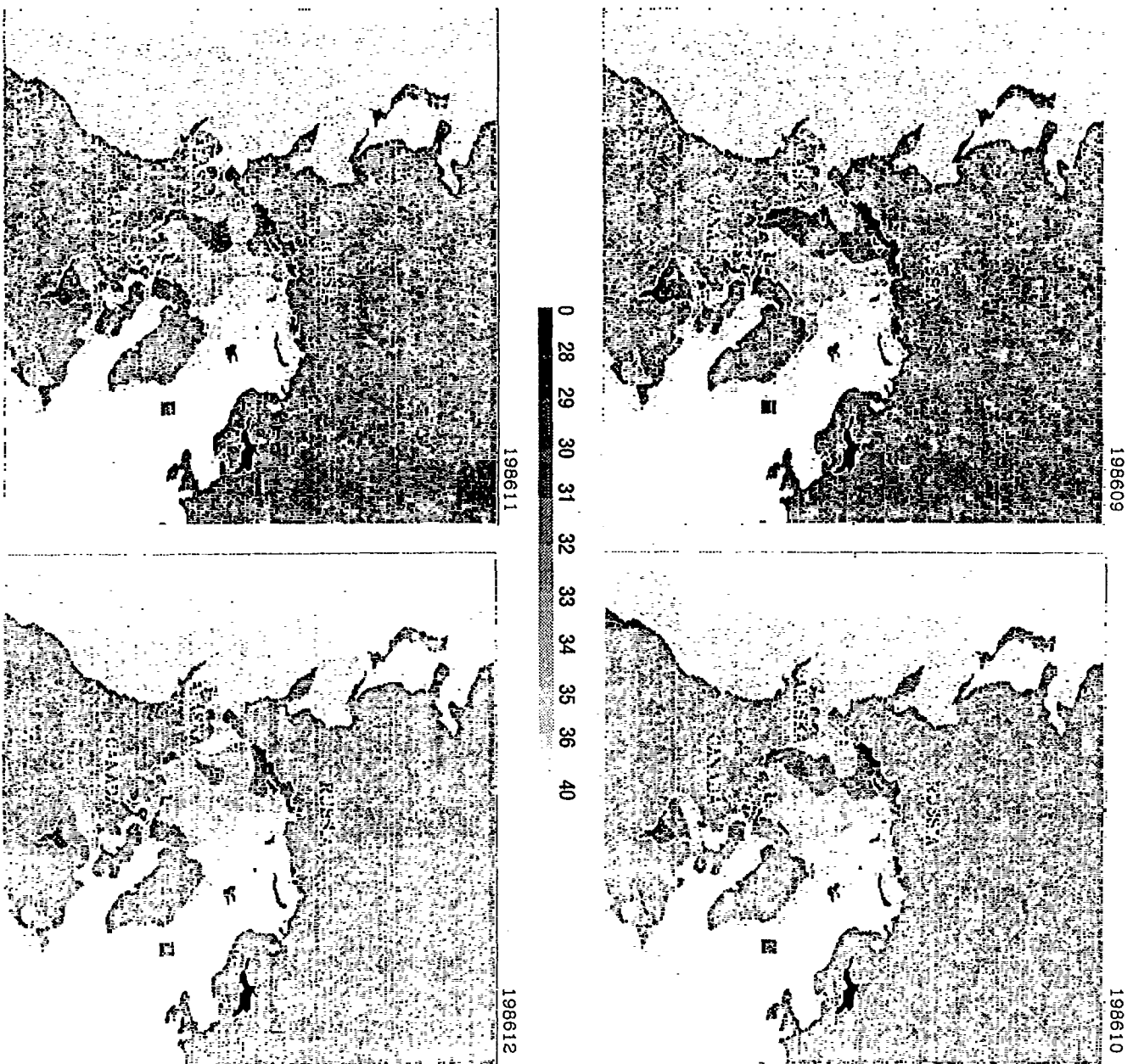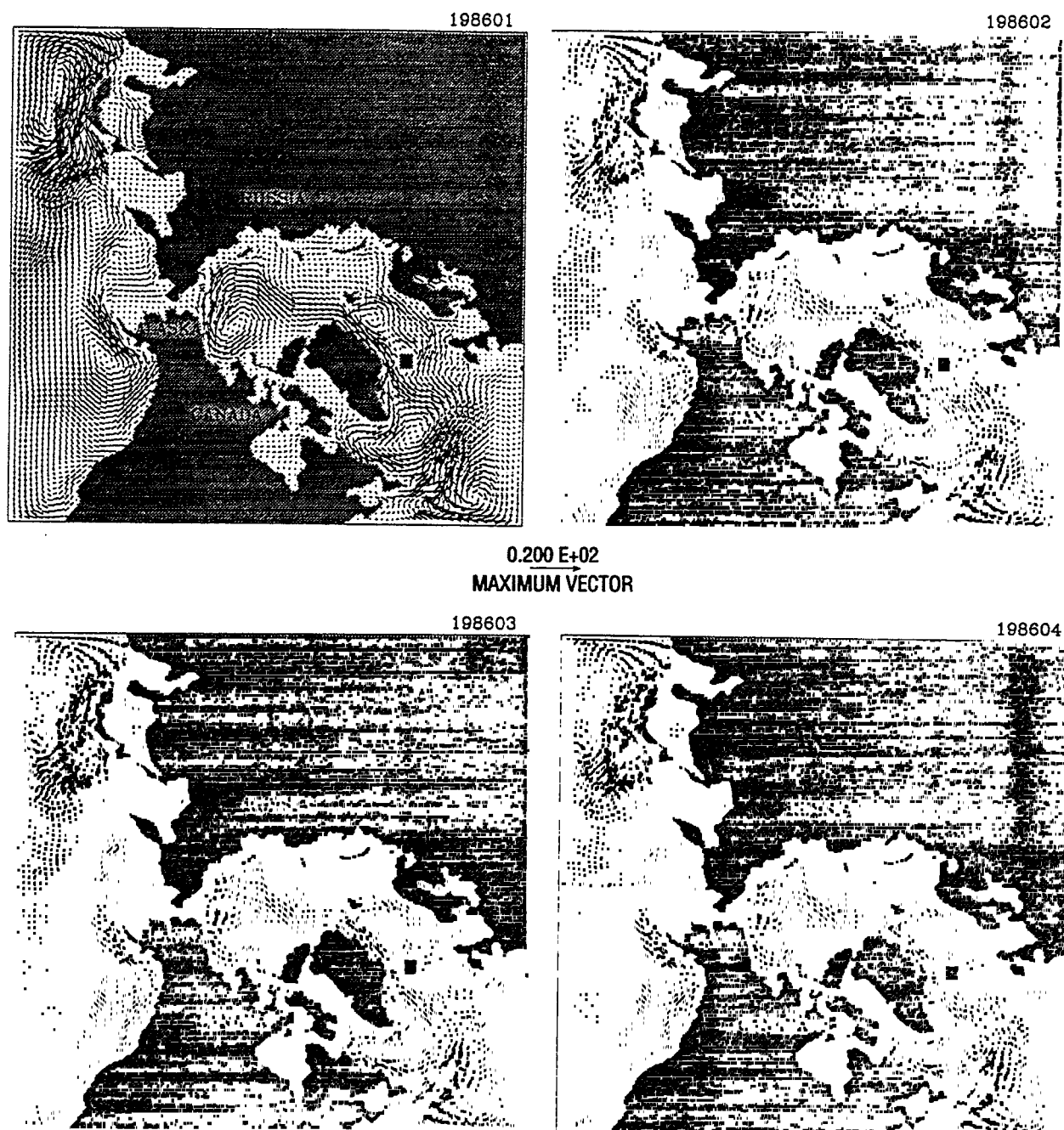
Fig. 12.6 — Model ocean currents (cm/s) at 15 m, Jan–Dec 1986

0.200 E+02
MAXIMUM VECTOR

Fig. 12.6 — cont.

198609

198610

0.200 E+02
MAXIMUM VECTOR

198611

198612

Fig. 12.6 — cont.

Fig. 13.1.1 — Model stream functions (cm^2/s) (a) Mar, (b) Jun, (c) Sep, and (d) Dec 1986

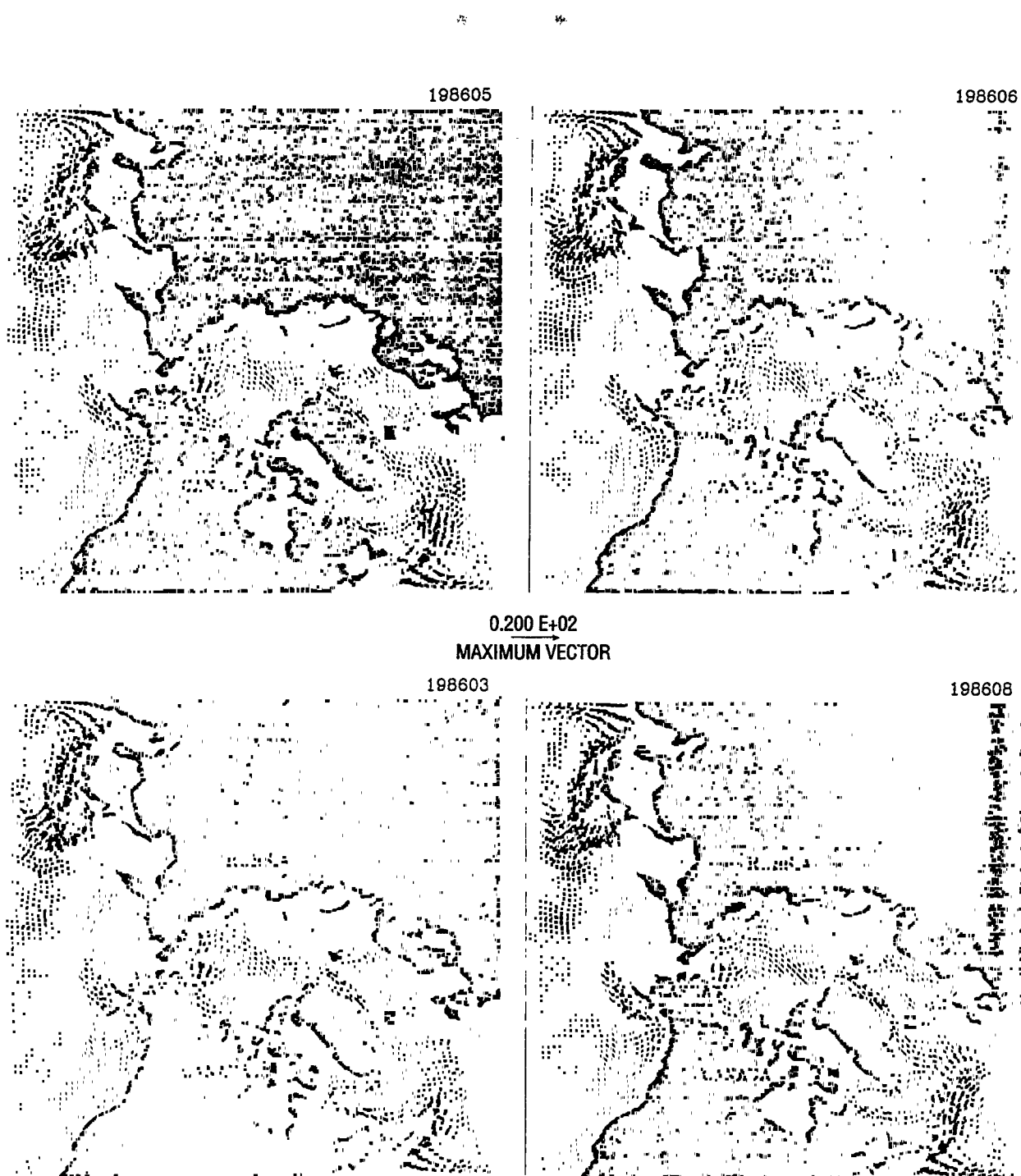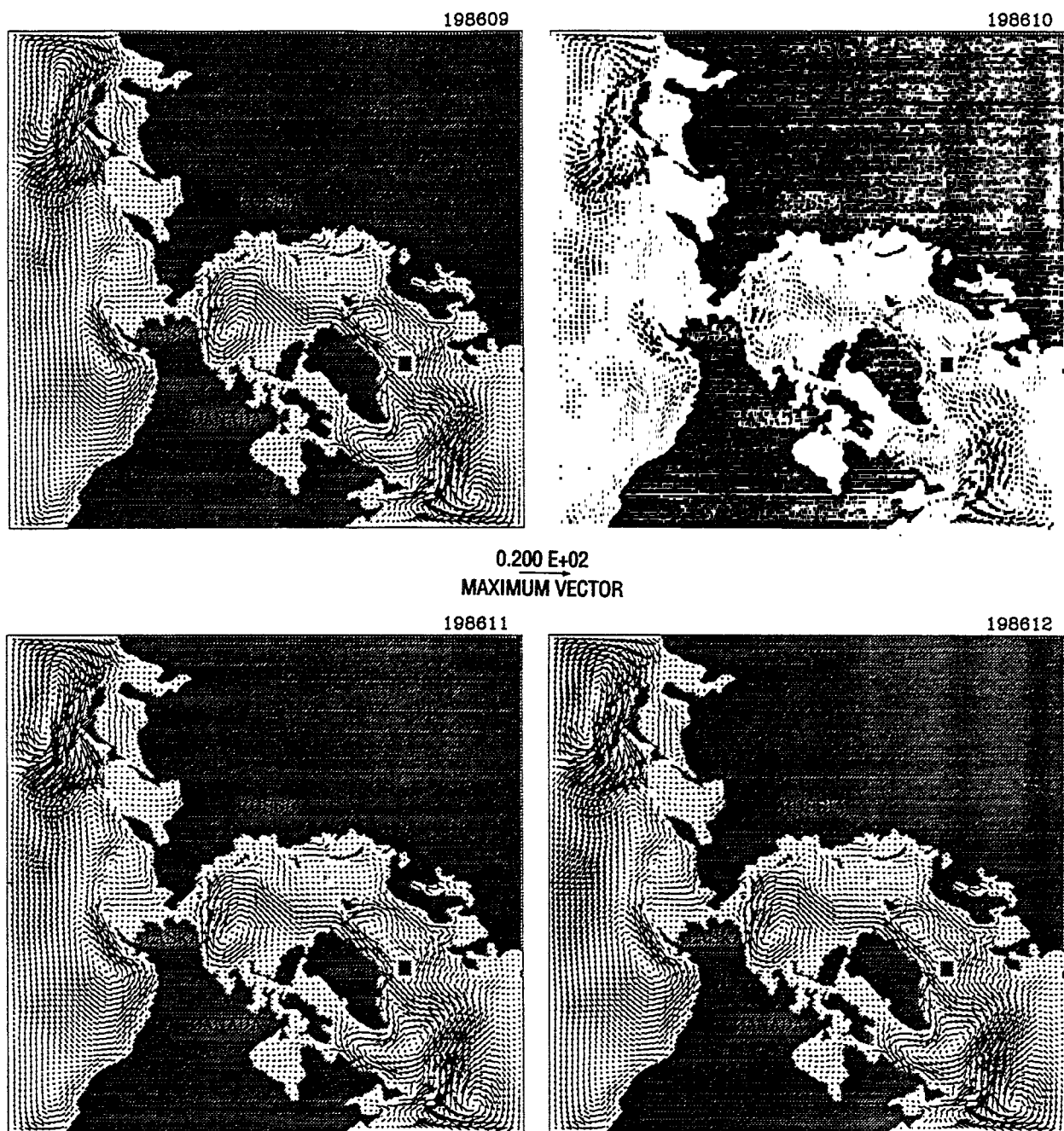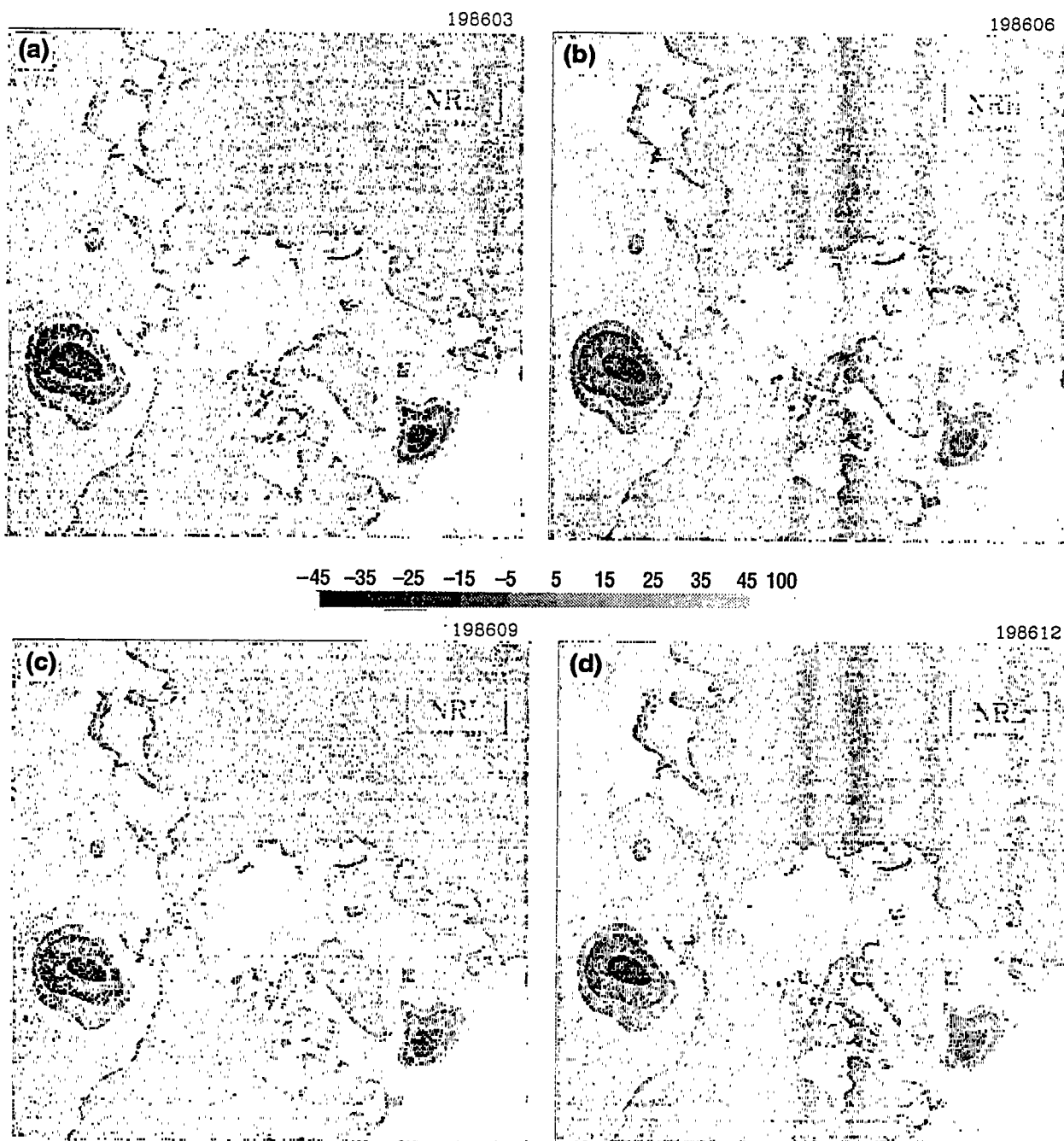Because of the way this model is implemented, inaccuracies are introduced into some of the calculations at lower latitudes. For example, inaccurate ocean currents on the lower right, upper left and lower left corners of Fig. 12.6 (i.e., near the Gulf Stream, the Kuroshio Current, and the California Current, respectively) are caused by (1) an assumption in the model that operates mainly in those lower latitudes, (2) the lateral solid wall boundary, and (3) the mass conservation law. The solid wall assumption blocks water exchanges between high- and low-latitude water masses. As a result, the model California Current moves northward, opposite to its observed motion. However, since the boundary at which the solid wall assumption is needed has been placed far away from sea ice-covered regions, the influence of the assumption on ice growth and drift should be negligible.

Another check on the current predictions of the PIPS2.0 model has recently become available, but again, that check is at low latitudes. According to Ebbesmeyer and Ingraham [1994], ocean current pathways tracked by following the trajectories of toys and shoes spilled in a maritime accident start from the middle of the North Pacific, move eastward to the coast of North America, and finally flow northward to Alaska. Another route starts at a low-latitude location (close to 135° W, 13° N), moves eastward along that latitude, then turns northeast toward Baja California (at (115° W, 15° N), and finally travels northward along the California coast to Alaska. Although this route is consistent with the PIPS2.0 model current pathways, that could be a special case driven by unusual winds or coastal Kelvin waves.

The current ocean model in PIPS2.0 cannot be used for resolving eddies. Because of the high horizontal eddy coefficients just mentioned and the model's horizontal grid resolution, seasonal variations of regional meanders and eddies, as well as those caused by ice melt and growth, cannot be resolved with the PIPS2.0 model. For example, the Chukchi Sea front between the Bering Sea warm inflow and the Arctic cold water cannot be delineated clearly by looking at Figs. 12.4, 12.5, and 12.6, even though the model temperature and salinity vary seasonally. The noneddy-resolving Cox ocean model is used to compute large-scale ocean circulations and the water transport between high and low latitudes.

The results of all these studies are very sensitive to variations in the wind fields. The model ocean currents, when driven by the monthly winds, change slowly during the year. When the NOGAPS daily (3- or 6-hourly) winds are used, however, the currents show strong daily variations, especially in the top mixed layer. For example, Fig. 13.1.2 shows such ocean currents and salinities for 21 and 31 October 1992, when the coupled model was driven by 6-hourly wind forcing fields. Wind-driven currents in open water are more energetic and variable than the monthly wind case, even when the salinity distributions are the same. More sensitivity studies of the wind stresses and the air drag coefficient will be conducted in the future.

Although the mixed-layer temperature starts with the Levitus climatology, a loose constraint is applied during the run integration. This constraint allows the atmospheric forcing to significantly change the temperature with season. For example, the Norwegian Sea reaches 8°C in March and 1°C in September. Similarly, the mixed-layer salinity also shows seasonal variations. In the East Siberian Sea and the Beaufort Sea, the model salinity is about 1–2 ppt higher than the Levitus data. Seasonal variations of ocean currents and temperature and salinity at depth are much smaller than those in the mixed layer.

Meunch [1989] classified the Arctic Ocean and the Norwegian and East Greenland Seas into four different categories of water: the Arctic surface layer (ASL), the Atlantic layer, the deep waters, and the Arctic shelf waters. The three main classes of ASL can be recognized as follows: the Atlantic Water (AW), which is the Norwegian-Atlantic Current with temperatures above 3°C and salinity above 34.9 ppt; the Polar Water (PW), which has been diluted by admixtures with fresh water, so its temperature and salinity are below 0°C and 34.4 ppt, respectively; and the Arctic
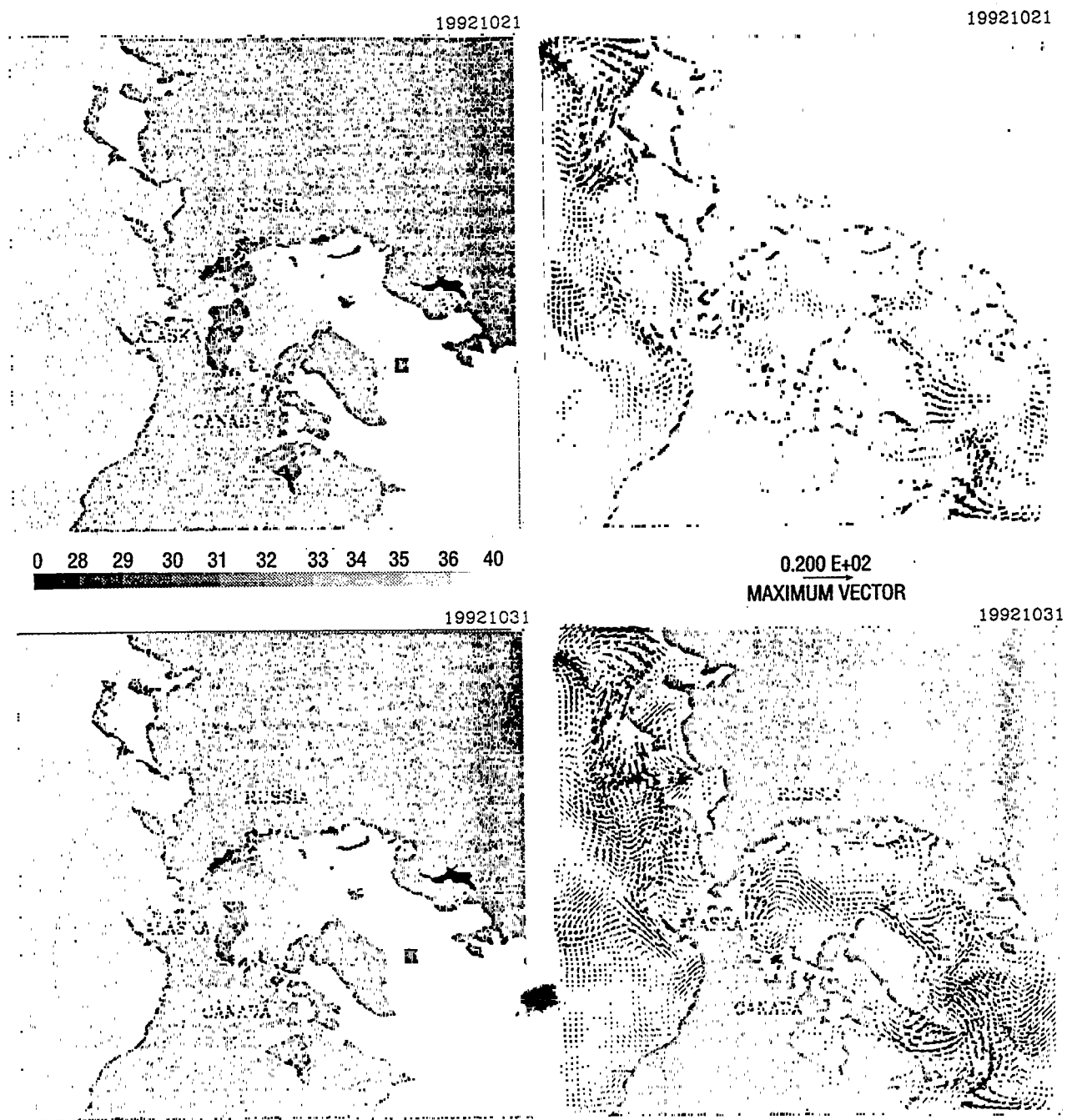
Fig. 13.1.2 — Model ocean temperature (°C) and current (cm/s) on 21 and 31 Oct 1992

Surface Water (ASW), which has temperatures between 0°– 3°C and salinity between 34.4–34.9 ppt. AW is located basically along the Norwegian Current and PW in the central Arctic Ocean and the East Greenland Current. ASW lies between AW and PW and in the gyres of the Greenland and Iceland Seas.

The model distributions of temperature and salinity (Figs. 12.4 and 12.5) agree well with the three ASL water types. Note that the model temperature and salinity vary seasonally. For example, the summer temperature of the East Greenland Sea (Fig. 12.4) is 1°–2°C higher than the PW described above. The model Atlantic layer, deep waters, and Arctic shelf waters are located under the mixed layer and will be discussed with other sensitivity studies in the future.

13.2 Central Arctic

The Transpolar Drift and the Beaufort Gyre are the dominant ocean currents in this region. The vertical and lateral heat fluxes are the important factors as to whether or not sea ice exists. Because of the permanent existence of sea ice, the mixed-layer temperature of the currents remains at the freezing point most of the year. Consequently, lateral oceanic heat fluxes are small. However, coastal seas along Russia and Alaska are clear of sea ice in summer and have open water.

The distribution of the model ice thickness shows packed thick sea ice north of Canada and Greenland (between 3.5 – 8.5 m for March 1986). The sea ice becomes thinner toward the North Pole (between 3.0 – 4.5 m). The thickness continues to decrease toward the Laptev Sea and the Kara Sea north of Russia. The distribution remains approximately the same throughout the year, but the absolute value of the thickness varies seasonally (e.g., 1–2 m between summer and winter near the North Pole).

The ice drift is essentially dominated by the geostrophic winds that blow from Russia to Canada most of the year. Such ice advection affects the ice distribution: thick near Greenland and thin near the Laptev Sea. The accumulated thick ice in the East Siberian Sea is likely to have been caused by the use of the monthly mean winds advecting the sea ice in that direction for several months. The monthly geostrophic winds of summer move from the central Arctic to the Laptev Sea and force ice to drift into that sea. As a result, the Laptev Sea is covered by sea ice during summer (Figs. 12.1, 12.2, and 12.3).

In similar work, Walsh et al. [1985] used the Hibler ice model to extend the model domain to the North Pacific Ocean and the Labrador Sea. The horizontal grid was 222 km and the model sea ice was estimated in Cartesian coordinates. No ocean model was coupled. Geostrophic winds and temperature-derived thermodynamic fluxes from 1951 to 1980 drove the model. The 30-yr mean for February (Case N30) shows an ice thickness distribution similar to the PIPS2.0 result: thin in the Laptev Sea (approximately 1.5 m), thick near the North Pole (approximately 2.5 m), and still thicker toward Greenland and the Canadian Archipelago (approximately 3.5–4.0 m). The August 30-yr mean shows a similar distribution, but thinner: 0–0.5 m for the Laptev Sea, 2.5–3.0 m north of Greenland and the Canadian Archipelago. In spite of different atmospheric forcing fields, and without the ocean model, Walsh et al.'s February and August means are consistent with the PIPS2.0 ice-ocean coupled model results, although the former is 0.5–4.0 m thinner than the latter.

13.3 Barents Sea

The ice thickness reaches a maximum of 2 m in the northwestern Barents Sea in March, and the ice drift is dominated by the cyclonic geostrophic winds. No sea ice grows in the south

and southwestern Barents Sea because the water, which is part of the Norwegian Current, is warm and salty throughout the year. In March, the open-water temperature ranges from 0°–4°C, even though the corresponding air temperature is between −10° and 0°C. In summer, sea ice usually retreats from the Barents Sea to a region near the Franz Josef Islands, the boundary of the sea and the central Arctic. The mixed layer is dominated by Atlantic water and has a salinity between 34 and 35 ppt, except for the northern sea near Spitsbergen, the Franz Josef Islands, and Novaya Zemlya. That region could have a salinity as low as 33 ppt in summer. The sea ice distribution affected by geostrophic winds could vary from year to year.

In the Barents Sea, the ice edge of the PIPS2.0 model agrees in general with the JIC weekly analysis throughout the year. This consistency implies that the ice-ocean coupled model gives the proper currents and heat fluxes, especially near the ice edge. The JIC analysis reveals two inconsistencies. For August and September, the model results show extra sea ice east of Spitsbergen. For October and November, the model results indicate fast ice growth (generally less than 20% in concentration) in the central and northern portions of the sea. These inconsistencies might imply that the monthly atmospheric forcing does not reflect such sea ice change in fast melting and growing seasons. When the 3-hourly atmospheric forcing is used in operation, the model sea ice would follow the temporal variations and the inconsistencies should be improved.

13.4 East Greenland and Norwegian Seas

The East Greenland Current brings cold, fresh Arctic surface water into the seas through the Fram Strait. This current travels farther south, passes the Denmark Strait, and enters the North Atlantic Ocean. The water is less saline in summer due to ice melt in the sea and the Arctic Ocean (approximately 33 ppt), but is saltier in winter due to ice growth (approximately 34 ppt). The Norwegian Current, which is part of the salty, warm Atlantic water, flows from the Faroe-Shetland Channel north to Spitsbergen and remains ice-free during the year.

The strong ocean current and wind off the eastern coast of Greenland move sea ice from the Fram Strait through the Denmark Strait to the southern tip of Greenland (i.e., from about 82° N–60° N). In winter, sea ice covers the entire region; in summer, it retreats as far south as the Denmark Strait. In March, for example, the water temperature north of the Denmark Strait can reach 4°C. However, due to the strong advection in this region, sea ice can still survive.

In August, the southwesterly offshore winds near the Fram Strait advect sea ice away from the coast. As a result, the distribution of model sea ice indicates open water there (or implies possible fast ice). The JIC weekly analysis shows fast sea ice, but no open water along the coast. The model open water is probably the result of using the offshore winds to drive the coupled model for the entire month of August, while the JIC observations are taken on only a few days. That sea ice distribution from the model might be different if the model was driven by daily (or 3-hourly) winds, instead of the monthly winds. If daily winds were used, sea ice might not be constantly expelled from the coast. Open water in the model does not exist when using the 1992 daily winds for August (P. Posey, pers. comm.).

13.5 Baffin Bay and Labrador Sea

After picking up some Atlantic water southwest of Iceland, the East Greenland Current flows around the southern tip of Greenland and into the Labrador Sea. It is renamed as the West Greenland

Current (WGC) and continues northward along the west coast of Greenland. Most of the WGC water drifts to the west and mixes with the Baffin Land Current and the Labrador Current. The WGC contains warm Atlantic water and remains ice-free along its path throughout the year. In summer, the water temperatures of Baffin Bay and the Labrador Sea seem to decrease with the distance from the North Atlantic Ocean. The water salinity ranges between 33–35 ppt in winter and between 32–34 ppt in summer.

Baffin Bay and the Labrador Sea have very little sea ice in summer and grow new sea ice every winter. Advected sea ice from the Arctic Ocean is limited because of the narrow straits, channels, and sounds. In March, Baffin Bay is covered by sea ice, except for areas near the west Greenland coast where offshore winds constantly advect sea ice away. As with the model predictions for the East Greenland and Norwegian Seas, when the 1992 daily winds are used in studies, sea ice entirely covers Baffin Bay (P. Posey, pers. comm.). The model ice edge agrees with the JIC analysis except in two regions: Baffin Bay west of Greenland and the northern Labrador Sea south of the Ellesmere Island. The absence of sea ice in the model results is likely to have been caused by the constant offshore monthly winds, as discussed above. According to the JIC data in the southern Labrador Sea, sea ice should exist along the Canada coast and extend to Newfoundland. In the coupled model, March cyclonic winds move young sea ice from north to south and then from the southern Labrador Sea into the warm Atlantic water.

Comparing the March ice thickness with the March ice concentration reveals that the latter ice edge extends farther toward the North Atlantic Ocean than the former. The difference in the two ice-edge locations implies thin sea ice in the southern Labrador Sea. Thin sea ice might be caused by returned warm Atlantic water, which plays an important role in melting sea ice.

13.6 Hudson Bay

In summer, the model water temperature in Hudson Bay varies from 0°–10°C and its salinity ranges from 28–32 ppt. Seasonal river runoff, which contributes fresh water and causes low salinity in the east and south of the bay, was not included in this modeling. River runoff could affect the horizontal stratification of water in the bay and produce an estuarine-type circulation [Pickard and Emery 1990]. In winter, water salinity increases to 30–33 ppt, mainly due to ice growth and brine rejection into the bay.

Hudson Bay is totally covered by sea ice during winter and is completely free of ice in August and September. The bay is partially occupied by sea ice in spring and fall. Differences in the estimates of open water between the ice thickness and ice concentration distributions represent thin sea ice coverage, especially in November and December when it grows rapidly. Hudson Bay receives little influence from warm North Atlantic water, except for the northern part of the bay, where some inflow from the Labrador Sea can occur [Wang et al. 1994a; 1994b]. Most of the ice growth and melt in Hudson Bay are dominated by atmospheric forcing.

13.7 Bering Sea

The Bering Sea inflow comes from the Aleutian Islands close to the Alaska Peninsula. The water turns westward and flows out of the sea through the western Aleutians. This outflow joins the Oyashio Current east of the Kamchatka Peninsula. The mixed-layer temperature, influenced by North Pacific water, is sometimes higher than 6°C in the summer. The water exchange with the Arctic through the Bering Strait does not seem to have significant impact for the sea when compared with that of the North Pacific Ocean, but it could possibly initiate and then accelerate sea ice

growth near the Strait. Little sea ice is advected from the Arctic through the Bering Strait. Similar to the situation with temperature, the mixed-layer salinity depends mostly on North Pacific inflow and brine rejection due to sea ice growth.

In the Bering Sea, sea ice starts to form in late October or early November and starts to melt in April. The sea remains open throughout the summer. The model ice-edge locations agree well with the JIC weekly analysis, except for the southeast Bering Sea in winter. In March, for example, the model results indicate the existence of sea ice in the northern Bering Sea and along the western Siberian coast. Sea ice that drifts westward is basically dominated by easterly geostrophic winds. In the southeast Bering Sea, easterly offshore winds blow from Alaska to the sea and advect sea ice away from the coast. In the model, consequently, the southeast Bering Sea cannot retain sea ice. However, the JIC weekly analysis of ice concentration shows some sea ice in this region, which disagrees with the model results. When variable 1992 daily winds, instead of the monthly winds, are used to drive this model, most of the southeastern sea is covered by sea ice in winter [P. Posey, pers. comm.]. Another reason the model incorrectly captures this area is that fresh river runoff makes sea ice grow easier because the lack of salinity causes the freezing temperature to be higher than in regular seawater. River runoff was not included in this part of the modeling, although there is actually considerable outflow. This situation will be addressed in future work.

13.8 Sea of Okhotsk

Some of the Oyashio Current has been observed to make the turn around the southern tip of the Kamchatka Peninsula and to flow into the Sea of Okhotsk. It continues northward along the west coast of that peninsula and circulates the sea cyclonically. Finally, the water flows out through the southern Kuril Islands. Another small inflow (1–3 Sv) comes in from the Soya Channel between the Hokkaido and Sakhalin Islands.
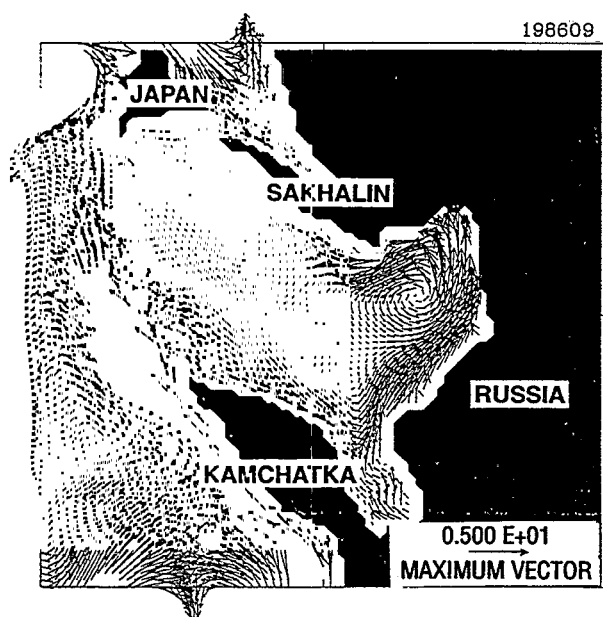

Fig. 13.8.1 — Ocean current in the Sea of Okhotsk with low eddy coefficients, 15-m depth

The circulation in the Sea of Okhotsk that the model produces, under normal values for the model parameters, flows anticyclonically and is not consistent with that discussed above. However, when eddy coefficients of viscosity and diffusivity are reduced to 10^8 and 10^6 cm^2/s, respectively, the cyclonic circulation is reproduced by the model and agrees with the observed circulation (Fig. 13.8.1). Due to plotting problems, Fig. 13.8.1 neither shows values for the Kuroshio and Oyashio Currents higher than 5 cm/s, nor represents the Kuril Islands.

In the Sea of Okhotsk, sea ice starts to grow from late November or early December, and it begins to melt in April. During the summer, the sea remains ice-free. In winter, sea ice stays in the northern and western sections of the sea (i.e., along the continental coast and along Sakhalin Island, respectively). The eastern Sea of Okhotsk along the Kamchatka Peninsula and along the Kuril Islands remains

ice-free throughout the year. Differences between the ice thickness and ice concentration distributions in the northern part of the sea represent thin sea ice. The model concentration for March agrees with the JIC weekly analysis.

14.0 REMARKS AND CONCLUSIONS

An algorithm was developed for transforming the coordinates of the ice and ocean models that make up the PIPS system from Cartesian coordinates to spherical coordinates. This transformation was made to avoid the numerical singularity at the North Pole and to increase the numerical stability in high latitudes. The spherical coordinates have a new equator that coincides with the 10° E–170° W great circle and a new north pole that is located at the intersection of the 100° E meridian and the true equator. Tests demonstrated that the transformed PIPS model gives the same results as the Cartesian coordinates PIPS model.

The domain for the spherical coordinates PIPS model was extended southward to the 20° N–30° N region, depending on which part of the grid is considered. PIPS2.0, as this transformed and regridded model is called, covers all sea ice in the Northern Hemisphere. The horizontal grid resolution is 0.28575° × 0.28575°. The Cox ocean model has also been regridded to the new domain.

The ice and ocean models have been coupled for their integration by exchanging daily information. Mixed-layer temperatures, variable freezing temperatures, oceanic heat fluxes, and ocean currents go from the ocean model to the ice model. A variable drag coefficient, salinity transfers, and daily ice growth rates are returned to the ocean model from the ice model. In coupling, the sea ice is treated as a boundary layer that blocks direct heat and momentum exchanges between the atmosphere and ocean.

The runs that were made with the ice-ocean coupled model had much input information in common. The ETOPO5 bathymetry data were interpolated into the PIPS2.0 model domain using cubic splines. After interpolation and integration, the bottom topography was divided into 15 levels, as was appropriate for the Cox ocean model [1984]. Level 1 (the top) thickness was fixed at 30 m.

The 1986 NOGAPS atmospheric forcing fields were used to develop and test the PIPS2.0 ice-ocean coupled model. These fields have insufficient resolution, both temporally and spatially, to support accurate studies in small areas. When used operationally, they will be replaced by high-resolution, 3-hourly winds, and their form will be transferred to the ice-ocean model as stresses. Both these improvements will address limitations on the applicability of PIPS2.0 results.

The Levitus seasonal and annual climatological data of water temperature and salinity [1982] were interpolated into the PIPS2.0 model domain. Resolution of the Levitus data makes it difficult to consider coasts, bays, small seas, and narrow straits. New climatological data are being prepared that can address this limitation as well and can be used by the PIPS2.0 model directly.

In addition to the limitations of applicability of PIPS2.0 caused by the input data characteristics, implementation algorithm characteristics also might impact on how successfully this model can be applied to given situations. The top layer of the ice-ocean coupled model that represents the ocean's mixed layer has been kept at a constant 30-m thickness for this version. In reality, the mixed layer is a function of season (thin in winter and thick in summer) and is influenced by the influx of fresh water from river runoff. In the Arctic Ocean, the mixed layer is estimated to vary from 30–50 m in thickness [Carmack 1990]. The approximation that was made could become important in the marginal ice zone because a thin mixed layer can grow ice easier than a thick one. In the North

Pacific and Atlantic Oceans, the open-water mixed layer varies seasonally from shallow to 200 m deep. For both oceans, the top 30-m level does not represent the mixed layer, but it is used in modeling to interact with the atmospheric forcing.

In the PIPS2.0 model, a variable ice-water drag coefficient $C_{d,ice-water}$ was used to force certain kinds of sea ice drift to follow the underlying ocean currents closely. Of particular concern are thin sea ice and icebergs. In reality, these ice forms drift along with the currents like buoys, so it is imperative that the model represent that situation.

Hibler and Bryan [1987] used the ocean current of Level 2 to approximate the geostrophic currents and to compute the sea surface height. At present in the PIPS2.0 model, the ocean currents of Levels 1 and 2 are similar, so the sea surface heights based on both look identical, which does not affect sea ice computations. However, if the daily or 3–hourly winds are used to drive the coupled model, the wind-driven current of Level 1 could significantly differ from that in Level 2. Further work is needed on this point to minimize the effect on sea ice calculations.

15.0 ACKNOWLEDGMENTS

16.0 REFERENCES

Aagaard, K. and E. C. Carmack, "The Role of Sea Ice and Other Fresh Water in the Arctic Circulation," *J. Geophys. Res.* **94**, 14485–14498 (1989).

Allard R., R. Preller, S. Piacsek, and A. Cheng, *The Fourth Conference on Polar Meteorology and Oceanography*, 15–20 Jan 1995, Dallas, TX, pp. 193–199.

Bryan, K., "Accelerating the Convergence to Equilibrium of Ocean-Climate Models," *J. Phys. Oceanogr.* **14**, 666–673 (1984).

Carmack, E., "Large-Scale Physical Oceanography of Polar Oceans," in *Polar Oceanography: Part A*, W. Smith, Jr., ed., Academic Press, 1990.

Cheng, A. and R. Preller, "An Ice-Ocean Coupled Model for the Northern Hemisphere," *Geophys. Res. Let.* **19**, 901–904 (1992).

Cheng, A. and R. Preller, "An Ice-Ocean Coupled Model for the Northern Hemisphere," proceedings of 1993 International Symposium on Sea Ice, pp. 78–87, 1994.

Cox, M., "A Primitive Equation, 3-Dimensional Model of the Ocean," GFDL Ocean Group Tech. Rep. 1, 141 pp., Geophys. Fluid Dyn. Lab., Princeton, NJ, 1984.

Ebbesmeyer, C. C. and W. J. Ingramham, Jr., "Pacific Toy Spill Fuels Ocean Current Pathways Research," *EOS* **75**, 425–428 (1994).

Flato, G. M. and W. D. Hibler III, "Modeling Pack Ice as a Cavitating Fluid," *J. Phys. Oceanogr.* **22**, 626–651 (1993).

Hibler, W. D. III, "A Dynamic Thermodynamic Sea Ice Model," *J. Phys. Oceanogr.* **9**, 815–864 (1979).

Hibler, W. D. III, "Modeling a Variable Thickness Sea Ice Cover," *Mon. Weather Rev.* **108**, 1943–1973 (1980).

Hibler, W. D. III and K. Bryan, "A Diagnostic Ice-Ocean Model," *J. Phys. Oceanogr.* **17**, 987–1015, (1987).

Holland, D. M., "Some Numerical Issues Relating to the Simulation of Sea Ice," proceedings of 1993 International Symposium on Sea Ice, pp. 88–99, 1994.

Levitus, S., "Climatological Atlas of the World Ocean," National Oceanic and Atmospheric Administration Prof. Paper 13, p. 173, 1982.

McPhee, M. G., "Small-Scale Processes," in *Polar Oceanography, Part A: Physical Science*, W. Smith, ed., Academic Press, Inc., pp. 287–333, 1990.

Mellor, G. and T. Ezer, "A Gulf Stream Model and an Altimetry Assimilation Scheme," *J. Geophys. Res.* **96**, 8779–8796 (1991).

Mellor, G. L., "The Princeton Ocean Model: Users Guide for a Three–Dimensional Primitive Equation, Numerical Ocean Model," Program in Atmospheric and Oceanic Science Rep., Princeton University, p. 35, 1992.

Muench, R. D., "Mesoscale Phenomena in the Polar Oceans, Polar Ocean: Part A, Physical Science," W. O. Smith, Jr., ed., pp. 223–286, Academic Press, Inc., 1989.

Owens, W. B. and P. Lemke, "Sensitivity Studies with a Sea Ice-Mixed Layer-Pycnocline Model in the Weddell Sea," *J. Geophys. Res.* **95**, 9527–9538 (1990).

Pickard, G. L. and W. J. Emery, "Descriptive Physical Oceanography: An Introduction," Fifth (SI) Enlarged Edition, Pergamon Press, 1990.

Preller, R. H. and P. G. Posey, "The Polar Ice Prediction System – A Sea Ice Forecasting System," NORDA Report 212, Naval Research Laboratory, Stennis Space Center, MS, 1989.

Preller, R. H., P. G. Posey, and A. Cheng, "A Preliminary Study of the Dispersion of Radioactive Contaminants in the Kara and Barents Seas Using a Coupled Ice-Ocean Model," Nansen Centennial Symposium, Bergen, Norway, 1993.

Preller, R. and A. Cheng, "Modeling the Dispersion of Radioactive Contaminants in the Arctic," submitted to *Bulletin of Marine Pollution* (1995).

Sarmiento, J. L. and K. Bryan, "An Ocean Transport Model for the North Atlantic," *J. Geophys. Res.* **87**, 395–408 (1982).

Semtner, A. J., Jr., "A Numerical Study of Sea Ice and Ocean Circulation in the Arctic," *J. Phys. Oceanogr.* **17**, 1077–1099 (1987).

Shiklomanov, I. and B. Skakalsky, "Studying Water, Sediment and Contaminant Runoff of Siberian Rivers: Modern Stats and Prospects," in Workshop on Arctic Contamination, in *Proceedings of the Interagency Arctic Research Policy Committee*, Anchorage, AK, May 2–7, 1993.

Walsh, J. E., W. D. Hibler III, and B. Ross, "Numerical Simulation of Northern Hemisphere Sea Ice Variability, 1951–1980," *J. Geophys. Res.* **90**, 4847–4865 (1985).

Wang, J., L. A. Mysak, and R. G. Ingram, "A Three-Dimensional Numerical Simulation of Hudson Bay Summer Ocean Circulation: Topographic Gyres, Separations, and Coastal Jets," *J. Phys. Oceanogr.* **24**, 2496–2514 (1994a).

Wang, J., L. A. Mysak, and R. G. Ingram, "A Numerical Simulation of Sea Ice Cover in Hudson Bay," *J. Phys. Oceanogr.* **24**, 2515–2533 (1994b).